Doctoral Dissertation
博士論文

Search for direct Chargino production based on a disappearing-track signature at $\sqrt{s} = 13$ TeV with the ATLAS detector

(ATLAS検出器での13TeV衝突エネルギー実験データを用いた消失飛跡を特徴としたチャージーノ探索)

A Dissertation Submitted for the Degree of Doctor of Philosophy
April 2019
平成31年4月博士（理学）申請

Department of Physics, Graduate School of Science,
The University of Tokyo
東京大学大学院理学系研究科
物理学専攻

Masahiko Saito
齊藤 真彦

Abstract

A supersymmetric theory is one of the most well-motivated theories of Beyond the Standard Model. The past observations favour the supersymmetric models where the lightest charged-supersymmetric particle is nearly mass-degenerate with the lightest neutral-one. Such models predict a meta-stable charged supersymmetric particle with a lifetime of O(0.01–0.1) ns, resulting in a characteristic track signature, called disappearing track. This thesis presents a search for a direct chargino production based on the disappearing track signature in the ATLAS detector in the proton-proton collisions produced by the Large Hadron Collider at the centre of mass energy of 13 TeV. The introduction of short tracks which consist of only four Pixel-sensor hits gives a significant improvement for the signal acceptance by a factor of seven.

The results with data recorded in 2015–2017 show no significant excess from the Standard Model prediction, resulting in the strong constraints for the pure wino/higgsino LSP scenarios; the chargino mass up to 490 GeV is excluded in the pure wino LSP scenario, and the chargino mass up to 170 GeV is excluded in the pure higgsino LSP scenario. The future prospects of disappearing track analysis are also discussed. Although the current LHC does not have a sensitivity to explore the entire chargino-mass parameter space which is viable from the cosmology, the next-generation collider, Future Circular Collider, has the sufficient potential to discover them.

Contents

Chapter 1

Introduction

The discovery of the Higgs boson in 2012 was a milestone on the elementary particle physics, resulting in the reconfirmation of the validity of the Standard Model. The Standard Model is, however, not a perfect nor an ultimate theory because it contains an artificial tuning like the anthropic principle and cannot explain 95% of the energy in our universe. Importance of the searches for new physics beyond the Standard Model is increasing since there is still no clear hint indicating new theories close to the ultimate theory.

One of the most well-motivated theories is a supersymmetric theory, which solves many problems in the Standard Model. Although the supersymmetric theory has a huge number of model parameters, the properties of the supersymmetric theory are expected according to the precise agreements between nature and the Standard Model and a few unexpected deviations, including the existence of dark matter. One of the well-motivated scenarios in the supersymmetric theories is the case where superpartners of the W boson or the Higgs boson is the lightest supersymmetric particle. Such scenarios can be satisfied with constraints from the Higgs boson mass, dark-matter relic density and the flavour physics.

Despite the motivation, it is known to be hard to search for such a scenario in hadron collider experiments within the traditional searches based on only energetic jets, leptons and the missing transverse momentum due to the lack of energetic particles from a cascade decay from the supersymmetric particles. On the other hand, instead of the energetic signatures, such a model predicts a charged meta-stable supersymmetric particle with a lifetime of O(0.01–0.1) ns. Since such a lifetime corresponds to the decay radius of O(1–10) cm, which is smaller than the size of a track detector (tracker) in the ATLAS detector, the charged supersymmetric particles can be observed as suddenly disappearing in the tracker after running some macroscopic distances. Such a signature is called a disappearing track. Since the Standard Model particles do not produce a disappearing track, a requirement for the disappearing track has strong rejection power for the Standard Model particles.

The past experiments using disappearing track signature did not have adequate signal acceptance because it was difficult to reconstruct the short tracks comparable with the

typical decay radius (O(1–10) cm) due to the tracker layout. The ATLAS experiment upgraded the tracker in the long-shutdown in 2013–2014, making it possible to reconstruct shorter tracks with the track length of 12 cm. The shorter tracks and the improvements in various parts in the analysis including the track reconstruction, measurements of the tracking performance and the background estimation technique, significantly improve the sensitivity for the supersymmetric particles.

This chapter briefs the supersymmetric theory and the motivative supersymmetric scenarios at first, then describes the properties of the characteristic signature predicted from the motivative scenarios. After showing a limitation of the disappearing track analysis, a significant advantage of the shorter tracks is discussed. The last section gives an overview of this thesis.

1.1 The problems in the Standard Model

The Standard Model (SM) of elementary particle physics was theoretically finalised by the 1970s for the most part, and verified by many experimental results. The last missing particle in the SM, i.e. Higgs boson, was discovered by both the ATLAS and the CMS experiments in 2012 [1,2], resulting in the experimental confirmation of the SM. The SM describes the properties of elementary particles with surprising precision. It is, however, not a perfect model: the SM has some problems.

The first problem is related to the naturalness of SM parameters. This problem relates to the Higgs boson. Higgs boson mass is contributed by a radiative correction from a fermion loop, e.g. top-quark

$$\Delta m_h^2 \propto \frac{3\lambda_t^2}{4\pi^2}\Lambda^2, \tag{1.1}$$

where λ_t is a top Yukawa coupling constant and Λ is the cut-off scale of the SM. The cut-off scale is considered to be near the Planck scale $\approx$ O(10^{19}) GeV if the SM is valid to this energy scale, while the observed Higgs mass is around 125 GeV. Therefore, to accomplish the observed Higgs mass, the squared of the bare mass must be tuned at 10^{-34} level. Since this is not natural, this problem is called a naturalness problem.

The second one is related to a grand unification theory (GUT). When considering the GUT, the strengths of the three fundamental forces (electromagnetic, weak and strong) should be unified at one energy scale, called the GUT scale. However, it was revealed that the three gauge coupling constants are not unified at a high energy scale if considering all contributions only from the SM particles. So GUT is not simply accomplished in the SM.

The third one is the existence of dark matter, which was proposed at first to explain the inconsistency of the galactic rotation curves. By the great success of the Λ-Cold Dark Matter model with the precise measurements of cosmic microwave background by the WMAP/Planck, detailed properties of dark matter in our universe became clear: dark-matter density is five times larger than the baryon density, dark matter does not interact

electromagnetically and strongly, and its velocity should be small. Such a particle does not exist in the SM.

The existence of Beyond the Standard Model (BSM) is necessary to solve the three problems mentioned above, and many kinds of BSMs are proposed.

1.2 Supersymmetry

Supersymmetry (SUSY) models are the promising BSM models which can solve these problems. Supersymmetry is a new symmetry between bosons and fermions. SUSY predicts additional new particles, called the superpartners, which have the same properties as the SM particles except for the spin. Such particles, however, are rejected experimentally, e.g. no scalar particle with the electron mass, corresponding to the electron-counterpart, has been observed The supersymmetry must be broken, and SUSY particles are expected to have heavier masses than the SM particles.

Although new particles predicted in the SUSY are not discovered yet, SUSY is a well-motivated model, because the SUSY solves the problems in the SM.

Naturalness

The new symmetry protects the Higgs mass from a quadratic divergence. A contribution to a radiative correction of the Higgs mass from new scalar particles gives an opposite-signed contribution to the SM fermions, resulting in a cancellation of the quadratic divergence and relaxation to a logarithmic divergence. Although the Higgs mass is a free parameter in the SM, it can be predicted in the SUSY frameworks as follows

$$\begin{aligned} m_h^2 &\lesssim m_Z^2 \cos^2 2\beta + \frac{3g^2 m_t^4}{8\pi^2 m_W^2}\left(\log\frac{m_{\tilde{t}}^2}{m_t^2} + \frac{X_t^2}{m_{\tilde{t}}^2}\left(1 - \frac{1}{12}\frac{X_t^2}{m_{\tilde{t}}^2}\right)\right) \\ X_t &= A_t - \mu\cot\beta \\ m_{\tilde{t}}^2 &\sim m_{\tilde{t_1}} m_{\tilde{t_2}}, \end{aligned} \tag{1.2}$$

where $\tan\beta$ is the ratio of vacuum expectation value, $m_{\tilde{t}}$, m_t, m_h, m_Z and m_W are the masses of superpartner of top-quark, top-quark, Higgs boson, Z boson and W boson, respectively, A_t is the trilinear coupling of Higgs and a superpartner of top-quark, μ is a mixing parameter of doublet Higgs and g is SU(2) gauge coupling. The second term is a contribution from a radiative correction, and it is proportional to the logarithm of the mass scale of a new particle. Even though the Higgs mass depends on some SUSY parameters, it should be less than around 130 GeV. The observed Higgs mass (125 GeV) favours the existence of SUSY.

Grand Unification

An existence of SUSY particles changes a gauge-coupling renormalisation-group-equations (RGE) as follows

$$\alpha_i^{-1}(Q) - \alpha_i^{-1}(M_{\rm GUT}) = \frac{b_i}{2\pi} \ln\left(\frac{Q}{M_{\rm GUT}}\right), \ (i = 1, 2, 3) \tag{1.3}$$

$$(b_1,\ b_2,\ b_3)_{\rm SM} = \left(-\frac{41}{10},\ \frac{19}{6},\ 7\right)$$

$$\Rightarrow (b_1,\ b_2,\ b_3)_{\rm MSSM} = \left(-\frac{35}{5},\ -1,\ 3\right), \tag{1.4}$$

where α_i^{-1} is an inverse gauge coupling, Q is an energy scale and $M_{\rm GUT}$ is an energy scale of the grand unification. The three coupling constants are unified at one energy scale $\approx$ O(10^{16}) GeV when assuming TeV-scale SUSY particles as shown in Fig. 1.1.

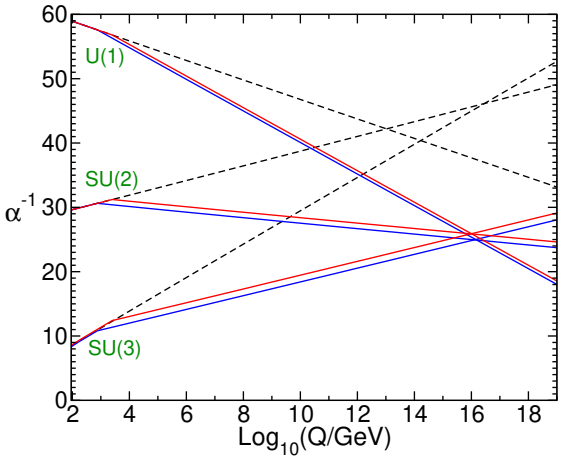

Figure 1.1: Inverse gauge couplings (α^{-1}) as a function of energy scale (Q) (Ref. [3]). Black dotted lines show ones with considering only the SM particles. Red lines and blue lines show ones with introducing supersymmetric particles mass of 750 GeV and 2.5 TeV, respectively. Three coupling constants are unified at one energy scale thanks to introduced supersymmetric particles mass of 1–10 TeV.

Dark matter

The lightest SUSY particle (LSP) is a candidate of a dark-matter. The details are discussed in Sec. 1.4.

1.3 Minimal Supersymmetric Standard Model

SUSY can solve many problems in the SM as shown in Sec. 1.2. This section describes a minimum supersymmetric extension of the SM, called the Minimal Supersymmetric

Standard Model (MSSM) as a practical framework to discuss the phenomenology of SUSY models.

The MSSM contains only one supersymmetric partner for each SM particle as shown in Table 1.1. Superpartners have different spins from the SM particles for just by half. The superpartners of quarks and leptons are called squarks and sleptons, and the superpartners of bosons (Higgs boson, gluon, W boson, B boson) are called higgsino, gluino, wino and bino, respectively. Especially, superpartners of the gauge bosons are called gauginos. Although a graviton is an undiscovered particle, its superpartner gravitino often takes an important role in the phenomenology and cosmology.

Super multiplet		spin 0	spin 1/2	spin 1	$(SU(3)_C, SU(2)_W, U(1)_Y)$
squarks/quarks	Q	$(\widetilde{u}_L, \widetilde{d}_L)$	(u_L, d_L)		(**3**, **2**, $\frac{1}{6}$)
	$\bar{u}$	$\widetilde{u}_R$	u_R		($\bar{\mathbf{3}}$, **1**, -$\frac{2}{3}$)
	$\bar{d}$	$\widetilde{d}_R$	d_R		($\bar{\mathbf{3}}$, **1**, $\frac{1}{3}$)
sleptons/leptons	L	$(\widetilde{e}_L, \widetilde{\nu}_L)$	(e_L, ν_L)		(**1**, **2**, -$\frac{1}{2}$)
	$\bar{e}$	$\widetilde{e}_R$	e_R		(**1**, **1**, 1)
Higgs/higgsinos	H_u	(H_u^+, H_u^0)	$(\widetilde{H}_u^+, \widetilde{H}_u^0)$		(**1**, **2**, $\frac{1}{2}$)
	H_d	(H_d^0, H_d^-)	$(\widetilde{H}_d^0, \widetilde{H}_d^-)$		(**1**, **2**, -$\frac{1}{2}$)
gluinos/gluons	g		$\widetilde{g}$	g	(**8**, **1**, 0)
winos/W-bosons	W		$\widetilde{W}^0, \widetilde{W}^\pm$	$W^0, W^\pm$	(**1**, **3**, 0)
bino/B-boson	B		$\widetilde{B^0}$	B^0	(**1**, **1**, 0)

Table 1.1: Supermultiplets in the MSSM. A right column shows the representation of the gauge groups of $SU(3)_C \times SU(2)_W \times U(1)_Y$. Only the first generation sparticles are shown.

The MSSM introduces two Higgs doublets because only one Higgs doublet cannot give the fermion mass for both up- and down- types. So there are two vacuum expectation values (VEVs) of Higgs doublets ($\langle H_u^0 \rangle, \langle H_d^0 \rangle$). The ratio of two VEVs is a free parameter but takes an important role in the MSSM, so the ratio is traditionally written using a mixing angle β as

$$\tan\beta = \frac{\langle H_u^0 \rangle}{\langle H_d^0 \rangle}. \tag{1.5}$$

Since bino, wino and higgsino have the same quantum numbers, they mix and form new mass-eigenstates. Neutral states are called neutralinos, and charged states are called charginos. The mass matrix of neutralinos ($\widetilde{B}, \widetilde{W}^0, \widetilde{H}_d^0, \widetilde{H}_u^0$) is given as

$$M_{\tilde{N}} = \begin{pmatrix} M_1 & 0 & -m_Z \sin\theta_W \cos\beta & m_Z \sin\theta_W \sin\beta \\ 0 & M_2 & m_Z \cos\theta_W \cos\beta & -m_Z \cos\theta_W \sin\beta \\ -m_Z \sin\theta_W \cos\beta & m_Z \cos\theta_W \cos\beta & 0 & -\mu \\ m_Z \sin\theta_W \sin\beta & -m_Z \cos\theta_W \sin\beta & -\mu & 0 \end{pmatrix}, \tag{1.6}$$

where M_1 and M_2 are the mass terms of bino and wino, respectively, μ is a mixing parameter of doublet Higgs, and θ_W is a Weinberg angle. As shown in the mass matrix (Eq. 1.6), a component of the mixture depends on the M_1, M_2, μ, Weinberg

angle (θ_W) and $\tan\beta$. The mixing changes the properties of neutralinos and especially is related to dark-matter properties, which is discussed in Sec. 1.4. As a context of the phenomenology, the mass eigenstates are often used. They are written as $\widetilde{\chi}^0_1$, $\widetilde{\chi}^0_2$, $\widetilde{\chi}^0_3$, $\widetilde{\chi}^0_4$ in the order of their masses. A mass matrix of chargino ($\widetilde{W}^{\pm}, \widetilde{H}^{\pm}_{u/d}$) is given as

$$M_{\widetilde{C}} = \begin{pmatrix} M_2 & \sqrt{2}m_W \cos\beta \\ \sqrt{2}m_W \sin\beta & \mu \end{pmatrix}. \tag{1.7}$$

The mass-eigenstates are written as $\widetilde{\chi}^{\pm}_1$, $\widetilde{\chi}^{\pm}_2$ in the order of their masses.

In the MSSM, an R-parity is introduced

$$R = (-1)^{3(B-L)+2S}, \tag{1.8}$$

where B, L and S are the baryon number, the lepton number and the spin. All the SM particles have R = +1, while all the supersymmetric partners have R = -1. The Lagrangian of the MSSM consists of using R-parity invariant terms because an R-parity-violated term leads to forbidden processes by some experimental facts, e.g. the baryon number violation which conflicts with the lower limits of the proton lifetime ($> 1.6 \times 10^{34}$ years [4]). Another advantage of the R-parity conservation is that the LSP becomes stable, resulting in a good candidate of dark matter.

1.4 Constraints from past experimental results

The MSSM framework contains large numbers of free parameters. However, it can be constrained with various experimental results.

Higgs mass

The Higgs mass can be predicted in the SUSY framework, unlike the SM, and the measured value, 125 GeV, gives a constraint on SUSY parameters. From Eq. 1.2, there are two possible solutions to explain the Higgs mass. The first solution is that stop mass ($m_{\widetilde{t}}$) is set to heavy enough ($>$ 10 TeV). The second solution is that the stop mixing parameter (X_t) is set to around $\sqrt{6}m_{\tilde{t}}$ with O(1) TeV stop mass. Figure 1.2 shows the relation between the stop mass and the Higgs mass. Although the naturalness favours that a stop is not far from the electroweak scale, heavy sparticles lead to other advantages as discussed later.

Dark-matter relic density

A dark-matter relic density can also constrain on SUSY parameters. There are some candidates of the LSP (and dark-matter as well) in the MSSM framework with R-parity conservation. From an observation of how dark matter interacts with normal matter, the candidates are limited to neutral particles for electromagnetic charge and strong charge, i.e. bino ($\widetilde{B}$), wino ($\widetilde{W}$), higgsino ($\widetilde{H}$) and gravitino ($\widetilde{G}$). Since gravitino becomes a hot dark-matter and it smears out the large structure of the universe, this thesis focuses on neutralinos (bino, wino and higgsino).

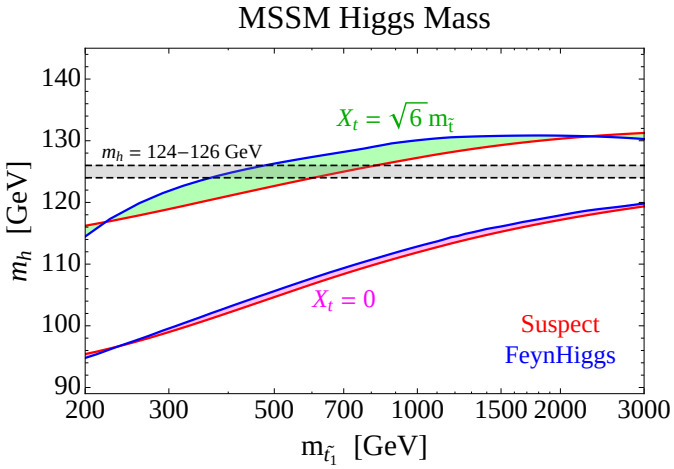

Figure 1.2: The Higgs mass as a function of stop mass [5]. Red lines show the two-loop calculation using Suspect, and blue lines show the two-loop calculation using FeynHiggs. Two upper lines show the case of $X_t = \sqrt{6} m_{\tilde{t}}$ (maximal mixing), and two bottom lines show the case of $X_t = 0$. The $\tan\beta$ is set to 20 for all cases.

The relic density of the lightest neutralino can be calculated with the annihilation cross-section, which is measured by Planck collaboration [6] to be $\Omega_{\rm DM}h^2 = 0.120 \pm 0.001$. Assuming a thermal production scenario where the dark-matter density was fixed at decoupled temperature, the relic abundance of LSP should be smaller than the observed dark-matter density. When the lightest neutralino is a pure bino, the upper bound of the lightest neutralino mass is highly constrained, and it is almost excluded by LHC experiments. The upper bounds can be relaxed by assuming an adequate co-annihilation process, which is realised such as setting a small mass difference between the bino and the next-lightest SUSY particles. Such a compressed region is one of the important phase space in the MSSM [7]. Unlike the bino LSP case, the upper bound of the pure wino and the pure higgsino is more moderate than the pure bino case due to their large cross-section: the upper bounds are 3 TeV for wino and 1 TeV for higgsino, respectively [7]. Therefore, the pure wino and the pure higgsino with their masses of O(0.1–1) TeV can naturally be a dark-matter candidate without a tuning of the next-LSP masses.

When the bino and wino masses decouple with the higgsino masses, mass-eigenstates ($\tilde{\chi}$) are nearly equivalent to pure flavour states ($\widetilde{B}/\widetilde{W}/\widetilde{H}$).

Flavour changing neutral current and CP violation

In the MSSM framework, non-diagonal terms in mass matrices for squarks and sleptons are non-zero in general. Such a term leads flavour mixing or CP violating processes, e.g. the large $K^0 \leftrightarrow \bar{K}^0$ mixing ($\Delta m_K = m_{K_L} - m_{K_s}$) and lepton flavour violation, e.g. $\mu \to e\gamma$. However, they should be highly suppressed by some experimental results [8]. Such processes can be suppressed if squarks and sleptons are nearly mass-degenerate or their masses are heavy ($\gg$O(1) TeV).

1.5 SUSY breaking models

Since the MSSM contains a huge number of parameters (124), the parameters are reduced by assuming the SUSY breaking mechanism. Considering the experimental constraints as discussed in the previous section, this thesis focuses on SUSY breaking models that predict

Condition 1.
The LSP is a neutralino which consists of a pure wino state or a pure higgsino state, and their masses do not lead to the overabundance of the dark-matter relic density.

Condition 2.
Squark masses and slepton masses are heavy enough to explain the Higgs mass and the current experimental constraints from the flavour physics.

There are three models in which these conditions are satisfied.

1.5.1 Anomaly mediated SUSY breaking model

Anomaly Mediated SUSY Breaking (AMSB) models are a promising scenario to predict the wino LSP. These models assign a conformal anomaly as a SUSY mediator connecting the hidden sector to the SM-sector [9], and this is a general breaking mechanism in all other SUSY models.

The mediator creates gaugino masses as following

$$M_i \quad = \quad \frac{b_i}{16\pi^2} g_i^2 m_{3/2} \quad (i = 1, 2, 3), \tag{1.9}$$

where g_i are gauge coupling constants of the SM gauge groups, $m_{3/2}$ is the gravitino mass, and b_i are coefficients of RGE (Eq. 1.4) in the MSSM case. From the relation of the magnitude of $b_i g_i^2$ values, a wino becomes the LSP. The mediator also contributes to masses of scalar SUSY particles, and resultant squared of scalar mass becomes negative. Therefore an artificial scalar-mass term (m_0) is added as an input model parameters to avoid a tachyon. These models are described using only four model parameters: m_0, $m_{3/2}$, $\tan\beta$ and sign(μ), which is a sign of higgsino mixing parameter (μ).

1.5.2 Pure gravity mediation model

Pure Gravity Mediation (PGM) models [10–12] are an extension of the AMSB models. In these models, sfermion and higgsino masses are produced from the mediation of gravity at tree level. Therefore, their masses are comparable to the gravitino mass. On the other hand, due to the lack of the tree-level contribution for gaugino masses, they are mainly produced from one-loop level gravity mediation. Therefore, the gaugino masses naturally become lighter than squark/slepton masses by a factor of 10^{-1}–10^{-2}, resulting in the satisfaction of the Condition 2. Considering the next-to-leading corrections [13],

the gaugino masses are affected by a sizeable contribution from the higgsino threshold correction due to the large higgsino mass comparable to the gravitino mass as follows,

$$M_1 = \frac{33}{5}\frac{g_1^2}{16\pi^2}(m_{3/2} + \frac{1}{11}L) \tag{1.10}$$

$$M_2 = \frac{g_2^2}{16\pi^2}(m_{3/2} + L) \tag{1.11}$$

$$M_3 = -3\frac{g_3^2}{16\pi^2}m_{3/2} \tag{1.12}$$

$$L = \mu \sin 2\beta \frac{m_A^2}{|\mu|^2 - m_A^2} \ln \frac{|\mu|^2}{m_A^2}, \tag{1.13}$$

where M_1, M_2 and M_3 are mass terms of bino, wino and gluino, respectively, μ and m_A are the higgsino mixing term and the pseudo-scalar Higgs mass, respectively. L represents a contribution from a higgsino threshold correction. The L parameter is expected to be of the same order of $m_{3/2}$ when $\mu \sim m_{3/2}$. Although the large L parameter leads the bino-LSP scenario, a large part of the phase space leads the wino-LSP scenario.

1.5.3 Supergravity mediation model

Supergravity mediation model (SUGRA) assumes that both the sparticle masses and gaugino masses are produced through the mediation of gravity at tree level. This model uses only five model parameters: a universal sparticle mass at the GUT scale (m_0), a universal gaugino mass at the GUT scale ($m_{1/2}$), a universal trilinear coupling (A_0), $\tan\beta$ and a sign of the μ (sign(μ)). When m_0 is set to a large value, Condition 2 is satisfied.

In this case, the gaugino mass relation is different from the above two models, because the mass relation is determined by the RGE of the gaugino mass as follows

$$M_1 : M_2 : M_3 = g_1^2 : g_2^2 : g_3^2 \approx 1 : 2 : 6. \tag{1.14}$$

In the mSUGRA model, the lightest gaugino is a bino, instead of a wino. However, when $m_{1/2}$ is large and μ is small, the neutral higgsinos are the LSP. In this case, Condition 1 is satisfied.

A condition of an electroweak symmetry breaking in the MSSM requires to tune the μ-parameter and the Higgs field soft SUSY-breaking terms (m_{H_U} and m_{H_D}). If μ is set to be a large value compared to the electroweak scale, the high-level tuning is needed. In order to avoid such an unnatural tuning, namely from the view of naturalness, light μ is favoured.

1.6 Phenomenology of the lightest charginos in the pure wino / pure higgsino scenario

As discussed in Sec. 1.5, the wino/higgsino LSP scenario is one of the most important cases in SUSY frameworks. Verification of the above models is, however, not easy for

the following reasons.

- Masses of gluino and squarks are expected to be large in these cases to explain the Higgs mass of 125 GeV. Hadron colliders have strengths in the production of heavy particles having SU(3) charge. However, such heavy strong-particles maybe not be produced even in the highest proton beam at present.
- For the wino/higgsino direct pair production, no energetic secondary particles are emitted from heavier SUSY particles. Both the wino and the higgsino are multiplets of SU(2), and the lightest chargino belongs to the same multiplets as the lightest neutralino due to the little mixing of neutralinos/charginos. Therefore, the mass difference between the lightest neutralino and the lightest chargino becomes quite small not as large to be detected in the detector.

For these reasons, traditional SUSY searches have less sensitivity for the above models. On the other hand, when the lightest chargino is a pure wino or a pure higgsino, the chargino is highly mass-degenerate with the lightest neutralino mass, resulting in an interesting signature. In this section, the phenomenology of the wino/higgsino LSP models is discussed.

1.6.1 Mass difference

The lightest neutralino is nearly mass-degenerate with the next lightest charginos when they are pure states of wino or higgsinos. A tiny mass difference is produced from radiative correction of the SM particles. The mass difference with one-loop calculation is represented as [14–16]

$$m_{\tilde{\chi}_1^\pm} - m_{\tilde{\chi}_1^0} = \frac{g^2 M}{8\pi^2}\left[\sin\theta_W^2 f\left(m_Z^2/M^2\right) + (1-2Y) f\left(m_W^2/M^2\right)\right], \quad (1.15)$$

$$f(z) = \int_0^1 (1+x)\log\left[1 + z(1-x)/x^2\right] dx, \quad (1.16)$$

where M and Y are the mass and the hypercharge of the lightest chargino respectively, g is a weak coupling constant, m_Z is the Z-boson mass, θ_W is the Weinberg angle, and the function $f(z)$ is a loop function. The hypercharge for wino (higgsino) is 0 (1/2). Eq. 1.15 can be simplified to

$$m_{\tilde{\chi}_1^\pm} - m_{\tilde{\chi}_1^0} = \begin{cases} \dfrac{g^2 M}{8\pi^2}\left[f\left(m_W^2/M^2\right) - \cos\theta_W^2 f\left(m_Z^2/M^2\right)\right], & \text{for wino} \\ \dfrac{g^2 M}{8\pi^2}\left[\sin\theta_W^2 f\left(m_Z^2/M^2\right)\right], & \text{for higgsino} \end{cases}. \quad (1.17)$$

The function $f(z)$ becomes 1 when $z \to 0$. The mass difference of wino (higgsino) becomes 166 (354) MeV at the limit of $M \gg m_Z$ as shown in Fig. 1.3. A two-loop calculations for wino case were also done [16, 17] and superimposed in Fig. 1.3 (a).

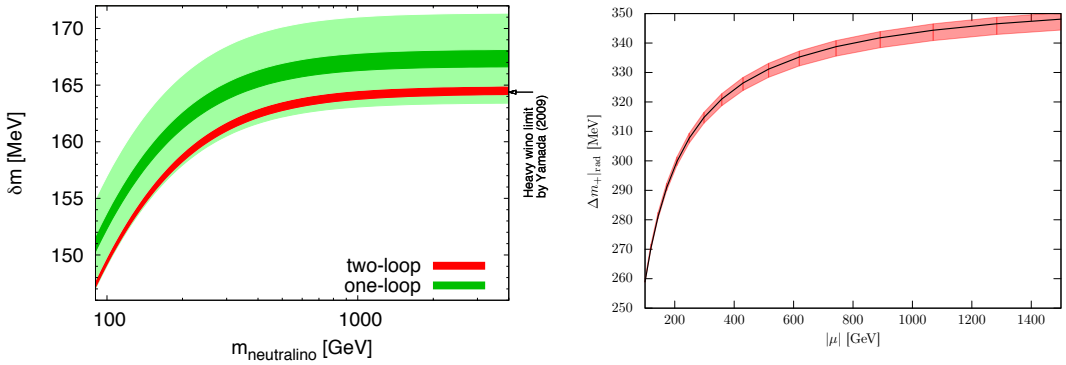

Figure 1.3: Mass splitting between the lightest chargino and the lightest neutralino as a function of the neutralino mass. (a) For the wino case with two-loop calculation [16]. (b) For the higgsino case with one-loop calculation [18].

1.6.2 Decay width and lifetime

Because of the tiny mass splitting, the decay channels of the lightest charginos are highly limited. The possible decaying ways are only into $\pi\tilde{\chi}^0$, $e\nu\tilde{\chi}^0$ and $\mu\nu\tilde{\chi}^0$, and their decay widths depend on the mass splitting given as [14, 16]

$$\Gamma(\widetilde{\chi}_1^{\pm} \to \widetilde{\chi}_{1(,2)}^0 \pi^{\pm}) = \begin{cases} \dfrac{2G_F^2 f_\pi^2}{\pi} \cos\theta_c^2 \Delta m^3 \sqrt{1-\left(\dfrac{m_\pi}{\Delta m}\right)^2}, & \text{for wino} \\ \dfrac{G_F^2 f_\pi^2}{\pi} \cos\theta_c^2 \Delta m^3 \sqrt{1-\left(\dfrac{m_\pi}{\Delta m}\right)^2}, & \text{for higgsino} \end{cases} \tag{1.18}$$

$$\Gamma(\widetilde{\chi}_1^{\pm} \to \widetilde{\chi}_{1(,2)}^0 l^{\pm} \nu_l) = \begin{cases} \dfrac{2G_F^2}{15\pi^3} \Delta m^5 P\left(\dfrac{m_l}{\Delta m}\right), & \text{for wino} \\ \dfrac{G_F^2}{15\pi^3} \Delta m^5 P\left(\dfrac{m_l}{\Delta m}\right), & \text{for higgsino} \end{cases} \tag{1.19}$$

$$P(x) = 1 - \frac{9}{2}x^2 - 4x^4 + \frac{15x^4}{2\sqrt{1-x^2}} \tanh^{-1}\sqrt{1-x^2}, \tag{1.20}$$

where Δm is the mass difference between the lightest chargino and the lightest neutralino, m_π and m_l are the mass of a pion and a lepton respectively, G_F^2 is the Fermi coupling constant, f_π is a pion decay constant, and $\cos\theta_c$ is a Cabibbo angle.

The relation between the mass difference and the chargino lifetime is shown in Fig. 1.4 (a). The lifetime of pure wino (higgsino) is about 0.2 ns (0.023 ns) in the rest frame, corresponding to the mean decay length of O(0.1–10) cm. As shown in Fig. 1.4 (b), a wino or a higgsino decays primarily into a pion which has too low momentum and it is difficult to reconstruct as tracks. Such a particle looks like disappearing in the detector as shown in Fig. 1.5, remaining only a short track in the tracker, which is called disappearing track.

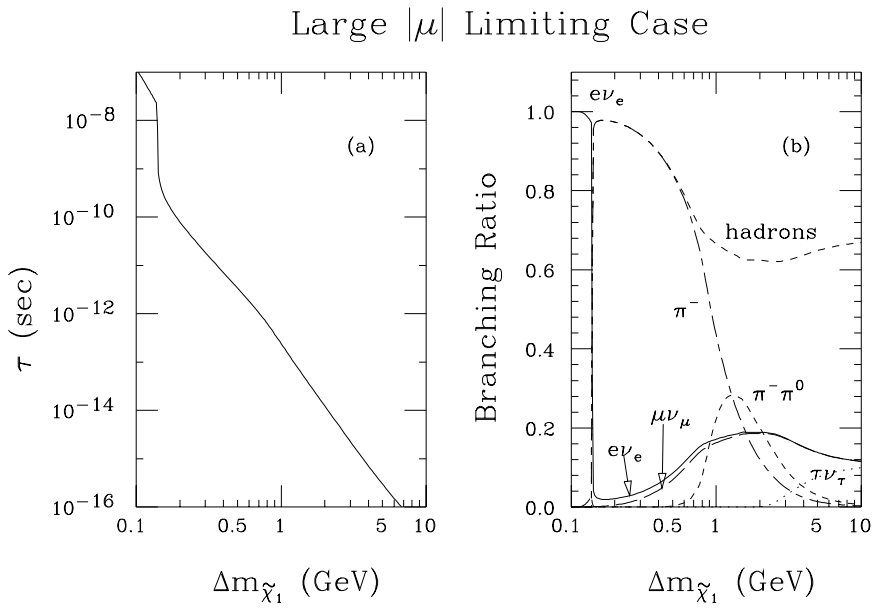

Figure 1.4: (a) A lifetime of the lightest chargino [19]. (b) A decay branching ratio for the lightest chargino [19].

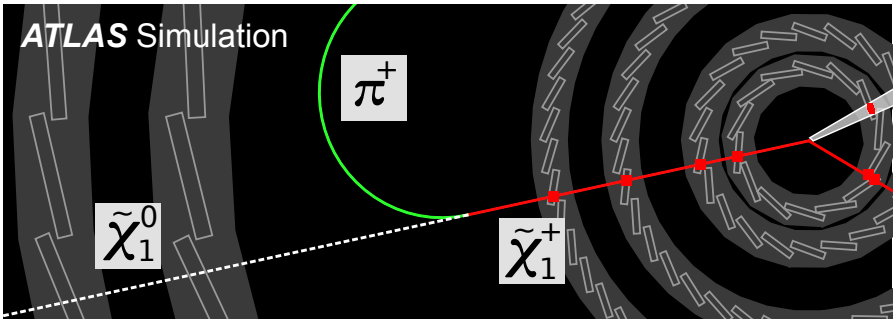

Figure 1.5: Illustration of the disappearing track signature. A chargino is observed as a few sensor-hits in the tracker shown as red squares. A neutralino does not interact with the detector, resulting in the missing momentum shown as a white dotted line. A secondary particle, a pion shown as green curve, can leave energy deposits to each sensor in the tracker, but it is difficult to reconstruct as a track due to the tiny momentum.

1.7 Previous disappearing-track search

The disappearing-track searches were done by both ATLAS [20] and CMS [21] experiments. In these searches, signal events were triggered by initial-state-radiation jets and the missing transverse momentum toward the opposite side as shown in Fig. 1.6. Then the existence of disappearing tracks was required. As discussed above, the expected signal track length was so small that signal acceptance was very low. Figure 1.7 shows the results in Run 1 analyses in the ATLAS experiment and a Run 2 analysis using 38 fb^{-1} in the CMS experiment, where the ATLAS experiment used short tracks whose length was larger than 30 cm. These analyses had strong discovery potential for long-lived particles ($\gtrsim$5 ns) but did not have adequate sensitivity for particles with motivated lifetimes.

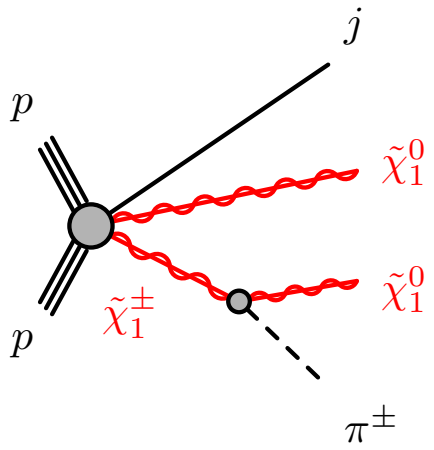

Figure 1.6: Diagrams of chargino-neutralino direct production with an association of one initial-radiation-jet.

The leading reason that the previous analyses had limited sensitivities for motivated lifetime predicted from the wino/higgsino LSP scenario is that they used the disappearing track signature longer than typical chargino decay lengths (O(1-10) cm). Since the charginos decay exponentially ($\frac{1}{c\tau\beta\gamma}e^{-r/c\tau\beta\gamma}$), where $\beta\gamma$ is a boost factor, signal acceptance for the disappearing track signature is also exponentially suppressed by the minimum reconstructable track length (R)

$$\text{acceptance} = \int_R^\infty \frac{1}{c\tau} e^{-r/c\tau} dr = e^{-R/c\tau}, \tag{1.21}$$

where assuming $\beta\gamma = 1$. Considering winos/higgsinos are expected to be heavy (O(0.1–1) TeV), the straightforward way to increase signal acceptance is to use shorter tracks than the previous ones.

One difficulty for the use of the short tracks is increasing fake tracks which are accidentally produced from a wrong combination of the hits in the tracker. The fake rate is decreased by using large numbers of hits because of the small probability that

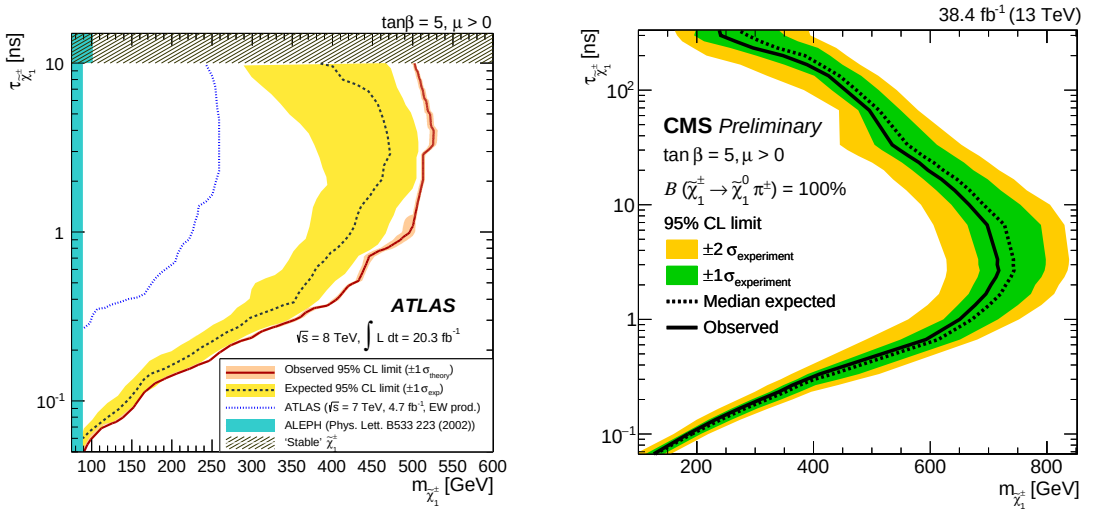

(a) (b)

Figure 1.7: Constraints for long-lived particles leaving disappearing track signature. (a) ATLAS Run 1 results [20]. (b) CMS Run 2 results [21].

all hits are consistently aligned. On the contrary, tracks with a small number of hits tend to be fake. The requirement on the minimum number of hits is determined by a trade-off between the signal acceptance and the fake rates. The ATLAS Run 1 analysis used short tracks reconstructed from at least five hits, which consists of three Pixel hits and two SCT hits[1], as shown in Fig. 1.8, resulting in the track length of larger than 30 cm and low sensitivity for charginos with their decay lengths of O(1–10) cm.

1.8 New tracking technique for long-lived particles

The ATLAS detector was upgraded in the long-shutdown in 2013–2014, and a new layer of the inner tracker was installed at the nearest position to the beam pipe. This enabled us to reconstruct shorter tracks, called pixel-tracklets, than those used in Run 1 analysis as shown in Fig. 1.8. Pixel-tracklets consist of four Pixel hits, instead of three Pixel hits and two SCT hits, resulting in a higher signal acceptance with a comparable fake track rate due to their short track length of around 12 cm. The use of pixel-tracklets increases the signal acceptance by a factor of seven compared to Run 1 analysis for the wino LSP scenario as shown in Fig. 1.9. On the other hand, new tracks require to modify the background estimation technique because the smaller track length leads to the worse momentum resolution. This thesis focuses on the significant improvement of signal tracks acceptance by the pixel-tracklets and shows the latest results which are most sensitive to the wino/higgsino LSP scenario, using 80 fb^{-1} of pp collision data

[1]Two SCT hits correspond to a three-dimensional measurement on one SCT layer because SCT detector is a double-sided strip detector.

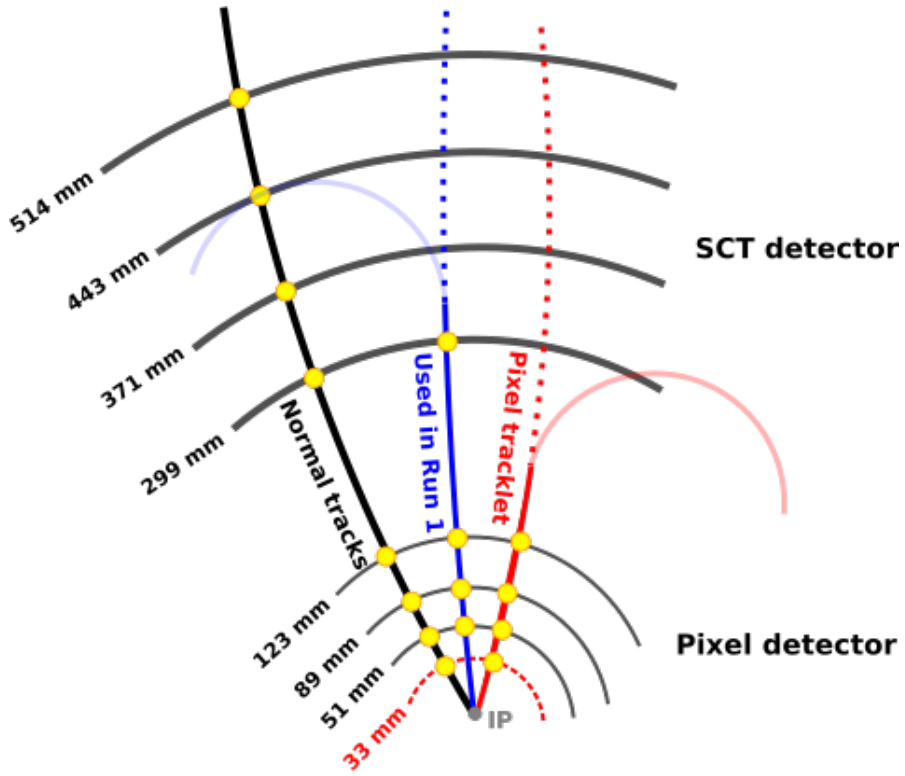

Figure 1.8: Illustration of tracks in the ATLAS detector. Inner three (four) layers are the Pixel detector, and the outer four layers are the SCT detectors. The yellow points represent hits in each layer. A black line shows the normal length track which consists of full hits in the tracker. A blue line shows a short track used in Run 1 analysis, where a track is made by three Pixel hits and two SCT hits. A red line shows a new short track (pixel tracklet), which consists of four Pixel hits. The pixel tracklet reconstruction became possible thanks to new Pixel-layer shown as red dashed line.

collected by the LHC/ATLAS experiments at $\sqrt{s} = 13$ TeV.

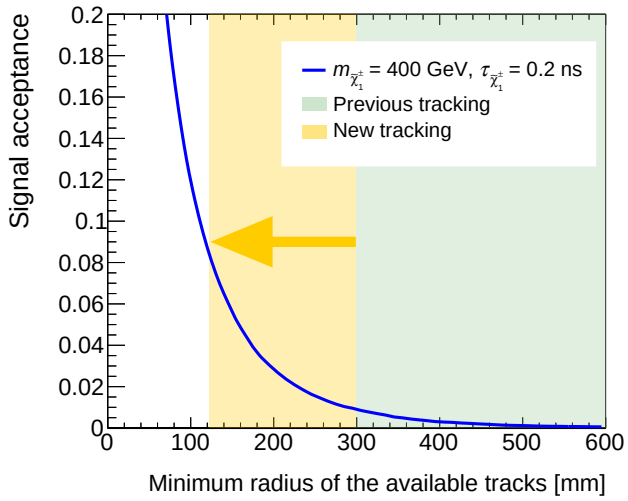

Figure 1.9: Signal acceptance as a function of the threshold on the chargino decay radius above which the chargino tracks are assumed to be fully reconstructed. A blue line shows the signal acceptance for a wino with a mass of 400 GeV and a lifetime of 0.2 ns. A green region corresponds to the track radius used in the ATLAS Run 1 analysis. A Yellow region corresponds to the track radius used in this thesis.

1.9 Contents of this thesis

This thesis presents a significant improvement in the search for supersymmetric particles using data recorded in 2015–2017 with the ATLAS detector. After introducing the ATLAS detector (Chapter 2), data and simulated samples used in this search (Chapter 3) and object reconstruction technique (Chapter 4), the short-track reconstruction is discussed in Chapter 5. An event selection to reduce background with keeping signal events are discussed in Chapter 6. The Chapter 7 discusses the evaluation method of the remaining number of events after the selections by categorising the background sources. Introducing the statistical procedure for an evaluation of the number of signal events in Chapter 8 and discussing its systematic uncertainties in Chapter 9, the results are shown in Chapter 10. In the last Chapter 11, the interpretation of the results and future prospects by a next-generation collider are discussed.

Chapter 2

LHC and ATLAS detector

2.1 Large Hadron Collider

The Large Hadron Collider (LHC) [22] is a two-ring-superconducting-hadron accelerator and collider installed in the 27 km tunnel used for Large-Electron-Positron (LEP) machine. It was designed to collide proton beams with a centre of mass energy of 14 TeV and the peak luminosity of 10^{34} cm^{-2}s^{-1}.

The beam injecting to the LHC is successively accelerated: up to 50 MeV by Linac2, 1.4 GeV by Proton Synchrotron Booster (PSB), 25 GeV by Proton Synchrotron (PS), 450 GeV by Super Proton Synchrotron (SPS) and finally the LHC accelerates the beam up to 7 TeV.

The LHC uses 1232 main superconducting dipole magnets based on NbTi cables as a bending magnet cooling to 1.9 K in superfluid helium, operating at fields up to 8.33 T as a designed value. The LHC proton beam consists of 39 batches (bunch-trains), which are filled 72 bunches with 25 ns spacing, resulting in 2808 bunches in total. The bunch structure flexibly changes depending on the beam condition as summarised in Table 2.1. Each bunch has 1.2×10^{11} protons as a designed nominal value, and then luminosity becomes to 10^{34} cm^{-2}s^{-1}.

The LHC started a pp run from 2010 to 2012 with $\sqrt{s} = 7$ TeV (2010 and 2011) and $\sqrt{s} = 8$ TeV (2012), which is called Run 1. After upgrading the accelerators and detectors, the LHC restarted the operation from 2015 with $\sqrt{s} = 13$ TeV, called Run 2.

The peak luminosity of the pp collision was designed to 1×10^{34} cm^{-2}s^{-1} as nominal values, and 2.5×10^{34} cm^{-2}s^{-1} as ultimate values, while the peak luminosity in Run 2 reached 2.09×10^{34} cm^{-2}s^{-1} (Maximum average events per bunch crossing is 79.8) at 2017 run (Table 2.1). The maximum number of bunches was designed as 2808, while 2544 was recorded in 2017.

There are four large experiments using the LHC: ATLAS [23], CMS [24], ALICE [25] and LHCb [26], and each experiment put a detector at the collision points. The ATLAS detector and the CMS detector are multi-purpose detectors, which aim for a precise measurement of the SM and a discovery of the BSM particles. ALICE (LHCb) is designed for a detailed study of nuclear physics (B-physics).

Values	Design	2012 Run	Run 2
Beam energy [TeV]	7	4	6.5
Luminosity $\times 10^3$ [cm^{-2}s^{-1}]	1 (2.5)	0.8	2.1
Number of bunches	2808	1380	2544
Bunch spacing [ns]	25	50	25

Table 2.1: The LHC beam parameters as a designed value, Run 1 value (2012) and Run 2 value.

2.2 ATLAS detector

A Toroidal LHC ApparatuS (ATLAS) is a general-purpose detector designed for covering much of the new phenomena at TeV scale. For detection of rare processes from the enormous amount of hadronic collisions due to the high beam intensity, the detector is required to be fast and radiation-hard, and to have a high granularity and a large azimuthal angle coverage. The detector consists of subcomponents: inner detector, solenoid magnet, calorimeter, toroidal magnet and muon spectrometer. Figure 2.1 shows a layout of the ATLAS detector.

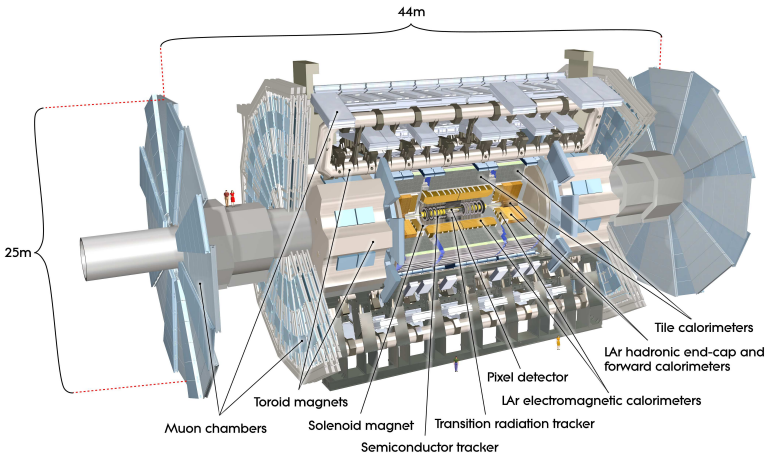

Figure 2.1: Overview of the ATLAS detector [23]. It has 25 m height, 40 m length and 7000 tonnes weight.

2.2.1 Coordinate

The ATLAS experiment uses a right-handed Cartesian coordinate system (x, y, z) where its origin is set at the nominal pp interaction point, the x-axis points to the centre of the LHC ring, the y-axis points upward, and z-axis directs to beam axis. Additionally,

a spherical coordinate system (r, θ, ϕ) is used as defined

$$r = \sqrt{x^2 + y^2} \tag{2.1}$$
$$\theta = \arctan\left(\frac{r}{z}\right) \tag{2.2}$$
$$\phi = \arctan\left(\frac{y}{x}\right). \tag{2.3}$$

Hadron collider often uses the transverse observables, such as transverse momentum $p_T = p\sin\theta$. It is because the vector sum of the momentum at the transverse plane is conserved, while one at longitudinal planes is not conserved due to the fluctuation of parton energy in protons. As related to it, particles produced in pp collisions are often highly boosting along the z-axis. In this case, it is useful to use the rapidity (y) defined as

$$y = \frac{1}{2}\ln\left(\frac{E + p_z}{E - p_z}\right), \tag{2.4}$$

where E and p_z are the energy and longitudinal momentum, respectively. Since the rapidity difference (Δy) is Lorenz-invariant, it is easy to grasp the event topology at a mass-frame. Since the rapidity needs the mass information, the pseudorapidity (η), which is a massless limit of the rapidity, as represented

$$\eta = -\ln\left(\tan\frac{\theta}{2}\right) \tag{2.5}$$

is normally used instead of θ. By using η and ϕ, the angular distance between two particles is defined as

$$\Delta R = \sqrt{(\Delta\eta)^2 + (\Delta\phi)^2}. \tag{2.6}$$

2.2.2 Inner detector

The ATLAS inner detector consists of three sub-detectors as shown in Fig. 2.2. Pixel detector is aligned nearest to the beam pipe, and has an advantage to well-measured the impact parameters. SCT detector covers the radii of 30–50 cm, and can find the charged tracks together with the Pixel detector. TRT covers an outermost region in the tracker up to 1 m, and possible to continuously measure the trajectory. Surrounding the inner detector, solenoid magnet provides a uniform magnetic field within the tracker to measure the transverse momentum of the charged particles.

In order to reduce the scattering with the material, the amount of material in the tracker system is kept at low level as shown in Fig. 2.3, and is also precisely measured using hadronic scattering [27].

Solenoid magnet

One of the aims of the tracker is to measure the momentum of charged particles. By bending the charged particles with the strong magnetic field, the momentum can be evaluated from the curvature of the tracks. The superconducting solenoid magnet, which

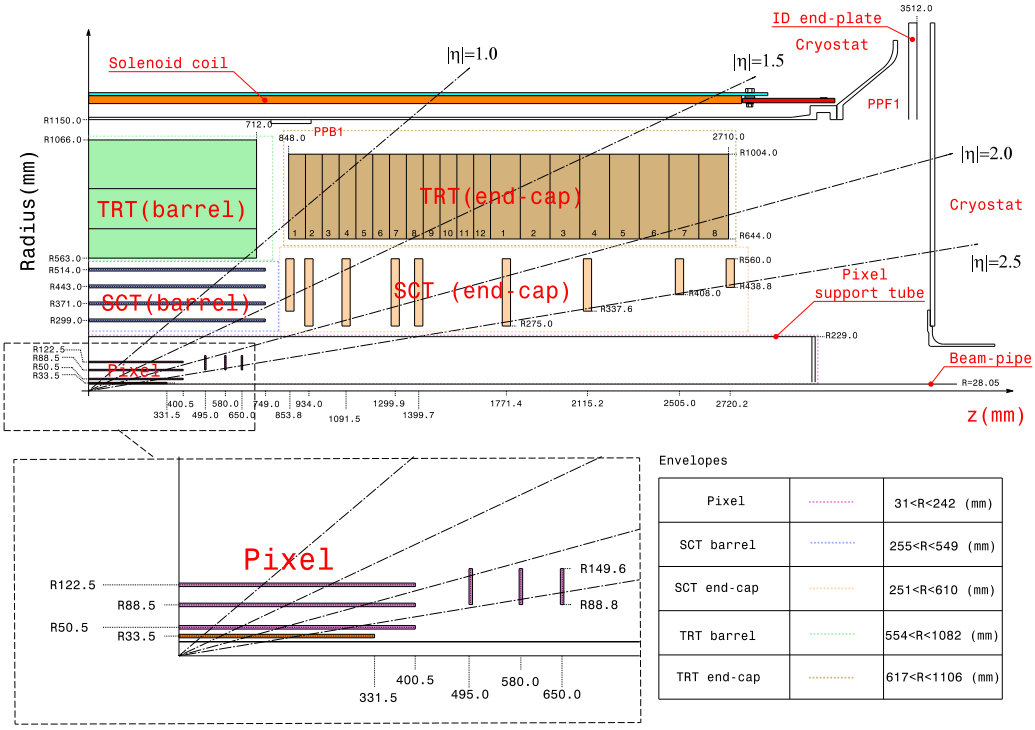

Figure 2.2: The layout of the inner detector [27].

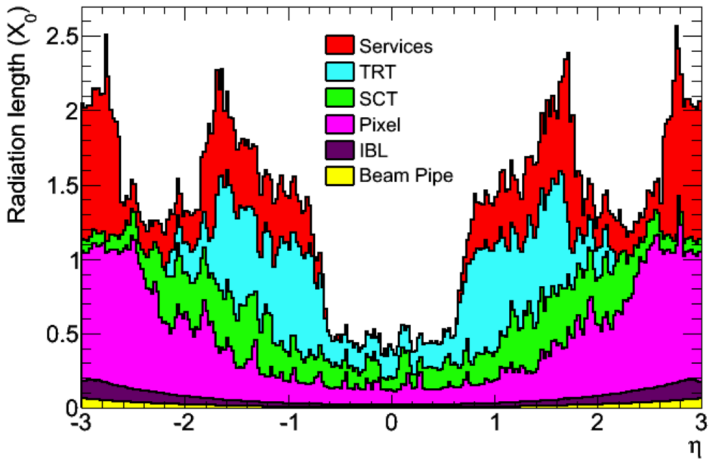

Figure 2.3: Radiation length as a function of η for the whole inner detectors [28]

surrounds the inner detector, provides a 2 T magnetic field along the beam axis and ability of a momentum measurement. The coil of the magnet is made of Al-stabilised NbTi, and the material thickness is kept at a low level (0.66 X_0 radiation length) in order to avoid a decrease of calorimeter performance.

The magnetic fields ($\boldsymbol{B}_z$, $\boldsymbol{B}_R$ and $\boldsymbol{B}_\phi$) are measured with the accuracy of less than 1 mT using 3D Hall cards as shown in Fig. 2.4.

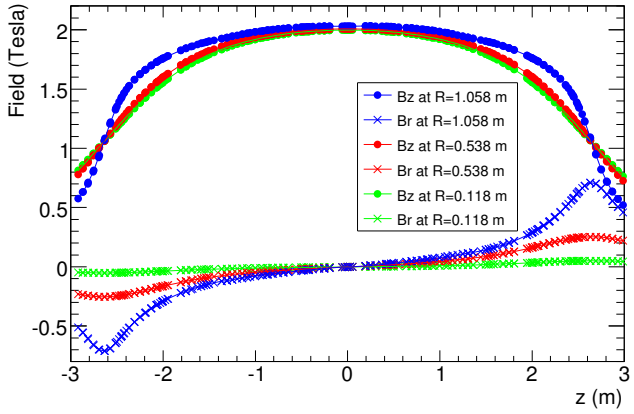

Figure 2.4: Measured magnetic field provided by the solenoid magnet as a function of z at three radii [23].

Pixel detector

The Pixel detector consists of four barrel-layers placed at radii of 33.5 mm, 50.5 mm, 88.5 mm and 122.5 mm, and three end-cap layers placed at z-positions of 495 mm, 580 mm and 650 mm. The barrel layers cover up to $|\eta| = 1.9$, and the end-cap layers covers up to $|\eta| = 2.5$. The innermost barrel layer, called Insertable B-Layer (IBL) [28], was installed after Run 1 in order to improve the tracking performance, then used from 2015. The total radiation length in the Pixel detector is shown in Fig. 2.5.

The sensor consists of a 250 μm thick n-bulk with 47232 (144 columns $\times$ 328 rows) readout pixels on the n^+-implanted side. Most of the pixels have the pitch of 50 $\times$ 400 μm^2, the remaining ones have longer pitches of 50×600 μm^2, and the pixels in the IBL have smaller pitches of 50×250 μm^2. Due to the technical requirement, some pixels near the edge of the frond-end chips share the one readout with the other pixels, which are called ganged-pixels. Although the sharing readout leads to ghost sensor hits, the ambiguity of the ganged-pixels can be resolved using consistency with other pixel hits at track reconstruction steps.

The charge deposit at each pixel (IBL) is measured as 8 (4)-bit dynamic range information by counting the number of clocks where the signal is above a threshold, which is called Time-over-Threshold (ToT). The ToT information of each pixel is used in the determination of the position passed by the charged particles.

The spatial resolution at each layer is 10 μm (r-ϕ) in both barrel and end-cap layers, 115 μm (z) in the barrel layers, and 115 μm (r) in the end-cap layers.

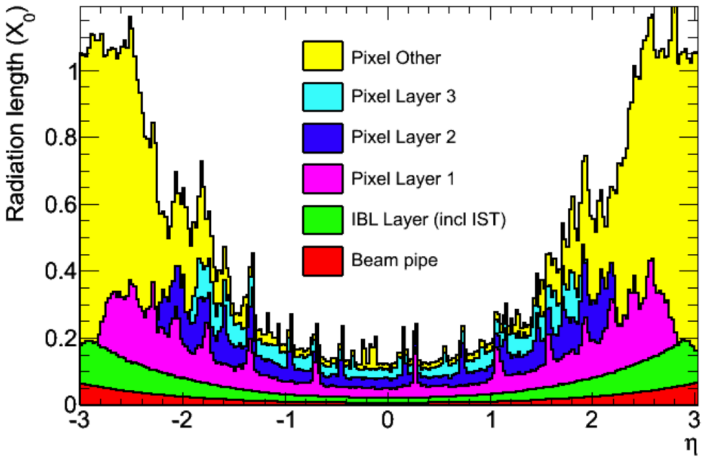

Figure 2.5: Radiation length as a function of η for the whole Pixel detectors [28]

Semiconductor tracker

The semiconductor tracker (SCT) consists of micro-strip silicon sensors and surrounds Pixel detectors. SCT consists of four barrel-layers placed at radii of 299 mm, 371 mm, 443 mm and 514 mm covering up to $|\eta| = 1.1$, and two end-caps containing nine disks placed at z-position between 854 mm and 2720 mm covering up to $|\eta| = 2.5$. The sensors are single-sided p-in-n sensors with 80 μm pitch, and two strip sensors are piled as a pair. Each sensor in a pair is integrated with rotating by $\pm$20 mrad each other, resulting in a capability to measure the passed position along the strip orientation. The spatial resolution is 17 μm in r-ϕ plane and 580 μm in the z (r)-direction for a barrel (end-cap) layers.

Transition Radiation tracker

The transition radiation tracker (TRT) is a gas straw-tube detector using transition radiation for particle identification. The drift tubes are made by multi-layer polyimide film with coated by graphite-polyimide, aluminium and polyurethane, and are filled with Xe-based gas mixture. Drifting electrons are collected by anode made of a tungsten wire plated with gold, and the operational drift-time accuracy is 130 μm. The straw tubes are of 4 mm diameter and align with a mean spacing of 7 mm. A transition radiator material is a 19 μm-diameter polypropylene fibre for a barrel sector and a 15 μm thick polypropylene radiator foil separated by a polypropylene net for an end-cap sector, surrounding the straws.

The TRT barrel sector is located at radii from 554 mm to 1082 mm and covering up to $|\eta| = 1.0$, and the end-cap sectors covers up to $|\eta| = 2.0$. The barrel sector contains 73 layers of straws for the radius direction, and the end-cap sectors contain 160 straw planes along to beam-axis. Charged tracks traverse at least 36 straws in the barrel or end-cap region, on the other hand, the tracks passing barrel-end-cap transition region ($0.8 < |\eta| < 1.0$) traverse the smaller number of straws of at least 22 straws due to the gap between the barrel and the end-cap modules.

Since there are two mechanisms producing two different amount of energy deposit (ionisation and transition radiation), two different thresholds are used for recording the time over thresholds. Higher thresholds are used to separate electrons and other particles. Electrons emit higher energies as the transition radiation because of the large γ factor (p/m). Electrons traversing the straw leave longer time over thresholds for the higher threshold, resulting in strong discriminants for the separation of electrons and other particles, especially pions.

2.2.3 Calorimeter

ATLAS has two types of sampling calorimeters for electromagnetic and hadronic measurements with a full ϕ-symmetry. Figure 2.6 shows the layout of the ATLAS calorimeter system. Most parts of the calorimeter use liquid argon (LAr) as the active matter because it has a good linearity, a stability of response over time and radiation-hardness, while the barrel hadron calorimeter uses scintillating tiles as the active material because of the low cost.

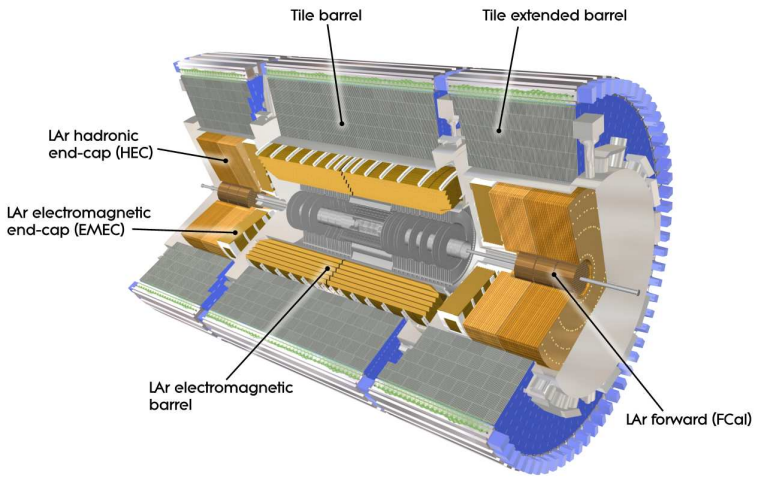

Figure 2.6: The layout of the ATLAS calorimeter [23].

Electromagnetic calorimeter

The electromagnetic (EM) calorimeter aims to measure the energies of electrons and photons with a precise resolution. There are two structures: the barrel EM calorimeter and the end-cap EM calorimeters, that cover central region ($|\eta| < 1.475$) and forward region ($1.375 < |\eta| < 3.2$), respectively. The detectors have an accordion-shaped structure to provide complete ϕ symmetry, are filled with liquid-argon as active matter and use lead as an absorber. Radiation length is shown in Fig. 2.7.

The each EM calorimeter consists of three layers. The first layer is finely segmented in η ($\Delta\eta$ =0.003 for barrel, $\Delta\eta$ =0.003–0.006 for end-cap). This layer is designed for a good separation of the γ/π^0. This layer is prepared in only a small η region ($|\eta| < 2.5$). The second layer has a large radiation length (16 X_0 at η =0) and collects large fractions of the energy. The granularity of the cell is $\Delta\eta \times \Delta\phi = 0.025 \times 0.025$. The third layer collects the tail of the shower, and the granularity in η is twice coarser than the second layer. A transition region ($1.35 < |\eta| < 1.5$) does not have the third layer. Additionally a presampler, thin liquid-argon layer, is placed in front of the first layer: all η coverage for barrel region and $1.5 < |\eta| < 1.8$ for end-cap. This layer enables to estimate the energy loss before the calorimeter and improve the energy resolution of the electromagnetic calorimeter.

Energy resolution measured using electron/positron test-beam as a function of energy in the range from 10 GeV to 245 GeV at $\eta = 0.687$ is

$$\frac{\sigma(E)}{E} = \frac{10\%}{\sqrt{E(\mathrm{GeV})}} \oplus 0.17\%, \tag{2.7}$$

and linearity ($E_{\mathrm{obs}}/E_{\mathrm{beam}}$) is within $\pm$ 0.1% in the energy range from 15 GeV to 180 GeV.

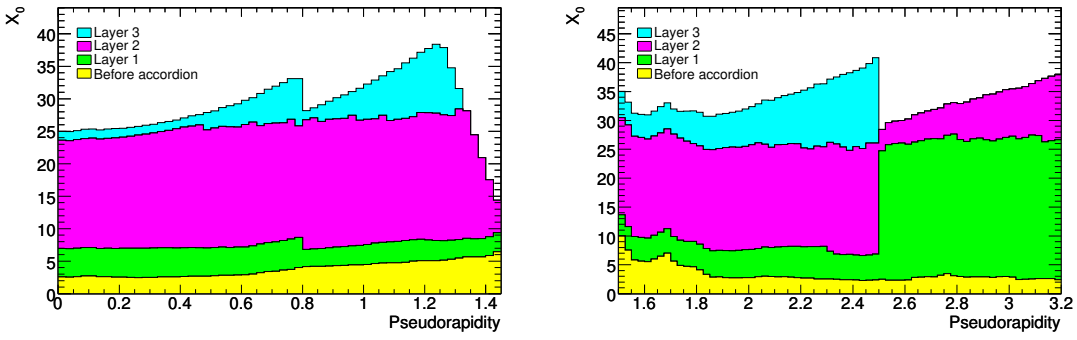

(a) (b)

Figure 2.7: Radiation length in the electromagnetic calorimeter as a function of η for (a) barrel region and (b) end-cap region [23].

Hadronic calorimeter

The hadronic calorimeter consists of three types of sub-detectors: the tile calorimeter, the liquid-argon hadronic end-cap calorimeter and the liquid-argon forward calorimeter. Interaction length of the hadronic calorimeter is shown in Fig. 2.8.

Tile calorimeter is located outside the EM calorimeter in the barrel region ($|\eta| < 1.0$), and in the extended barrel region ($0.8 < |\eta| < 1.7$). It is a sampling calorimeter using steel as the absorber and scintillating tiles as active material. Each barrel consists of 64 modules of $\Delta\phi \sim 0.1$, and each module forms periodic structure with a ratio of 4.7:1 for steel plates and scintillating tiles. Interaction length is about 7.4 λ. A fractional energy resolution for pions at $|\eta| = 0.35$ is

$$\frac{\sigma(E)}{E} = \frac{56\%}{\sqrt{E(\mathrm{GeV})}} \oplus 6\%. \tag{2.8}$$

The hadronic end-cap calorimeter (HEC) is located behind the end-cap EM calorimeter, covering $1.5 < |\eta| < 3.2$. It is a sampling calorimeter using copper as absorber and filled with liquid-argon as active material. The material was chosen for radiation hardness. HEC consists of two wheels in each side, and each wheels consists of 32 modules. The thickness of copper plates of the rear wheels is double of the front wheels, resulting in smaller sampling fractions than the front wheels. A readout cell size of each module is $\Delta\eta \times \Delta\phi = 0.1 \times 0.1$ for $|\eta| < 2.5$ and 0.2×0.2 for larger $|\eta|$. An energy resolution using the electromagnetic end-cap calorimeter and the HEC using π^- (π^+) test-beam in 2002 is

$$\frac{\sigma(E)}{E} = \frac{85\ (82)\%}{\sqrt{E(\mathrm{GeV})}}. \tag{2.9}$$

The forward calorimeter (FCal) is located at forward region, with a coverage over $|\eta| < 4.9$. It consists of three modules. The first module (FCal1) is optimised for electromagnetic measurements and made of copper to optimise the resolution. Other two modules (FCal2 and FCal3) are optimised for hadronic interactions and made of tungsten to minimise the lateral spread of hadronic showers. All modules use LAr as active matter. A shielding plug is installed behind FCal3 to suppress backgrounds in the muon system. The thickness of the FCal is approximately 10 λ. An energy resolution measured by test-beam in 2003 for electrons is

$$\frac{\sigma(E)}{E} = \frac{29\%}{\sqrt{E(\mathrm{GeV})}} \oplus 4\%, \tag{2.10}$$

and for pions

$$\frac{\sigma(E)}{E} = \frac{70\%}{\sqrt{E(\mathrm{GeV})}} \oplus 3\%. \tag{2.11}$$

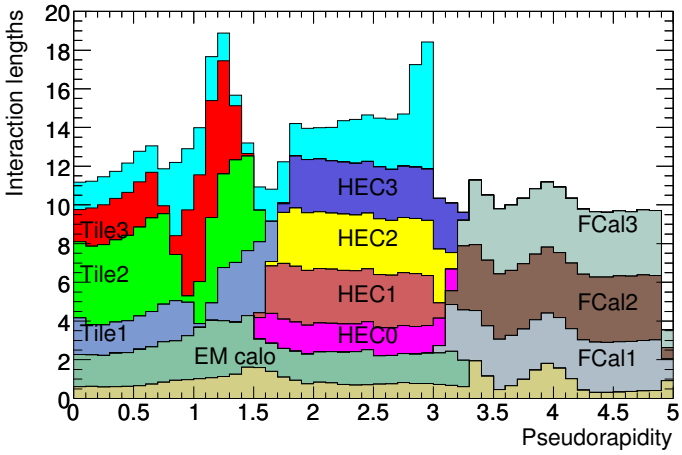

Figure 2.8: Interaction length in the calorimeter as a function of η [23].

2.2.4 Muon system

The muon system consists of four sub-detectors: Two are for triggering and others are for precision tracking as shown in Fig. 2.9. There is a gap at $|\eta| \approx 0$ due to the service of the solenoid magnet, the calorimeter and the inner detector. The maximum gap is 1–2 m, corresponding to $|\eta| < 0.08$ for high p_{T} muons. Therefore, a muon passing to this gap cannot be reconstructed as a muon spectrometer track.

Muon p_{T} is measured by bending the muon using the air-core toroid magnets locating inner of the muon spectrometers.

Toroidal magnet

Magnets for muon tracking consists of one barrel toroid and two end-cap toroid magnets, which consist of eight coils made of Al-stabilised Nb/Ti/Cu and surrounding the calorimeters as shown in Fig. 2.10 (a). They are aligned to cover whole η region up to $|\eta| < 2.7$. A magnetic field is optimised to bend any muons in the acceptance, and the integrated field strength ($\int Bdl$) is 1.5 T·m to 5.5 T·m for barrel region and 1 T·m to 7.5 T·m for end-cap region, while transition regions ($1.4 < |\eta| < 1.6$) has lower bending power as shown in Fig. 2.10 (b).

Precision tracking

Monitored drift tube (MDT) is the main part of the muon system for precise muon tracking. MDT consists of three layers (r = 5 m, 7.5 m and 10 m) for barrel, and four layers ($|z|$ = 7.4 m, 10.8 m, 14 m and 21.5 m) for end-cap region, covering $|\eta| < 2.7$ except for the innermost layer in the end-cap region. Each MDT chamber has two multi-layers, which consists of three or four tubes, and has four optical rays to monitor alignment of the tubes. Tubes are made of a pressurised aluminium drift tube with a

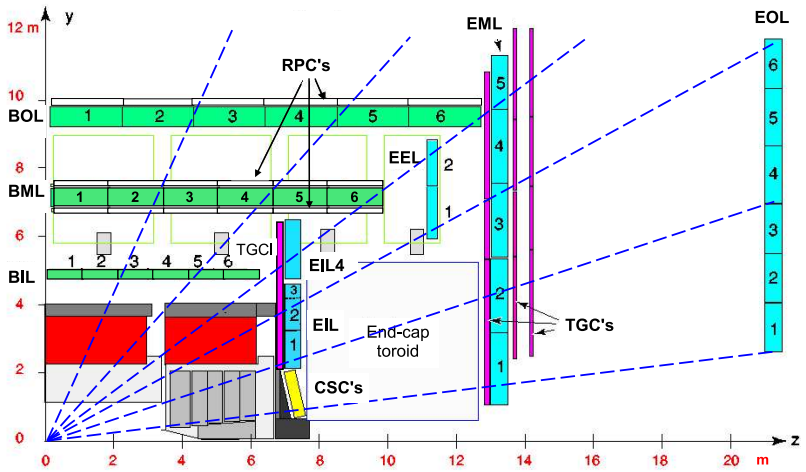

Figure 2.9: A layout of the muon system [23]. The three letters in each layer refer to barrel (B), end-cap (E), inner (I), middle (M), outer(O), large (L) and small (S).

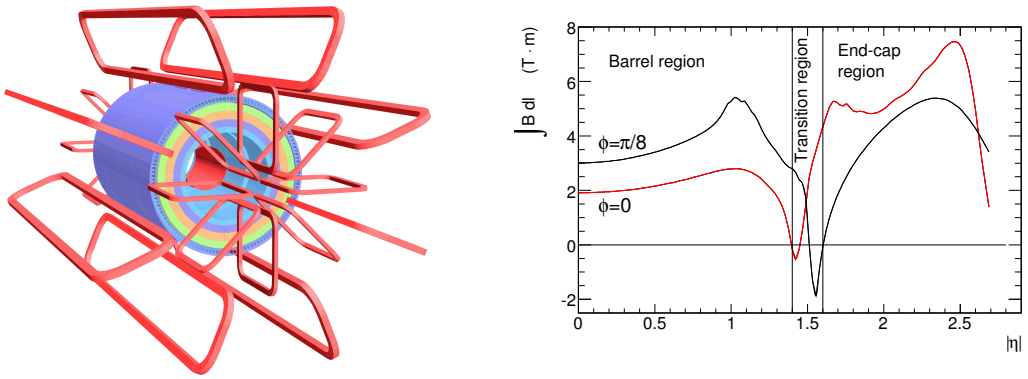

(a) (b)

Figure 2.10: (a) Magnet systems of the ATLAS detector. Outer red components are toroidal magnets [23]. (b) A magnetic field of toroidal magnets [23].

diameter of 30 mm, Ar/CO_2 gas and gold-plated tungsten-rhenium anode wire. Each tube is aligned along ϕ for both barrel and end-cap, then have a good resolution 35 μm for z-position.

MDTs in the first layer of end-caps in a high η region ($2 < |\eta| < 2.7$) are replaced by Cathode strip chamber (CSC) in order to withstand a high counting rate. CSC on each end-cap side consists of eight big chambers and eight small chambers which contain four CSC planes. CSC is multiwire proportional chambers having two oriented cathodes. One cathode is segmented perpendicular (bending plane) to the wires, and other is parallel (non-bending plane) to the wires with coarser pitches, resulting in spatial resolution of 40 μm for r, and 5 mm for ϕ.

Triggering

Resistive plate chamber (RPC) is a gas parallel electrode-place detector. Two plates are parallel to each other at a distance of 2 mm with electric field of 4.9 kV/mm, then the signal is read out via two orthogonal sets of strips for η and ϕ with a pitch of 23–35 mm, resulting in spatial resolution of 10 mm for z, 10 mm for ϕ and good time resolution of 1.5 ns. Information about ϕ position is also used in the precise tracking with MDT's precise r-position information. RPC consists of three layers: two layers sandwich the second layer of MDT, and one layer is located outer the third layer of MDT, and covering $|\eta| < 1.05$.

Thin gap chamber (TGC) is a multi-wire proportional chamber with small wire-to-cathode distance (thin gap) and highly quenching gas mixture of CO_2 and n-C_5H_{12}, leading to a good time resolution of 4 ns. The r-position is measured by wire groups, while the ϕ-position is measured by the radial strips. For a requirement on a good granularity at a high η region, the size of wire groups varies as a function of η, resulting in a good granularity of 2–3 mrad from the interaction point. TGC consists of four layers: the one layer (triplet) is in front of the second MDT wheel and two layers (doublets) are behind the second MDT wheel, while the fourth layer (doublet) is in front of the first MDT wheel, covering $1.05 < |\eta| < 2.4$. TGCs give complemental information about the non-bending plane alternative to MDTs.

2.2.5 Luminosity detector

Luminosity measurement using Cerenkov Integrating Detector-2 (LUCID-2) [29] is a luminosity detector installed in 2014 as an upgraded detector from LUCID. LUCID-2 modules are installed at both end-cap sides, and each module consists of 16+4 photomultipliers: 16 photomultipliers with thin quartz windows as Cherenkov medium are arranged around the beam-pipe with a distance of 13 cm from the beam line and 17 m away from the interaction point, and other four photomultipliers using quartz fibres as Cherenkov medium are put 1.5 m away from the LUCID detector. The calibration and monitoring the gain stability was done using ^{207}Bi sources, LED or LASER signals.

The average luminosity is calculated from

$$L_{\text{ave}} = \frac{f_{\text{LHC}} \cdot n_b \cdot \mu^{\text{vis}}}{\sigma^{\text{vis}}}, \tag{2.12}$$

where f_{LHC} is the LHC revolution frequency (11 kHz), n_b is the number of colliding bunches ($\sim$2500), μ^{vis} is a visible number of interactions in a bunch and σ^{vis} is the visible cross-section. The luminosity can be determined by measuring μ^{vis} and σ^{vis}. μ^{vis} is measured by counting the number of signals above threshold in 60 seconds, assuming that the hit-counts follow a Poisson distribution, while absolute σ^{vis} is determined in van der Meer (vdM) fills [30] profiling beam densities [31].

2.2.6 Trigger and data acquisition system

The Trigger and Data Acquisition (TDAQ) system consists of two subsystems: the first-level trigger (L1) and the high-level trigger (HLT) [32].

L1 is a hardware-based trigger and filters the event from 40 MHz to 100 kHz. A central trigger processor in L1 decides the accept/reject using the information from the two logics (L1Calo and L1Muon), which handle the output of the calorimeter and the muon spectrometer respectively, then sends the accept-flag and Region-of-Interest (RoI) information to HLT. L1Calo trigger aims to identify electron/photon, hadronic-τ, jets and the missing transverse momentum. To efficiently and fast identify high energy objects, L1Calo segments the calorimeter cells into $(\eta \times \phi) \approx (0.1 \times 0.1)$ blocks, called trigger-tower, and calculate the energy, coordinate, object type and isolation based on the energy deposit in each trigger-tower. L1Muon trigger aims to identify high p_{T} muons from the interaction point and detects them by requiring a coincidence of hits in the different layers in RPC and TGC within the requiring curvature.

HLT is a software-based trigger and filters the event from 100 kHz to 1 kHz. Unlike the L1 trigger, HLT can use full information in the detector, that is fine granularity segmentation in the calorimeter, precise tracking in the muon spectrometer and the tracking information from the inner detector within RoI region, as a similar level as the offline reconstruction. The events accepted by the HLT are transferred to permanent storage and are applied a time-consuming object-reconstruction algorithm for physics analyses.

Chapter 3

Data and simulated samples

3.1 Data

This analysis is based on the pp collision data collected with the ATLAS detector at the LHC at $\sqrt{s} = 13$ TeV from 3rd June 2015 to 26th November 2017. Data quality was monitored at all times, then the data where the detector did not work at their desired performance were filtered out from the data for physics analyses.

3.1.1 Luminosity

The instantaneous luminosity was grown year by year as shown in Fig. 3.1. The peak luminosity in three years is 2.09 $\times 10^{34}$ cm^{-2}s^{-1}, which nearly reaches designed ultimate values (2.5 $\times 10^{34}$ cm^{-2}s^{-1}). The combined integrated luminosity in 2015–2017 being satisfied with good quality requirements mentioned above is 79.8 fb^{-1}, and the uncertainty is 2.0%. It is derived, following a methodology similar to that detailed in Ref. [31], from calibrations of the luminosity scale using x-y beam-separation scans performed in August 2015, May 2016 and July 2017.

3.1.2 Pile-up

When instantaneous luminosity increases, the number of pp interactions per bunch crossing also increases. Since the rate of the target process is generally rare, most of the pp interactions are not of interest, and they are called pile-up. Figure 3.2 shows a distribution of the number of pp interactions per bunch crossing in the data in 2015–2017. The mean number of interactions per crossing in 2017 data is much higher than the previous two years due to the high instantaneous luminosity operation. High luminosity operation increases the production rate of target signals, while degrades the physics performance, especially tracking performance. The quantitative effects are discussed in Sec. 5. The bump around $\mu = 60$ is due to luminosity levelling, which aims to avoid that instantaneous luminosity exceeds 1.5 $\times 10^{34}$ cm^{-2}s^{-1} and that the serious pile-up affects the trigger rate.

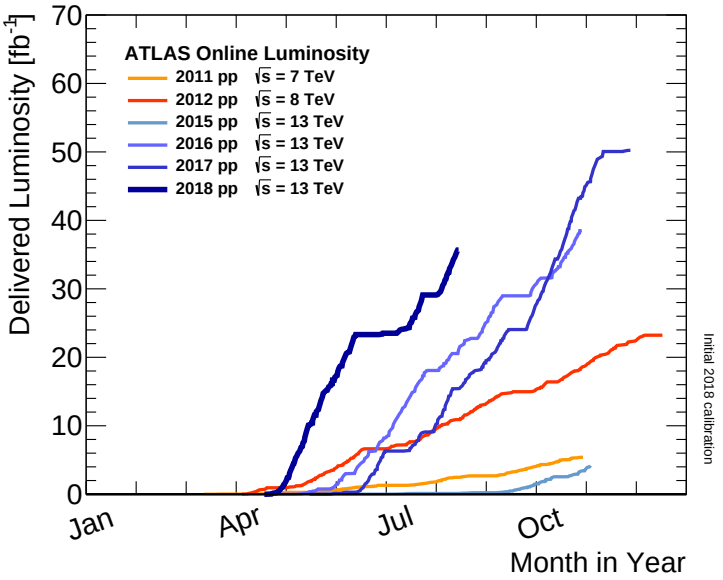

Figure 3.1: Cumulative luminosity in each year as a function of time.

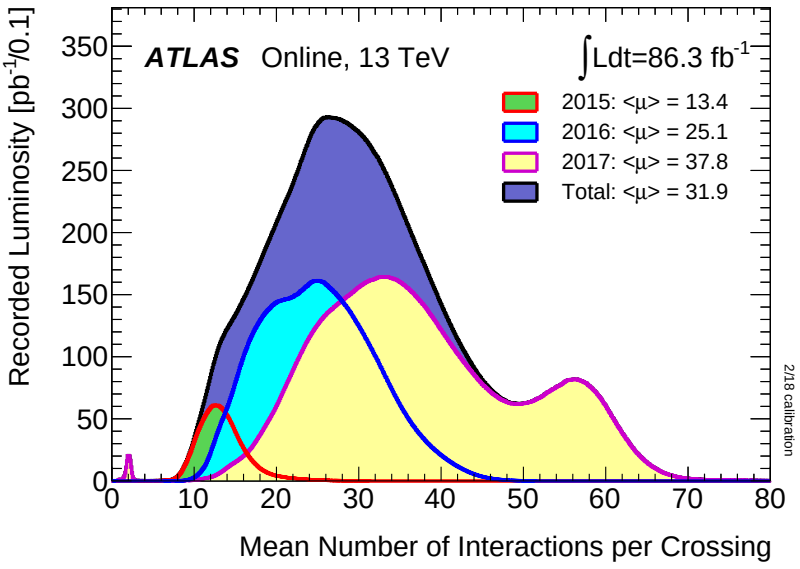

Figure 3.2: The luminosity-weighted distribution of the mean number of interactions per bunch crossing for 2015–2017 *pp* collision data.

3.2 Simulated samples

To validate the analysis method, Monte Carlo (MC) simulated samples are used. Samples were produced in some stages. At first, target elementary processes were created by event generators, which calculate a matrix element in *pp* collisions, then hadronic particles were simulated to reproduce parton showering and hadronisation. Second, a realistic response of the detector was simulated with GEANT4 [33–35], which simulates interactions of particles in processed events. In order to emulate pile-up effects correctly, minimum bias events were overlaid to each simulated samples, where minimum bias events were added to not only the same bunch crossing but also before and after the bunch crossing in order to emulate the effects from interactions in other bunch crossings. Overlaid minimum bias events were generated using PYTHIA 8.210 [36] and EVTGEN (v1.2.0) [37] with NNPDF2.3 LO PDF set [38] with A3 tune [39]. The number of overlaid minimum bias events in each bunch crossing was roughly set to match the observed pile-up distribution, and they were precisely tuned by applying an event-weight at the analysis step. After digitisation of GEANT4 simulation outputs, the particle reconstruction algorithms as described in Sec. 4 were applied for simulation samples as with the observed data. In order to minimise a difference between observed data and MC simulated samples, several corrections are applied to MC.

This section summarises the details of the event generator, parton showering and the hadronisation of the simulated samples.

3.2.1 Signal Monte Carlo sample

A mass spectrum of wino LSP models was calculated using the ISASUSY ver.7.80 [40] assuming minimal AMSB model with tan β=5, the sign of the higgsino mixing term (sign(μ)) set to be positive and the universal scalar mass set to m_0= 5 TeV. Gravitino mass ($m_{3/2}$) was selected to become charged wino mass to 91 GeV, 200 GeV, 300 GeV, 400 GeV, 500 GeV, 600 GeV, 700 GeV, 800 GeV and 900 GeV. For a mass spectrum of higgsino LSP models, charged higgsino masses were set to be 95 GeV, 100 GeV, 120 GeV, 140 GeV, 160 GeV and 200 GeV as a model parameter, and the neutral higgsino masses are set to appropriate values from the theory [14, 41]. Masses of other particles were set to be 40 TeV to be decoupled from the other particles. The signal samples were generated with up to two extra partons in the matrix element using MADGRAPH5_aMC@NLO 2.6.2 [42] at leading order (LO) interfaced to PYTHIA 8.230 [36] for parton showering and hadronisation. The NNPDF2.3 LO [38] parton distribution function (PDF) set was used with A14 tune [43]. A decay from chargino to neutralino was simulated in the GEANT4. The decay branching ratio of charginos were set to

$$\begin{aligned} Br(\tilde{\chi}_1^{\pm} \to \tilde{\chi}_1^0 \pi) &= 100.0\ (95.5)\% \\ Br(\tilde{\chi}_1^{\pm} \to \tilde{\chi}_1^0 e \nu_e) &= 0.0\ (3.0)\% \\ Br(\tilde{\chi}_1^{\pm} \to \tilde{\chi}_1^0 \mu \nu_\mu) &= 0.0\ (1.5)\%, \end{aligned}$$

where the values in parenthesis are for higgsinos. A secondary particle from chargino decay has quite a small momentum and is hard to be reconstructed as the tracks in the current tracking configuration. The signal acceptance is not affected from the decay branch. The effects from the difference of branching ratio between wino and higgsino were confirmed to be negligible by comparing both samples.

In order to reduce the meaningless events in the simulated samples, which are never triggered and left in the analysis dataset, events with low $E_{\mathrm{T}}^{\mathrm{miss}}$ were dropped before GEANT4 simulation. A threshold of $E_{\mathrm{T}}^{\mathrm{miss}}$ for the drop of events was set to 60 (50) GeV for wino (higgsino). The typical filter efficiencies were 20–50% for their mass. The thresholds are much lower than a threshold of $E_{\mathrm{T}}^{\mathrm{miss}}$ selection in kinematical selection (Sec. 6) and the events dropped by this filter were confirmed not to pass kinematical selection.

Cross-sections were calculated using RESUMMINO 2.0 [44–48] at NLO +NLL level. Figure 3.3 shows calculated cross-sections and uncertainties using CTEQ6.6 and MSTW2008 PDF sets at each chargino mass points. The final cross-sections and the uncertainties used in this analysis were evaluated from above two cross-sections from difference pdf sets as described at Ref. [49]. The central values were set to a centre of two uncertainties band, and the uncertainties were set to a difference between the central values and a maximum/minimum of uncertainty band as shown in Fig. 3.3, and summarised in Tables 3.1 and 3.2. For higgsinos, there are two neutralinos having the same mass because of the assumption of the decouple limit ($\mu \ll M_1, M_2$). The same production cross-sections as $\tilde{\chi}_1^+\tilde{\chi}_2^0$ and $\tilde{\chi}_1^-\tilde{\chi}_2^0$ are assigned to $\tilde{\chi}_1^+\tilde{\chi}_1^0$ and $\tilde{\chi}_1^-\tilde{\chi}_1^0$, respectively.

The lifetime of charginos strongly reflects from the signal model property and tightly relates with the signal acceptance in this analysis. It is necessary to precisely evaluate the signal discovery sensitivity as a function of the lifetimes. It is not efficient to produce chargino samples with precisely binning of the lifetime, because in most cases, a chargino in small lifetime samples is not reconstructed as tracks, then it is out of acceptance. In order to keep statistical uncertainties at a sufficiently low level, the chargino samples were produced by setting the lifetime to be large enough to keep signal acceptance, and then special weights were applied to be normalised samples to the correct pdf as follows

$$w(\tau_{\tilde{\chi}_1^\pm}) = \frac{f(\tau_{\tilde{\chi}_1^\pm})}{f(\tau_{MC})} \tag{3.1}$$

$$f(\tau) = \frac{1}{\tau}\exp\left(-\frac{t}{\tau}\right), \tag{3.2}$$

where t is a proper time of charginos for each event in simulated samples, $\tau_{\tilde{\chi}_1^\pm}$ is a lifetime of a target chargino and τ_{MC} is a lifetime in produced simulated samples. When there were two charginos, the events were applied to each weight respectively ($w = w(\tau_{\tilde{\chi}_1^\pm,1}) \cdot w(\tau_{\tilde{\chi}_1^\pm,2})$). Lifetime of the produced samples are 0.2 ns, 1.0 ns, 4.0 ns and 10.0 ns for wino and only 0.3 ns for higgsino. Since target lifetime for higgsino models are quite small, only one higgsino sample with small lifetime was created for each mass points. In order to emulate the signal samples with not-produced lifetime values (e.g. 0.4 ns), some samples with the same masses were merged, then treated as one samples, where the number of merged samples was limited to be at most two samples whose

lifetime is near the target signal to avoid a large statistical error from large extrapolation weights.

3.2.2 Monte Carlo samples of the Standard Model background

The simulated samples of the SM processes are used for validation of method, a fraction of remaining background components and some systematic uncertainties related to tracking properties. This analysis uses weak boson process ($pp \to W$, Z, WW, WZ and ZZ), t-quark production process ($pp \to t$, tW and $t\bar{t}$) and multi-jet events ($pp \to$ jet + jet). The cross-section of each process is summarised in Table 3.3.

Weak boson production

Weak boson production samples, containing W, Z and VV, were generated by SHERPA v2.2 [50] with NNPDF3.0 NNLO [51] PDF set, including parton showering and hadronisation. Each process was calculated at different accuracy for the number of additional partons as summarised in Table 3.4.

Cross-sections of single boson processes (W and Z) were calculated at NNLO accuracy in α_s using FEWZ [52]. Cross-sections of di-boson processes were calculated using SHERPA with the accuracy level of each production.

t-quark production

$t\bar{t}$ and single-t production with s-channel and W-boson-associated channel were generated by POWHEG-BOX 2 [53–56] with NNPDF3.0 NLO PDF set at NLO with h_{dump} parameter set to 1.5 m_{top}, interfaced to PYTHIA 8.230 with NNPDF2.3 LO with A14 tune. B-hadron decay was controlled by EVTGEN (v1.6.0) [37] instead of PYTHIA. Single-t production with t-channel was generated with a similar condition to other t samples except using NNPDF3.04f [51] PDF set to set to four-flavour scheme and except using MADSPIN [57] for t-quark decay to correctly model their spins.

The cross-section of the $t\bar{t}$ process was calculated at the NNLO+NNLL soft gluon resummation using TOP++V2.0 [58] assuming $m_t = 172.5$ GeV. A cross-section of single-t W-associated channel was calculated at approximate NNLO (NLO+NNLL) [59]. Cross-sections of single-t s/t-channels were calculated at NLO using Hathor v2.1 [60] [61].

Multi-jet events production

Multi-jet process and the cross-sections were generated by PYTHIA 8.186 replacing B-hadron decay by EVTGEN (v1.2.0) with NNPDF2.3 LO with A14 tune.

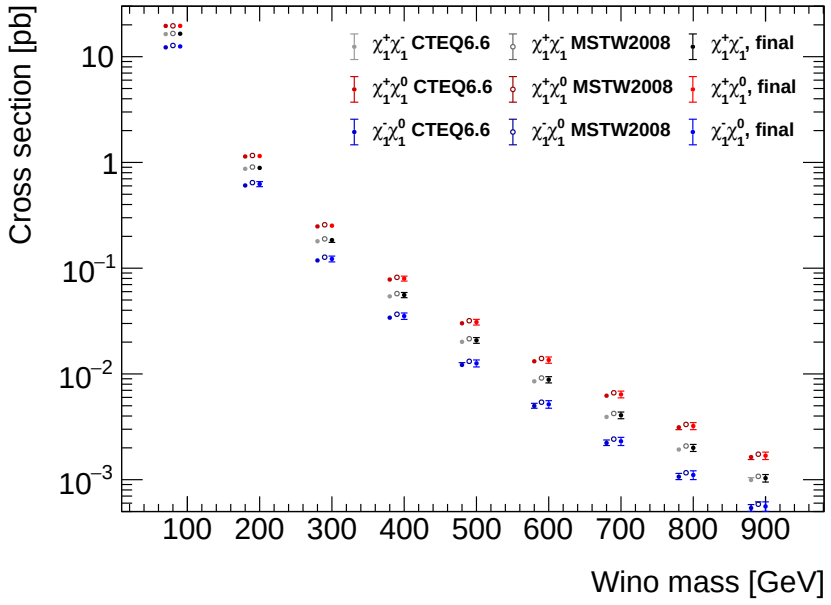

(a)

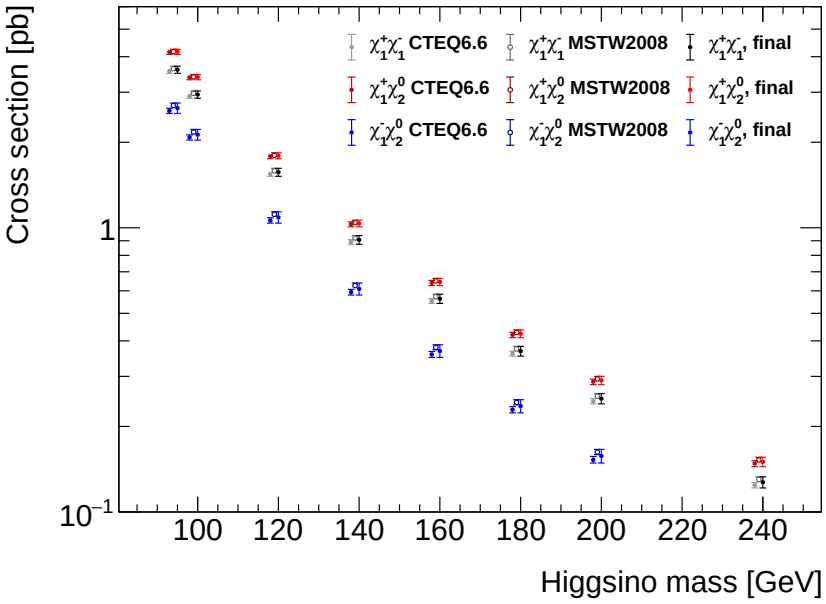

(b)

Figure 3.3: Calculated cross-section of chargino pair production. Left two points in each mass points are calculated with CTEQ6.6 (left) and MSTW2008 (centre) pdf set. Right points in each figures are final nominal value and uncertainties used in this analysis. (a) Wino LSP case. (b) Higgsino LSP case.

$\tilde{\chi}_1^{\pm}$ mass [GeV]	Process	$\sigma_{\text{NLO+NLL}}$ [pb]	Rel. unc.
91	$\tilde{\chi}_1^{\pm}\ \tilde{\chi}_1^{\mp}$	16.5	2.6%
91	$\tilde{\chi}_1^{+}\ \tilde{\chi}_1^{0}$	19.6	2.0%
91	$\tilde{\chi}_1^{-}\ \tilde{\chi}_1^{0}$	12.5	4.1%
200	$\tilde{\chi}_1^{\pm}\ \tilde{\chi}_1^{\mp}$	0.89	4.0%
200	$\tilde{\chi}_1^{+}\ \tilde{\chi}_1^{0}$	1.15	3.4%
200	$\tilde{\chi}_1^{-}\ \tilde{\chi}_1^{0}$	0.62	5.5%
300	$\tilde{\chi}_1^{\pm}\ \tilde{\chi}_1^{\mp}$	0.184	4.9%
300	$\tilde{\chi}_1^{+}\ \tilde{\chi}_1^{0}$	0.252	4.4%
300	$\tilde{\chi}_1^{-}\ \tilde{\chi}_1^{0}$	0.122	6.3%
400	$\tilde{\chi}_1^{\pm}\ \tilde{\chi}_1^{\mp}$	0.056	5.6%
400	$\tilde{\chi}_1^{+}\ \tilde{\chi}_1^{0}$	0.080	5.4%
400	$\tilde{\chi}_1^{-}\ \tilde{\chi}_1^{0}$	0.035	7.0%
500	$\tilde{\chi}_1^{\pm}\ \tilde{\chi}_1^{\mp}$	0.021	6.3%
500	$\tilde{\chi}_1^{+}\ \tilde{\chi}_1^{0}$	0.031	6.2%
500	$\tilde{\chi}_1^{-}\ \tilde{\chi}_1^{0}$	0.0126	7.6%
600	$\tilde{\chi}_1^{\pm}\ \tilde{\chi}_1^{\mp}$	0.0088	6.8%
600	$\tilde{\chi}_1^{+}\ \tilde{\chi}_1^{0}$	0.0135	6.8%
600	$\tilde{\chi}_1^{-}\ \tilde{\chi}_1^{0}$	0.0052	8.2%
700	$\tilde{\chi}_1^{\pm}\ \tilde{\chi}_1^{\mp}$	0.0041	7.3%
700	$\tilde{\chi}_1^{+}\ \tilde{\chi}_1^{0}$	0.0064	7.3%
700	$\tilde{\chi}_1^{-}\ \tilde{\chi}_1^{0}$	0.0023	8.9%
800	$\tilde{\chi}_1^{\pm}\ \tilde{\chi}_1^{\mp}$	0.0020	7.7%
800	$\tilde{\chi}_1^{+}\ \tilde{\chi}_1^{0}$	0.0032	7.7%
800	$\tilde{\chi}_1^{-}\ \tilde{\chi}_1^{0}$	0.0011	9.5%
900	$\tilde{\chi}_1^{\pm}\ \tilde{\chi}_1^{\mp}$	0.0010	8.2%
900	$\tilde{\chi}_1^{+}\ \tilde{\chi}_1^{0}$	0.0017	8.0%
900	$\tilde{\chi}_1^{-}\ \tilde{\chi}_1^{0}$	0.00056	10.3%

Table 3.1: Cross-section for wino direct pair production.

$\tilde{\chi}_1^{\pm}$ mass [GeV]	Process	$\sigma_{\text{NLO+NLL}}$ [pb]	Rel. unc.
95	$\tilde{\chi}_1^{\pm}\ \tilde{\chi}_1^{\mp}$	3.6	2.9%
95	$\tilde{\chi}_1^{+}\ \tilde{\chi}_2^{0}$	4.2	2.1%
95	$\tilde{\chi}_1^{-}\ \tilde{\chi}_2^{0}$	2.6	4.2%
100	$\tilde{\chi}_1^{\pm}\ \tilde{\chi}_1^{\mp}$	2.9	3.0%
100	$\tilde{\chi}_1^{+}\ \tilde{\chi}_2^{0}$	3.4	2.2%
100	$\tilde{\chi}_1^{-}\ \tilde{\chi}_2^{0}$	2.2	4.3%
120	$\tilde{\chi}_1^{\pm}\ \tilde{\chi}_1^{\mp}$	1.57	3.2%
120	$\tilde{\chi}_1^{+}\ \tilde{\chi}_2^{0}$	1.79	2.4%
120	$\tilde{\chi}_1^{-}\ \tilde{\chi}_2^{0}$	1.09	4.6%
140	$\tilde{\chi}_1^{\pm}\ \tilde{\chi}_1^{\mp}$	0.91	3.5%
140	$\tilde{\chi}_1^{+}\ \tilde{\chi}_2^{0}$	1.04	2.7%
140	$\tilde{\chi}_1^{-}\ \tilde{\chi}_2^{0}$	0.61	4.9%
160	$\tilde{\chi}_1^{\pm}\ \tilde{\chi}_1^{\mp}$	0.56	3.7%
160	$\tilde{\chi}_1^{+}\ \tilde{\chi}_2^{0}$	0.65	2.9%
160	$\tilde{\chi}_1^{-}\ \tilde{\chi}_2^{0}$	0.37	5.1%
200	$\tilde{\chi}_1^{\pm}\ \tilde{\chi}_1^{\mp}$	0.25	4.1%
200	$\tilde{\chi}_1^{+}\ \tilde{\chi}_2^{0}$	0.29	3.4%
200	$\tilde{\chi}_1^{-}\ \tilde{\chi}_2^{0}$	0.16	5.5%

Table 3.2: Cross-section for higgsino direct pair production.

Process	Decay	Order	Cross-section
W	$\ell\nu$	NNLO	60 nb
Z	$\ell\ell$	NNLO	6.3 nb
Z	$\nu\nu$	NNLO	11 nb
$t\bar{t}$	inclusive	NNLO+NNLL	832 pb
single t, s-channel	leptonic	NLO	3.4 pb
single t, Wt-channel	inclusive	NLO+NNLL	72 pb
single t, t-channel	leptonic	NLO	70 pb
VV	inclusive	NLO	100 pb
Loop-induced VV	inclusive	LO	2.4 pb
EW $VVjj$	inclusive	LO	0.24 pb
Multi-jet inelastic	inclusive	LO	77 mb

Table 3.3: Cross-sections of the SM processes.

Process	Generator (PDF)	Shower/Hadronisation (PDF)	accuracy
V (W and Z)	Sherpa (NNPDF3.0 NNLO)		NLO(0,1,2p), LO(3,4p)
V+jj (VBF)	Sherpa (NNPDF3.0 NNLO)		LO(0,1,2p)
VV	Sherpa (NNPDF3.0 NNLO)		NLO(0,1p), LO(2,3p)
Loop-induced VV	Sherpa (NNPDF3.0 NNLO)		LO(0,1p)
EW $VVjj$	Sherpa (NNPDF3.0 NNLO)		LO(0p)
t quark	Powheg (NNPDF3.0 NLO, (4f))	Pythia 8 (NNPDF2.3 LO, A14 tune)	NLO
Multi-jets	Pythia 8 (NNPDF2.3 LO, A14 tune)		NLO

Table 3.4: Summary of the generator configuration of the SM processes.

Chapter 4

Object reconstruction

This section discusses the way of the reconstruction of physics objects used in this analysis, which are tracks, vertices, jets, electrons/photons, muons and a missing transverse momentum.

4.1 Track

Passing through a sensor of the inner tracker, a charged particle leaves an energy deposit in each sensor. By connecting the several energy deposits, called "hits", a trajectory of the charged particle can be reconstructed. A reconstructed trajectory is called a track. Tracks have many information about the charged particles: a momentum, a direction and an impact parameter. Tracks have better momentum resolution, pointing resolution and a separation power from pile-up than calorimeter information.

There are two tracking strategies [62]: Inside-out and Outside-in. Most of the tracks are reconstructed in the former one, while the latter strategy recovers charged particles produced in flight from the interation points.

4.1.1 Inside-out track reconstruction

Inside-out strategy consists of four steps: the space-point creation, the seed-track creation, the ambiguity resolver and the TRT extension. In the earlier three steps, the tracks are created using only the silicon detector (Pixel and SCT). Then, the tracks are extrapolated to TRT detectors and merge the associated TRT hits.

Space-point creation

First, neighbouring silicon-sensor hits are merged into a cluster in order to determine a three-dimensional position of a charged particle passing across the sensors by using a connected component analysis (CCA) technique [63]. The cluster having a three-dimensional position is called a space-point. The position of each pixel sensor on a module is known, it is, therefore, straight forward to calculate a three-dimensional position. On the other hand, the space-points of SCT sensors, which are strip-type sensors, are constructed from the binded strips.

In a dense environment, clusters from two charged particles are close each other and often merged as one space-point. In the case that the one space-point is shared by multiple tracks, the neural-network technique ([64–66]) is used in order to identify the split of the space-point and to estimate the position and the uncertainty for each sub-clusters.

Seed-track creation

A seed-track is built by the combination of at least three space-points requiring several constraints on track parameters to reduce the number of seed-track candidates. Here three space-points are sequentially selected from only the SCT detector, only the Pixel detector and both Pixel and SCT detector, then an additional one space-point on the trajectory is required in order to reduce fake seed-tracks [67].

A seed-track is extrapolated using a combinatorial Kalman filter [68] and incorporates the space-points on the trajectory. In order to improve the purity of track candidates, merged hits are required to be consistent with the track trajectory.

Ambiguity resolver

The track candidates still contain many fake-tracks. In order not to consume unnecessary compute resources, the fake tracks are suppressed by the following strategy. First, track candidates are re-fitted with the detail material information. Although the fit-quality evaluated in the re-fitting provides a means of identifying fake tracks, the selection by only this variable is not sufficient for a reduction of fake tracks. As a second step, the goodness of track-candidates are evaluated by scoring the track-candidates using likelihood technique, which uses the several variables related to the tracks, e.g. the momentum, fit-quality, the number of associated hits and the number of holes[1]. After scoring all track-candidates, seed-tracks are sequentially regarded as track objects in the order of the score, where a shared hit is defined by checking if the hit in the track-candidate is used in the already-defined track objects. If the number of shared hits of a track-candidate is more than one, the track-candidate is rejected.

TRT extension

After the track reconstruction only with silicon hits, TRT hits are added to the tracks. By extrapolating the track to TRT detectors, the near TRT hits are added as TRT-hits candidates. Here in order to reduce the bad extrapolation with wrongly assigned TRT hits, a track without the extrapolation is kept if the score of it is higher than the extrapolated track.

4.1.2 Outside-in track reconstruction

Inside-out algorithm can reconstruct most of the charged particles from the interaction points. However, it assumes that charged particles leave the sufficient number of silicon hits, therefore it cannot work in the cases that silicon hits are intrinsically missing: e.g.

[1] A hole is defined as a missing expected hit on the trajectory

for the secondary particles from meta-stable particles and photon conversion. In order to reconstruct such tracks, TRT segments are used for seeding instead of hits in silicon detectors. Since the TRT detector consists of straw tubes, the space-points, which have three-dimensional position information, cannot be defined. Therefore, in the TRT case, the two-dimensional-planes, r-ϕ for a barrel region and r-z plane for an end-cap region, are used for the seed finding, then trajectory patterns are detected by using Hough transformation technique [69].

After finding the patterns, they are re-fitted using drift time, then they are extrapolated into silicon detectors to find the associated silicon hits.

4.2 Vertex

A position of a pp interaction, called vertex, is reconstructed using tracks. Especially, the hardest vertex, which has the highest sum of squared momenta of associated tracks in all vertices, is called primary vertex. The vertex reconstruction [70–72] consists of seeding and fitting. A vertex seed is selected as the mode of z coordinate of the reconstructed tracks. Then, the vertex position is determined by an adaptive vertex fitting algorithm with an annealing procedure [73]. After iterative fitting with the vertex compatibility, the incompatible tracks with the vertex are removed. Until all tracks are assigned to any vertices, the procedure is repeated.

4.3 Jet

After a quark or a gluon is produced, it hadronises and is observed as a group of hadronic particles, which is called jet. Jets are reconstructed mainly from the calorimeter information.

First, the cells in the calorimeter are merged using the topological clustering algorithm [74], where the used cells are required to have significant energies above a noise threshold. Second, jets are reconstructed using the anti-k_T algorithms [75] with radius parameter $R = 0.4$ as implemented in the FastJet package [76]. Jets are reconstructed as the electromagnetic scale. In order to match the jet energy to the truth-level scale, jets are calibrated [77] with pileup mitigation [78].

4.4 Electron and photon

First, a cluster of calorimeter cells is formed by the topological clustering algorithms as described in [74] as well as a jet case. Then tracks associated to the cluster are searched for. If associated tracks which come from an interaction point is found, the cluster is identified as an electron. The detail of cluster-track matching in electron reconstruction is given in Ref. [79]. Tracks associated with electrons are re-fitted using Gaussian Sum Filter [80] that treats the bremsstrahlung more appropriately. Then the supercluster algorithm [81] is performed to merge the neighbourhood clusters in order to

catch the radiated bremsstrahlung photons. If there are no associated tracks, the cluster is identified as an unconverted photon. And if there are associated tracks identified as coming from a photon conversion, the cluster is identified as a converted photon. The detail of photons reconstruction is given in Ref. [82, 83]. In this analysis, photons are used only in the $E_{\mathrm{T}}^{\mathrm{miss}}$ calculation. Electron and photon energy calibration is described in Ref. [84].

Reconstructed electrons contain the fake electron which does not come from the true electron. To reject such fake electrons, four identification criteria (VeryLoose, Loose, Medium and Tight) are defined, where electrons in a later criterion must pass an earlier criterion, and the earlier former criterion has higher efficiency and lower fake reduction. Using likelihood techniques based on the several variables, true electrons are discriminated from fake electrons as described in Ref. [85]. This analysis uses electrons labelled as "Loose" unless otherwise noted because electrons are required to be tightly vetoed. The electron and photon identification efficiencies are summarised in Ref. [86] and Ref. [83], respectively.

4.5 Muon

A muon is reconstructed using an inner-detector track (ID-track) and a muon-spectrometer track (MS-track). An MS-track is reconstructed at each sub-detector as a segment. Then, extending the segments, the track-candidate is created.

A muon is reconstructed based on various algorithms. Four muon types are defined as follows. (1) Combined muons are formed using hits from both the ID-tracks and MS-tracks. (2) Segment-tagged muons are formed using ID-tracks and muon segment in the MDT or CSC chambers. (3) Calorimeter-tagged muons are formed using ID-tracks and an energy deposit in the calorimeter compatible with the muons. (4) Extrapolated muons are formed using only MS-tracks. This analysis uses only Combined muons. Muon reconstruction performance in Run 2 is summarised in Ref. [87].

As well as electrons, to reduce fake muons, muon-identification criteria (Ref. [87]) are applied. There are three identification criteria (Loose, Medium and Tight) as with electron identification criteria. These qualities are defined based on the muon types, q/p significance, momentum balance between ID-tracks and MS-tracks, χ^2/ndf in the fit and the number of hits in muon spectrometer. This analysis uses "Medium" quality unless otherwise noted.

4.6 Missing transverse momentum

Missing transverse momentum ($E_{\mathrm{T}}^{\mathrm{miss}}$) is a sum of the momenta of undetectable particles. The SM particles observed as $E_{\mathrm{T}}^{\mathrm{miss}}$ are only neutrinos. On the other hand, some new BSM particles create $E_{\mathrm{T}}^{\mathrm{miss}}$, e.g. neutralino, so $E_{\mathrm{T}}^{\mathrm{miss}}$ has good separation power between the SM and the BSM.

$E_{\mathrm{T}}^{\mathrm{miss}}$ is reconstructed using all objects described above (hard objects) and the other

contribution (soft objects) [88, 89] as follow

$$\overrightarrow{E_T} = -\sum_{\text{jets}} \overrightarrow{p_T^{\text{jet}}} - \sum_{\text{electrons}} \overrightarrow{p_T^{\text{e}}} - \sum_{\text{muons}} \overrightarrow{p_T^{\mu}} - \sum_{\text{photons}} \overrightarrow{p_T^{\gamma}} - \overrightarrow{E_T^{\text{soft}}}, \tag{4.1}$$

where overlaps between different objects are resolved by the appropriate treatments for each objects in order to avoid the double-counting the same momentum (e.g. electron and jets).

The soft term is aiming for the low p_{T} particle contribution. The soft term is calculated using inner-detector tracks which are not associated with the hard objects as follows

$$\overrightarrow{E_T^{\text{soft}}} = \sum_{\text{tracks}} \overrightarrow{p_T^{\text{track}}}, \tag{4.2}$$

where tracks are required to have a good quality and comes from the primary vertex in order to reject fake-tracks and pileup tracks. These requirements make the soft term pileup-tolerant.

Chapter 5

Track-reconstruction for disappearing signature

The standard ATLAS tracking algorithm is designed to reconstruct trajectories of stable charged particles. The track reconstruction is the most time-consuming part of the reconstruction-algorithm chain. The fewer requirements on the number of Pixel hits in the track reconstruction increase the number of unphysical tracks, which results in a higher demand for compute resources. Moreover, the typical charged particles measured in the ATLAS detector have long lifetimes enough to fly through the inner detector. Therefore, the standard track-reconstruction algorithm requires a long trajectory and is not suitable for the particles targeted in this search due to the quite low track-reconstruction efficiency. The new special track reconstruction, which is called "Pixel tracklet" reconstruction, is designed to be enabled to reconstruct meta-stable charginos with lifetimes considered in this search. Hereafter, a track reconstructed by the pixel tracklet reconstruction is called a "pixel tracklet" or just "tracklet", and a track reconstructed by the standard track-reconstruction algorithms described in Sec. 4.1 is called a "standard track".

5.1 Algorithm

The algorithms of the pixel tracklets are based on the standard tracking described in Sec. 4.1. The main differences between the standard track reconstruction and the pixel tracklet reconstruction are the parameters and the type of used hits in the track reconstruction. A summary of the differences in the configuration between two track reconstructions is shown in Table 5.1, where "hole"-hit is defined as a missing expected hit on the trajectory, and "shared"-hit is defined as a hit which is also used by other tracks. The number of required hits in the pixel tracklet reconstruction is only four, and this is a much looser requirement than the standard track reconstruction which requires seven hits. As mentioned above, a track-reconstruction with the small number of hits leads many combinatorial-fake tracks, resulting in an enormous consumption of compute resources. In order to reduce fake tracks and the number of patterns for seed tracks,

tight requirements, which are no hole hits, no shared hits and higher p_{T}, are required at seed-track finding algorithms. This requirement keeps the compute resources at a level of less than a few percent of the standard track reconstruction.

In order to reduce the compute time, the special tracking algorithm uses only left-over hits which are not used in the standard tracks. This limitation can realise an efficient reduction of seed-tracks and remove an overlapping with tracks reconstructed in the standard tracking.

Figure 5.1 shows a distribution of the number of Pixel and SCT hits associated with a standard track or a pixel tracklet. The pixel tracklet tracking algorithm recovers short tracks having less than seven silicon hits. A peak around seven hits is due to fake tracks. The standard track reconstruction requires at least seven hits, and this is tighter than pixel tracklet tracking. However, since requirements on the hit quality are looser than pixel tracklets, fake tracks can pass the quality check.

Tracking variables	Standard tracks	Pixel tracklet
Transverse momentum	≥ 500 MeV	≥ 5 GeV
N of hits	≥ 7	≥ 4
N of holes	≤ 2	$= 0$
N of shared hits	≤ 1	$= 0$
$\lvert\eta\rvert$	≤ 2.7	≤ 2.2
Seeding	Pixel + SCT	unassociated Pixel hits

Table 5.1: A summary of tracking configuration for the standard track reconstruction and the pixel tracklet reconstruction.

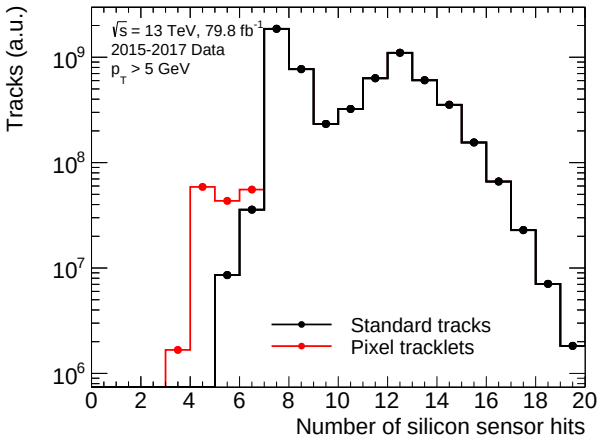

Figure 5.1: The number of hits in silicon sensors. A black line shows the standard tracks, and a red line shows pixel tracklets.

5.2 Performance

The tracking performance has to be carefully checked because pixel tracklets are strongly affected by unexpected detector conditions. This section describes the performance of the tracklet reconstruction as follows.

1. A performance for chargino samples is performed in Sec. 5.2.1 to check the signal acceptance by this tracking.

2. Tracklet selection criteria are examined in Sec. 5.2.2, that reduce fake tracks and populate tracklets originating from a particular kind of particles.

3. A tracklet performance in the observed data is performed in Sec. 5.2.3, where tracklets are produced with a special configuration to enhance high purity tracklets.

4. Additional tracklet modellings are performed using observed data in Sec. 5.2.4.

5.2.1 For meta-stable charginos

As signal samples, wino and higgsino simulated samples are used. All chargino samples are combined regardless of their masses and lifetimes to reduce statistical uncertainties. In order to ensure that a reconstructed track is produced using the hits by a chargino, it is required the chargino track association, which is defined that the Δ R between a tracklet and a generator-level particle is smaller than 0.01.

The tracklet reconstruction efficiency as a function of the decay radius vs η and z are shown in Fig. 5.2 (a) and (b), respectively. Most tracklets come from the charginos decaying between the fourth Pixel-layers (r = 123 mm) and the second SCT-layers (r = 370 mm). A low-efficiency region above $|\eta| > 1.9$ corresponds to a gap between the barrel and the end-cap of the Pixel detector. A tracklet reconstructed using hits in end-cap layers has a different track performance, especially p_{T}, from one reconstructed using only barrel layers. Therefore, this analysis uses only tracklets with $|\eta| < 1.9$. This requirement secondarily contributes to a reduction of background because the forward region has a larger amount of material than the central region.

Figure 5.3 (a) shows a comparison of the track reconstruction efficiency as a function of decay radius between the standard tracks, pixel tracklets and pixel tracklets requiring no SCT hits (SCT veto). The standard track has little efficiency when chargino decays before the SCT detector (at 300 mm). On the other hand, the pixel tracklet has a significant reconstruction efficiency in the region. After vetoing SCT hits, the reconstruction efficiency reduces, because sometimes hits originating from a chargino decay product (pion, electron or muon) or background SCT hits are assigned to the tracklet. Since these tracks have bad tracking properties, they cannot be used in the analysis. Such tracks with the wrong combination have a pile-up dependence as shown in Fig. 5.3 (b), because high pile-up circumstance increases fake tracks in the standard tracks and the fake tracks accidentally use Pixel hits originating from a chargino, resulting in inefficiency in the pixel tracklet reconstruction. This issue is expected to be

solved by using all clusters in the reconstruction step. Since a study of a pile-up tolerant tracking needs quite much compute resources, it was not implemented in this study.

Tracking parameter distributions as the difference between tracks and associated generator-level particles are shown in Fig. 5.4. Five parameters (q/p_T, θ, ϕ, transverse impact parameter (d_0) and longitudinal impact parameter (z_0) [1]) and p_{T} at the closet points with the beam spot (perigee) are shown with three type tracks (the standard tracks, pixel tracklets and pixel tracklets with SCT veto). Resolutions of θ and z_0 of pixel tracklets are compatible with tracks in the standard track reconstruction. On the other hand, resolutions of p_{T}, d_0 and ϕ of pixel tracklets are much worse than tracks in the standard track reconstruction due to the small number of associated hits and the small track length of pixel tracklets, which are related to track curvature uncertainty. Notably, a bad resolution of q/p_T of pixel tracklets gives a large impact to the analysis because the track momentum is used for a separation between the signal and the background, and used as the final discriminant. Further study using observed data is discussed in Sec. 5.2.4. A tail in the Δ q/p_T distribution of inclusive pixel tracklets is due to tracklets with SCT hits. These tracks largely have wrong hits as mentioned in the above paragraph, that leads wrong p_{T} observation.

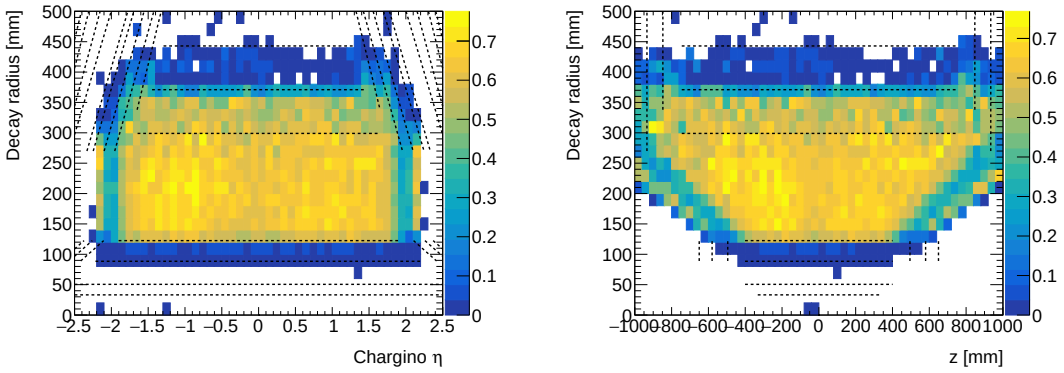

(a) (b)

Figure 5.2: Pixel tracklet reconstruction efficiency as a function of chargino decay radius vs (a) chargino η and (b) z-position of chargino decay. Black dash lines show the layer positions of the silicon detectors.

5.2.2 Disappearing tracklet selection

As mentioned in Sec. 5.1, a large fraction of pixel tracklets are fake tracks which have an unphysical origin.

[1] In this thesis, the transverse impact parameter (d_0) is defined as the distance of the closest approach in the transverse plane between a track and the beam line. The longitudinal impact parameter (z_0) is defined as the z-coordinate distance between the primary vertex and the point where the d_0 is defined.

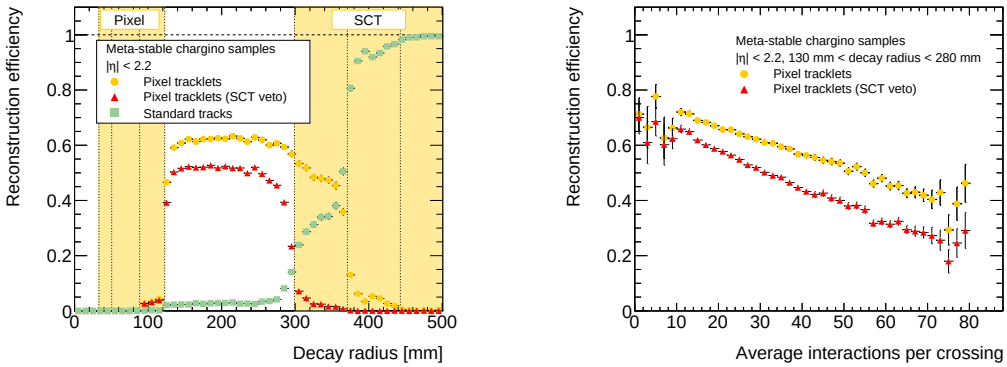

(a) (b)

Figure 5.3: (a) Track reconstruction efficiency as a function of chargino decay radius. (b) Track reconstruction efficiency when a chargino decays between the fourth Pixel-layer and the first SCT-layer as a function of average number of pp interactions per bunch crossing (pile-up). A standard track is shown as green squares. A pixel tracklet is shown as orange circles. A pixel tracklet with SCT veto is shown as red triangles. The difference between the inclusive pixel tracklet and the tracklet with SCT veto is due to wrong association of SCT hits.

Figures 5.5–5.7 show distribution of track variables of pixel tracklets after applying minimum track selections as follows

1. Kinematic selection is applied to extract signal-like kinematic topology. Details are shown in Sec. 6.3.
2. A tracklet p_{T} is required to be larger than 20 GeV
3. A tracklet $|d_0$ significance$|$ ($\equiv |d_0/\mathrm{err}(d_0)|$) is smaller than 5
4. A tracklet $|z_0 \sin\theta|$ is smaller than 500 μm,

where a tracklet which has at least one wrong associated hit is labelled as "wrong comb.". Moreover, truth matching criteria mentioned before are applied for charginos. As shown in the figures, there are many fake tracks, and a reduction of these tracks is necessary.

In this subsection, tracklet selection criteria are discussed. By applying the tracklet selection, most of fakes can be reduced, and tracklets having physical origin remain.

At least four Pixel hits

Pixel tracklet reconstruction algorithm requires that the number of clusters is more than or equal to four. However, after precise fitting, a cluster can be labelled as an outlier. An outlier hit is not used in a fitting, and then a pixel tracklet can look like a three-layer track. Such a situation happens when a particle passes through an overlap region of barrel layers because a pixel tracklet has two hits in one layer

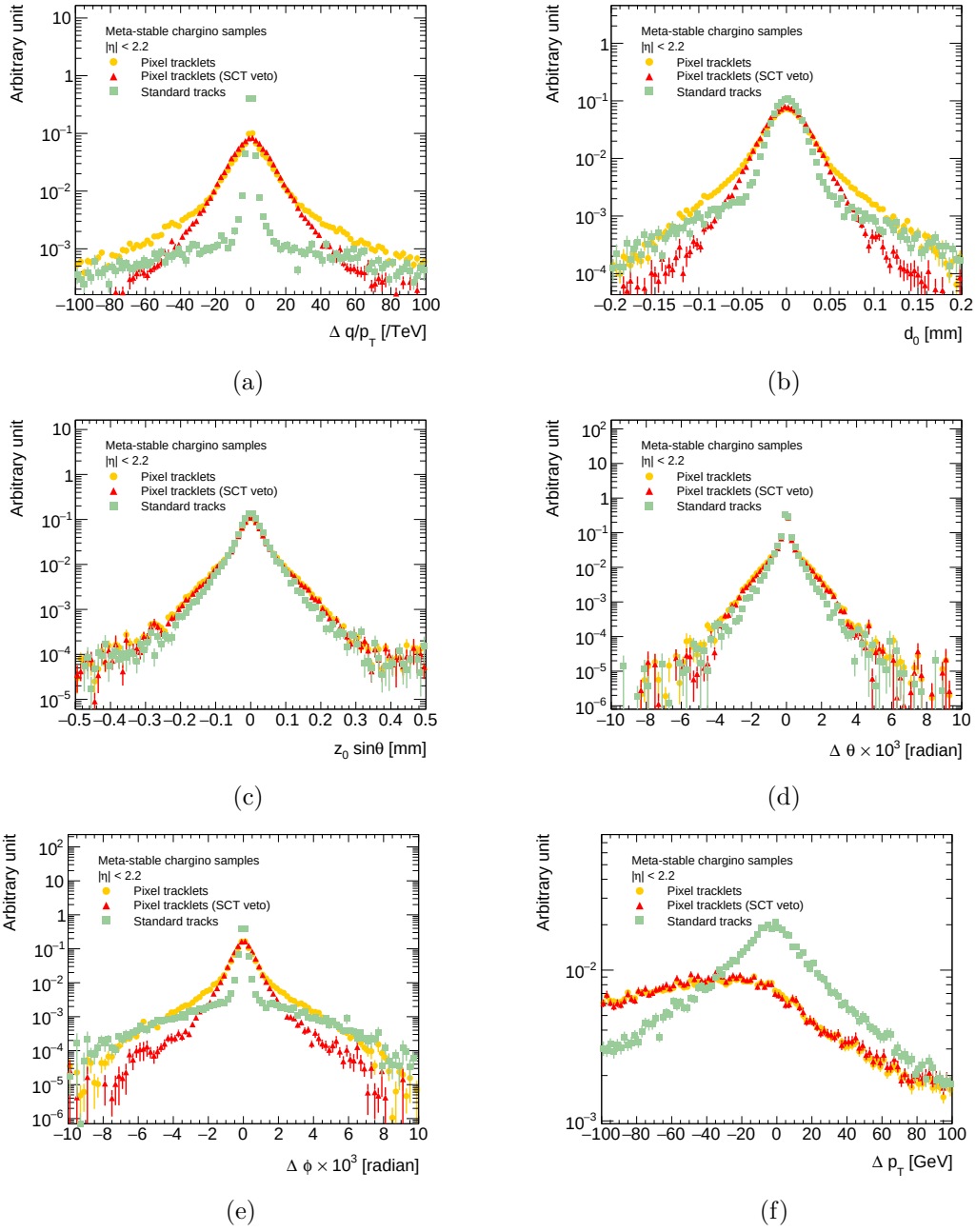

Figure 5.4: Track parameters at perigee. (a) $\Delta q/p_T$ between the track and the generator-level particle. (b) d_0. (c) $z_0 \sin\theta$. (d) $\Delta\theta$ between the track and the generator-level particle. (e) $\Delta\phi$ between the track and the generator-level particle. (f) Δp_{T} between the track and the generator-level particle. The standard tracks are shown as green squares. The pixel tracklets are shown as yellow circles. The pixel tracklets with SCT veto are shown as red triangles.

in this case. A performance of three-layer tracks is different from typical pixel tracklets (four-layer tracks). In this analysis, in order to avoid these tracks, it is required that the number of pixel layers associated with hits of the tracklet is more than or equal to four shown in Fig. 5.5 (c). This requirement ensures that a pixel tracklet has an expected track length and the performance will be under control.

All hits having good properties

There are three bad hit types labelled in the track reconstruction stage as defined in Table 5.2. In order to reduce fake background further, a tracklet is removed when it has any bad hits: fake ganged-hits (Fig. 5.5 (e)), spoilt hits (Fig. 5.5 (f)) and outlier hits (Fig. 5.5 (d)).

Label	Definition
Outlier hit	Far from the track (χ^2 >9)
Spoilt hit	Having a large position uncertainty
Fake ganged-hit	Ganged-pixels (Sec. 2.2.2) identified as fake in ambiguity solving

Table 5.2: Definitions of bad types of hits

Isolation

The rate of fake pixel tracklets is correlated to the occupancy of the Pixel detector. Jets contain many charged particles and increase the hit occupancy locally. Therefore, fake pixel tracklets are easily created around high p_{T} jets.

A chargino is isolated from other particles in most cases. Pixel tracklets are required to be isolated from other objects for a reduction of fake tracks. The isolation is evaluated using ΔR between a tracklet and other particles as follows

- minimum ΔR(tracklet, jets ($p_{\mathrm{T}} > 50$ GeV)) > 0.4 (Fig. 5.6 (a))
- minimum ΔR(tracklet, electrons) > 0.4
- minimum ΔR(tracklet, muons) > 0.4
- minimum ΔR(tracklet, muon spectrometer tracks) > 0.4 (Fig. 5.6 (b))

Additionally, in order to further reduce fake pixel tracklet from jets, a track isolation is required as $p_T^{\mathrm{cone40}} < 0.04\ p_{\mathrm{T}}$, where p_T^{cone40} is defined as a scalar sum of track p_{T} with $\Delta R(\mathrm{tracklet}, \mathrm{standard\ tracks}) < 0.4$, where used standard tracks are required to have p_{T} higher than 1 GeV and $|z_0 \sin\theta|$ less than 3 mm (Fig. 5.6 (c)).

Impact parameter

All particles except secondary particles from meta-stable particles have small impact parameter. On the other hand, fake tracks usually have large impact parameters because fake tracks have no origin particles produced around a primary vertex. This analysis requires that two variables related to the impact parameter are small.

- An absolute value of a significance of transverse impact parameter (d_0 significance $= d_0/\sigma_{d_0}$) is less than 1.5 (Fig. 5.6 (d)).
- An absolute value of longitudinal impact parameter ($z_0 \sin\theta$) is less than 0.5 mm (Fig. 5.6 (e)).

Fit quality

Fitting quality is a useful index for detecting fake tracklets. Here χ^2-probability, defined as an upper integration of the χ^2 distribution, is used. The tracklets whose χ^2-probability is less than 0.1 are rejected (Fig. 5.6 (f)).

Geometrical acceptance

Pixel tracklets are reconstructed with a range between η = -2.2 and η = 2.2. Outer region over 1.9 in $|\eta|$ is not an active region of TRT. Additionally, there is a transition region of pixel barrel and end cap shown in Fig. 5.2 and the material budget is higher. The muon spectrometer has low efficiency in the inner region ($|\eta| < 0.1$). The use of tracks in the small $|\eta|$ region leads an increase of pixel tracklet background from muons. By the above condition, it is required that the absolute η of pixel tracklets is larger than 0.1 and less than 1.9 (Fig. 5.7 (a)).

Disappearance condition

In order to ensure a pixel tracklet disappears in the tracker, it is required that the pixel tracklet has no SCT hits (Fig. 5.7 (b)) and no TRT hits (Fig. 5.7 (c)).

5.2.3 Data/MC comparison using high purity tracklets

In Sec. 5.2.2, data/MC comparisons of fake-dominant tracklets are performed to ensure that track selections efficiently reduce fake tracks. The data/MC comparisons are performed for high purity tracklets, which contain less fake tracks. It is necessary to check the validity of MC simulated samples using not-fake-like tracks. It is difficult to populate tracklet samples, in data, originating from a particle decaying to un-reconstructable particles, like charginos. This issue is solved by using an artificial re-tracking technique. The artificial pixel tracklet is created by using only hits in the pixel detector, no matter whether there are hits in the SCT or TRT detector. By doing this, all tracks, including the standard tracks, are reconstructed as pixel tracklets. Reconstructed tracklets by this method implicitly requires that there are at least four Pixel-hits. Therefore, the case that a hit associated with signal particles is missing cannot be included in this way. Such a case is assessed in Sec. 5.2.4.

Muons are good candidates to compare the track performance because it is easy to extract high purity muon track samples. Since artificial re-tracking technique requires a large number of compute resources, a limited number of data samples are used for this study, where the samples are selected to cover the whole run time in 2015–2017.

Here high purity muon tracks from $Z \to \mu\mu$ events are triggered by the single isolated muon trigger, then extracted by requiring two muons whose reconstructed mass ($M_{\mu\mu}$) of within the range of 10 GeV of the Z boson mass, where the leading muon p_{T} is larger

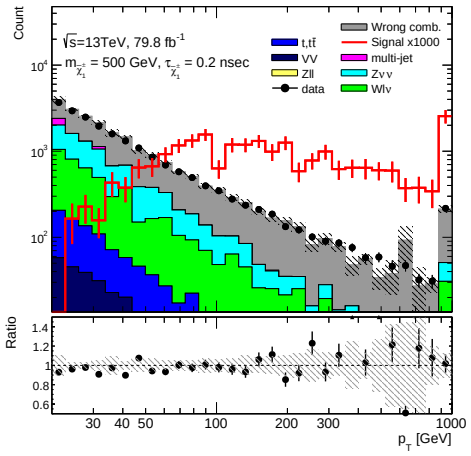

(a)

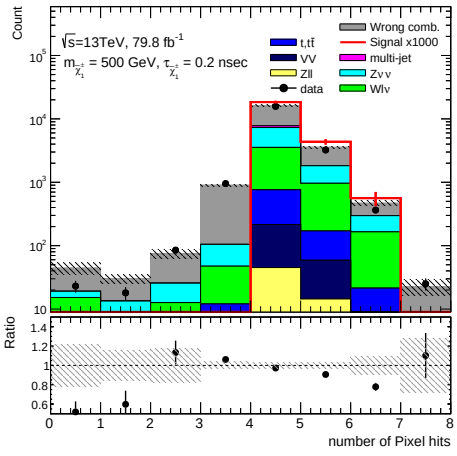

(b)

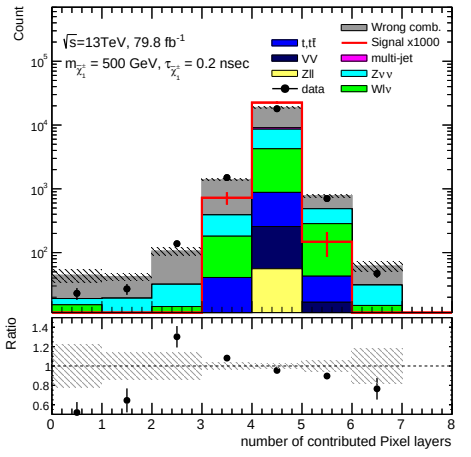

(c)

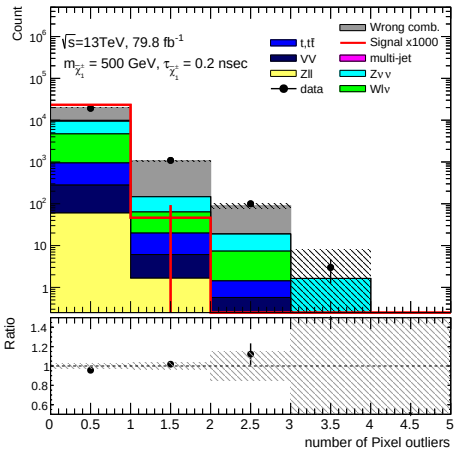

(d)

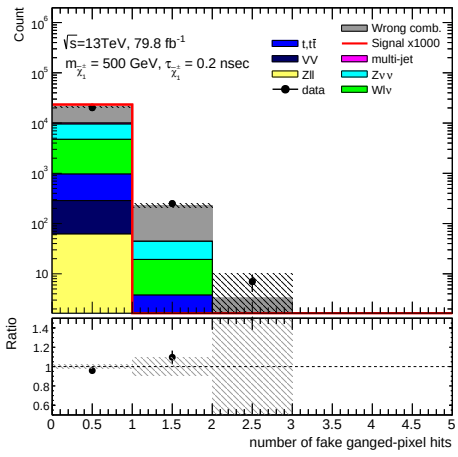

(e)

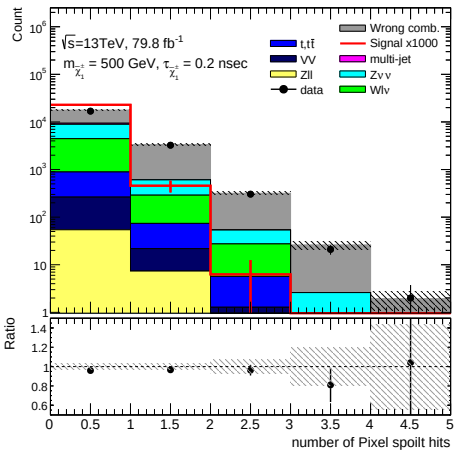

(f)

Figure 5.5: Data/MC comparison for pixel tracklets. (a) p_{T} (b) the number of Pixel hits (c) the number of Pixel layers associated with the hits (d) the number of Pixel outlier hits (e) the number of fake ganged-pixel hits (f) the number of Pixel spoilt hits

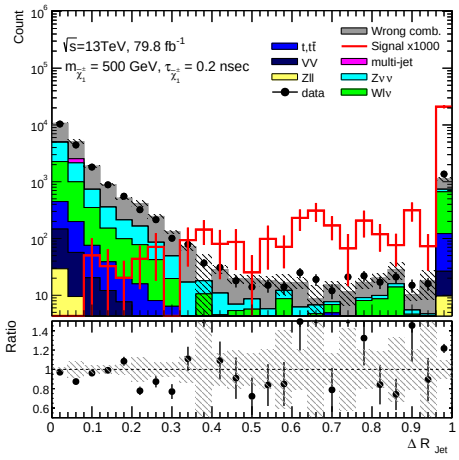

(a)

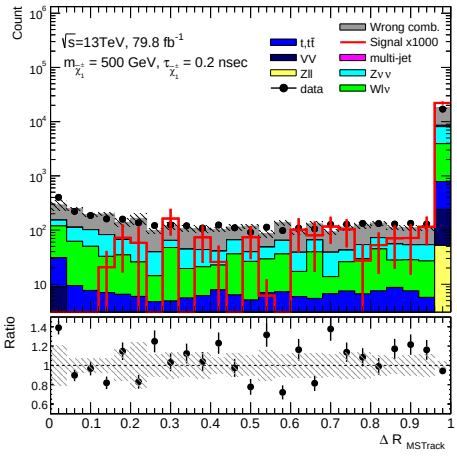

(b)

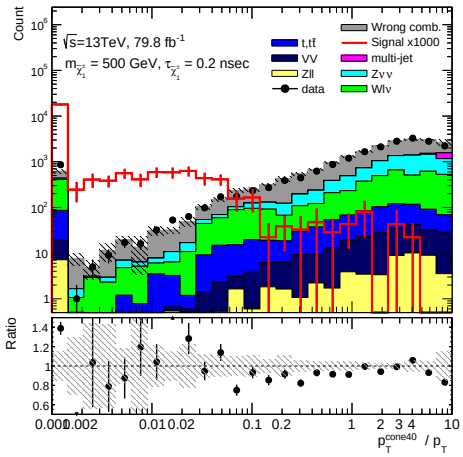

(c)

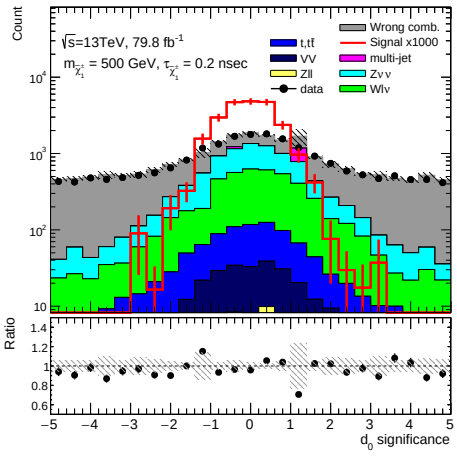

(d)

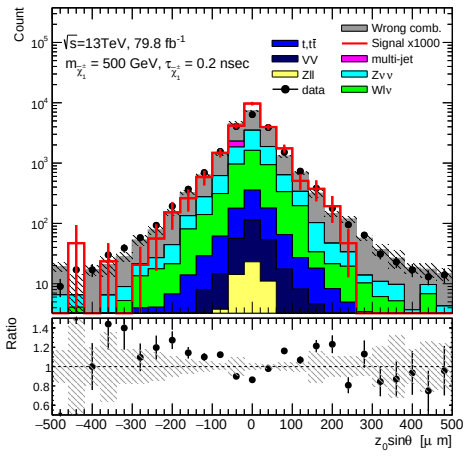

(e)

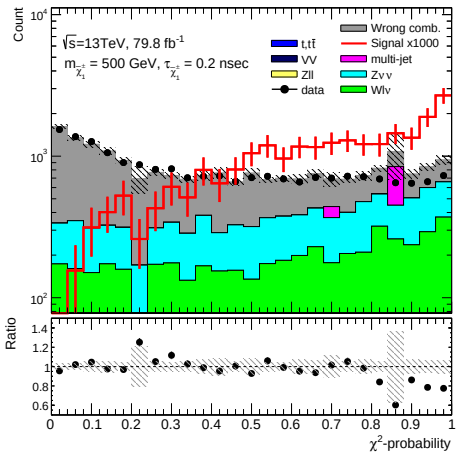

(f)

Figure 5.6: Data/MC comparison for pixel tracklets. (a) ΔR(tracklet, jets) (b) ΔR(tracklet, muon spectrometer tracks) (c) $p_T^{\text{cone40}}/\ p_{\text{T}}$ (d) d_0 significance (e) $z_0 \sin\theta$ wrt primary vertex (f) χ^2-probability

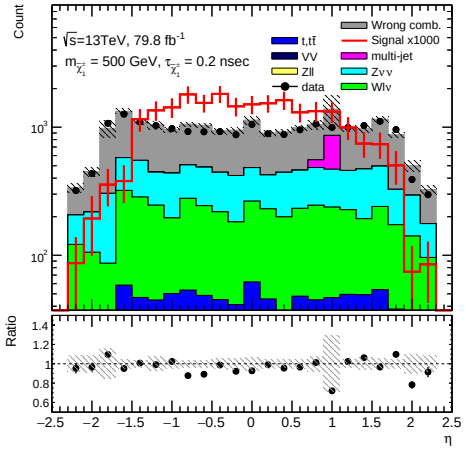

(a)

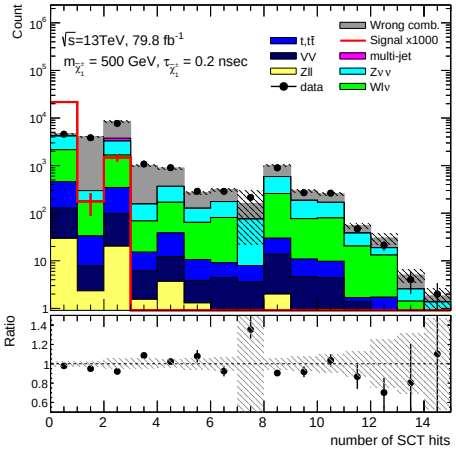

(b)

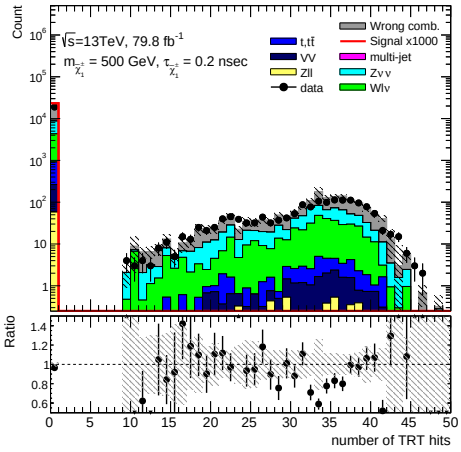

(c)

Figure 5.7: Data/MC comparison for pixel tracklets. (a) η (b) the number of SCT hits (c) the number of TRT hits

than 25 GeV and the sub-leading muon $p_{\mathrm{T}} > 20$ GeV. Additionally, in order to increase a purity, the events are required to not have electrons and that an artificial pixel tracklet overlaps with the muon track coming from the standard tracking (ΔR(tracklet, muon) < 0.2)

Figures 5.8 and 5.9 are comparison plots where disappearing track selections are applied except the related selection with its variable. As shown in these figures, the tracklet performance of MC samples is well-modelled. Since the difference in p_{T} resolution and impact parameters are sensitive in this analysis, additional treatments are applied. Systematic uncertainties related to track selection efficiency is discussed in Sec. 9.

5.2.4 Correction of simulated data using observed data

Due to a mismodelling in simulated data, a correction for a mismodelling in a simulation is necessary. This subsection describes a mismodelling in q/p_T and the number of Pixel hits.

p_{T} resolution of pixel tracklets

The modelling of p_{T} and its control are important because this analysis use tracklet p_{T} as the final discriminant and pixel tracklets are strongly affected by the detector condition and misalignment due to the small number of associated hits.

The p_{T} is calculated from the curvature of the tracks, and the curvature resolution is approximately proportional to the resolution of a sagitta, which is a maximum distance between the track and a straight line connecting the edges of the track. Sagitta resolution is approximately proportional to the inverse of the p_{T} as follows

$$\text{sagitta[m]} \sim \frac{0.3}{8} \frac{B[\mathrm{T}](L[\mathrm{m}])^2}{p_{\mathrm{T}}[\mathrm{GeV}]}, \tag{5.1}$$

where L is a track length and B is a magnetic field strength (2 T for ATLAS solenoid). The position resolution of each space points is correlated with a charge over p_{T} resolution. Therefore in order to control p_{T}, a q/p_T resolution is measured from observed data then the generator-level p_{T} in simulated samples is smeared using the resolution function instead of directly using the reconstructed p_{T} of simulation samples. The measured q/p_T resolution is called "smearing function" because it is used to smear the generator-level p_{T}.

The measurements of $\Delta q/p_T$ between a tracklet and an associated standard track is performed with both data and MC samples for the different p_{T} slices. The artificial re-tracking technique discussed in the Sec. 5.2.3 is applied for both samples. The artificial re-tracking technique requires the existence of the standard tracks, resulting in a potential bias from a missing event where a charged particle is not reconstructed as the standard tracks. However, the effect is negligible ($< 5 \times 10^{-3}$) because the probability of such events is small (<1%) and, moreover, the behaviour of p_{T} resolution of such event is equivalent to the one of events having the standard tracks in most cases (>95%).

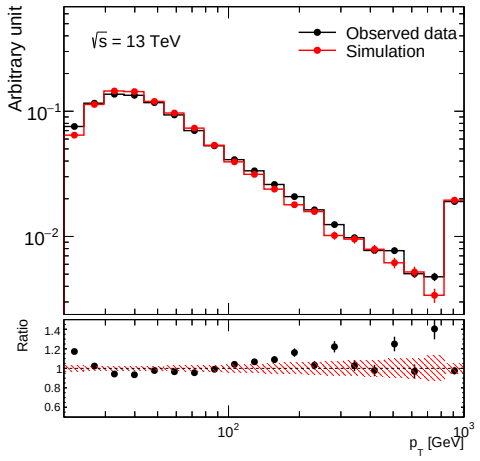

(a)

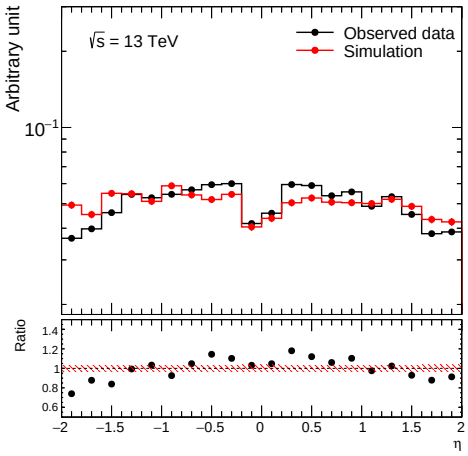

(b)

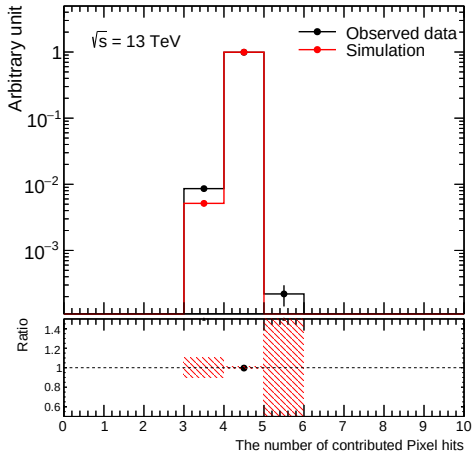

(c)

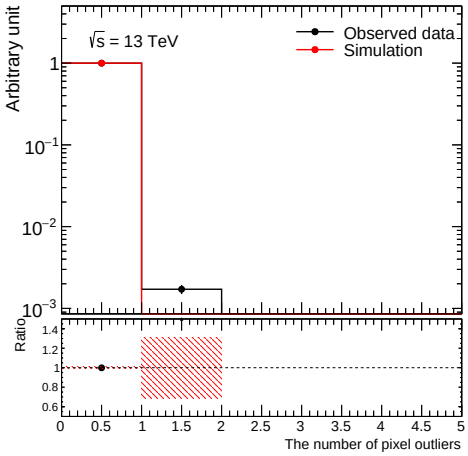

(d)

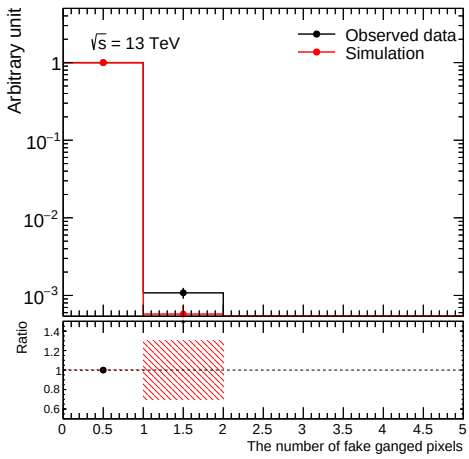

(e)

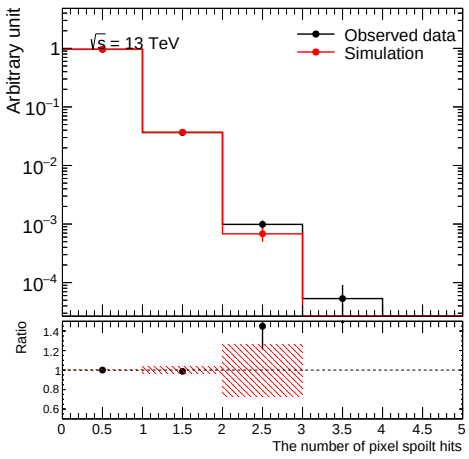

(f)

Figure 5.8: Data/MC comparison with muon tracks. Disappearing track selections are applied except the related selection with its variable. (a) p_{T} (b) η (c) The number of Pixel-layers associated with the hits (d) The number of Pixel outlier hits (e) The number of fake ganged-pixel hits (f) The number of Pixel spoilt hits

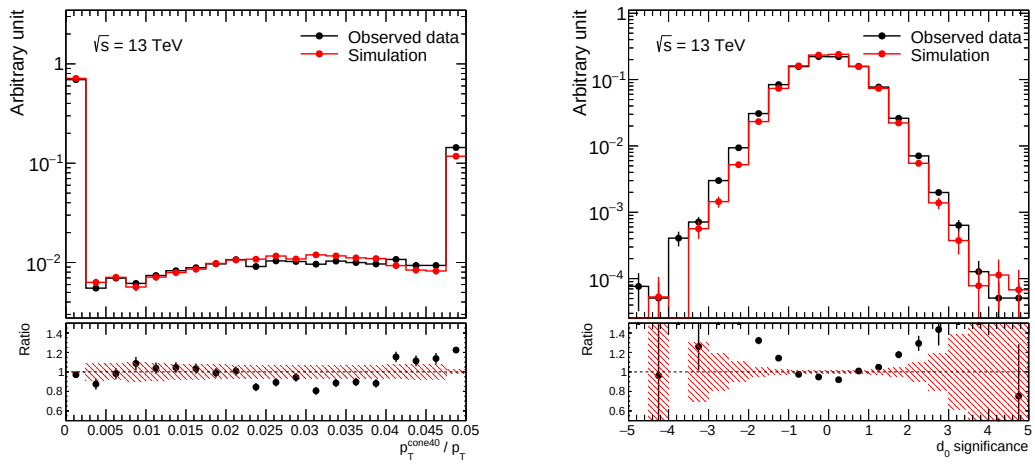

(a)

(b)

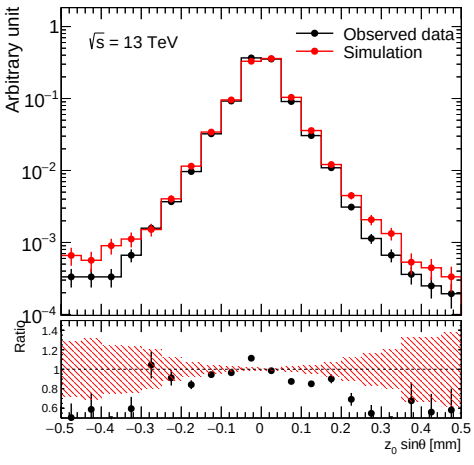

(c)

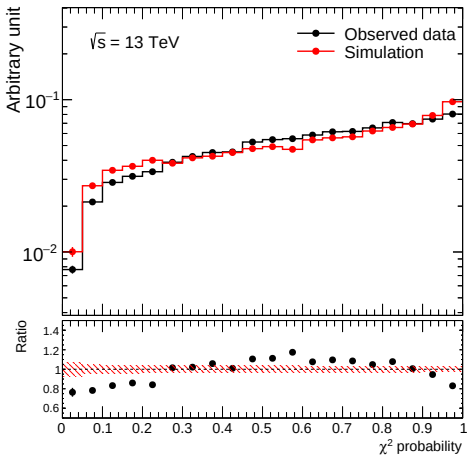

(d)

Figure 5.9: Data/MC comparison with muon tracks. Disappearing track selections are applied except the related selection with its variable. (a) $p_T^{\text{cone40}}/\ p_{\text{T}}$ (b) d_0 significance (c) $z_0 \sin\theta$ wrt primary vertex (d) χ^2-probability

The event missing the standard tracks is caused by a scatter with material because the SCT detector and the TRT detector cover the full η range of the pixel tracklet ($0.1 < |\eta| < 1.9$) as shown in Fig. 2.2. In such events, 95% of particles, which are reconstructed as pixel tracklet but fail to reconstruct the standard track, are derived from being scattered by material between the fourth Pixel-layer and the first SCT-layer as shown in Fig. 5.10. Since the scatter occurs after creating four Pixel hits used in a pixel tracklet, their positions are not affected by the scatter. Because of using the unbiased four Pixel hits, p_{T} resolution is equivalent to the measurements based on the artificial re-tracking technique. Therefore, the smearing function is well-modelling a p_{T} resolution of the pixel tracklet.

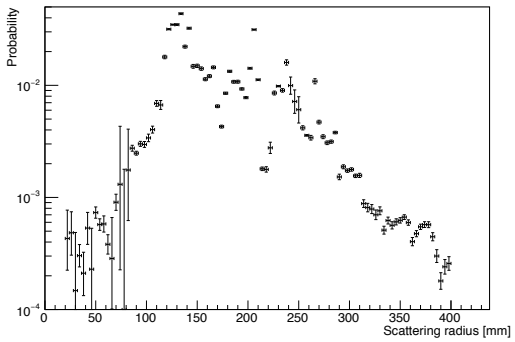

Figure 5.10: The probability of identifying an electron as a disappearing pixel tracklet as a function of the scattering radius. The fourth Pixel-layers and the first SCT-layers are placed at z-positions of 123 mm and 299 mm, respectively. Since each layer is not an ideal cylindrical but tilted, a part of sensors is widely placed around the designed positions.

In order to extract high purity lepton tracks from data samples, $Z \to ee$ and $Z \to \mu\mu$ events are selected by applying similar selection to the selection in Sec. 5.2.3. Additionally, the disappearing track selection except for lepton veto and the p_{T} requirements is applied to extract tracklets with the same conditions as the analysis. For MC samples, special simulated samples, where only one particle is produced in the interaction point with no pileup, are used to obtain the high purity tracks.

The $\Delta\ q/p_T$ distribution with a fit for high p_{T} particles are shown in Fig. 5.11 for the $Z \to ee$ and $Z \to \mu\mu$ comparison in the data and for the muon and pion comparison in the simulated samples. Others are shown in Appendix A. In the fit, a double-sided

Crystal-ball function is used.

$$
\begin{aligned}
f(z) &= \begin{cases} A \cdot (B - z)^{-n} & (z < -\alpha), \\ \exp\left(-z^2/2\right) & (-\alpha < z < \alpha), \\ A \cdot (B + z)^{-n} & (z > \alpha) \end{cases} \\
z &= \frac{\Delta(q/p_T) - \beta}{\sigma} \\
A &= \left(\frac{n}{\alpha}\right)^n \exp\left(-\frac{\alpha^2}{2}\right) \\
B &= \frac{n}{\alpha} - \alpha,
\end{aligned}
\tag{5.2}
$$

where α, β, σ and n are parameters representing the slope of the tail part, the mean of the core part, the resolution of the core part and the index of the tail power function, respectively. After the fit, the best fit n is very large sometimes. When n is infinity, a tail part of this function becomes exponential as follows

$$
\begin{aligned}
f(z) &= \begin{cases} \exp(\alpha(z + \alpha/2)) & (z < -\alpha) \\ \exp(-z^2/2) & (-\alpha < z < \alpha), \\ \exp(-\alpha(z - \alpha/2)) & (z > \alpha) \end{cases} \\
z &= \frac{\Delta(q/p_T) - \beta}{\sigma}.
\end{aligned}
\tag{5.3}
$$

In case that n is consistent with infinity, Eq. 5.3 is used instead.

Fig. 5.12 shows the p_{T} dependence of the fitting parameters of the smearing functions. Basically, the resolution in data is worse than that in MC. This is expected due to the misalignment. Electrons with low momenta are more strongly affected multiple-scattering effects than other heavier particles. The muons and pions have similar properties because their masses are similar. But pions have a wider tail in the high p_{T} region as shown in Fig. 5.12 (c). These effects are taken into account in the analysis.

Summarised above, the $\Delta q/p_T$ distribution measured from observed data is used to smear the signal chargino p_{T} and to estimate tracklet p_{T} from the standard track p_{T} distributions in observed data. For muons and electrons, the distributions measured in $Z \to ee$ events and $Z \to \mu\mu$ events are applied respectively. For hadrons and charginos, the distribution measured from $Z \to \mu\mu$ events is used instead of measurements of the hadrons and charginos in observed data. The additional tail effect (n) which is observed in simulation is added to the distribution for hadron and electron with 100% uncertainties.

Effects from Pixel dead modules

Some fraction of pixel sensors is not functional due to synchronisation errors or the other problems in the modules. A modelling of the status of Pixel modules is not perfect in the simulation. Since this analysis requires for tracks to have at least four Pixel hits, the

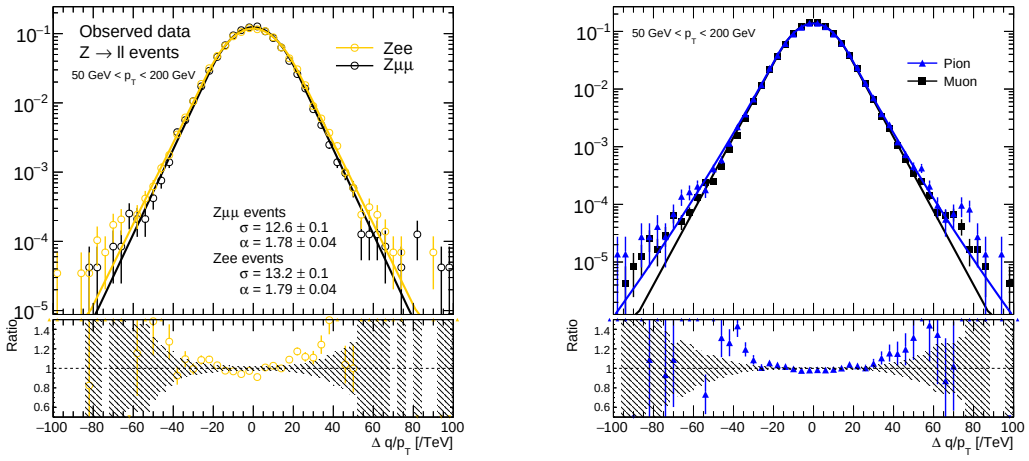

(a) (b)

Figure 5.11: $\Delta\ q/p_T$ distribution passed disappearing track selection. (a) The comparison of $Z \to ee$ and $Z \to \mu\mu$ events in observed data. (b) The comparison of muon and pion events in the simulated samples.

dead modules change the signal acceptance. Therefore this effect should be considered using observed data.

The artificial re-tracking method discussed before does not work in this case because it requires sufficient Pixel hits originating from a charged particle. In order to measure the efficiency of Pixel hits requirements, high purity muon tracks reconstructed by the standard track reconstruction is used. The high purity muons are extracted by selecting $Z \to \mu\mu$ events. Then, in order to reduce fake tracks, additional track selections are required as follows

1. $p_{\mathrm{T}} > 15$ GeV
2. The number of Pixel hits is more than one
3. The number of SCT hits is more than four
4. The number of TRT hits is more than five

The selection efficiency of a requirement on at least four contributed Pixel-layers is shown in Fig. 5.13 (a) and (b). Some effects from dead modules are not reflected MC as shown in the figures. Figure 5.13 (c) shows a ratio of data to MC which is used to scale the signal samples in the final steps in this analysis.

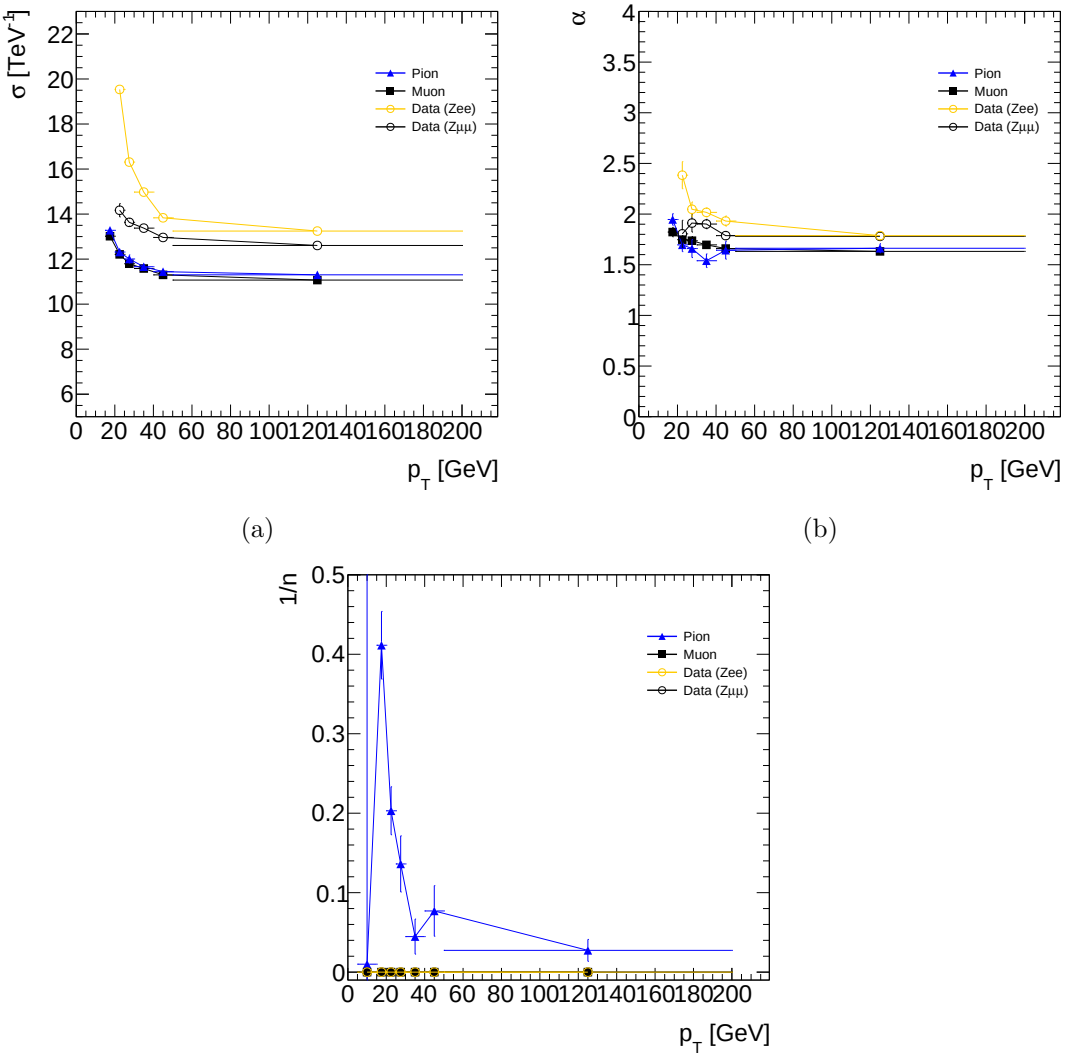

(a) (b)

(c)

Figure 5.12: Parameters of the smearing function as function of particle p_{T}. Black open circles show a $Z \to \mu\mu$ events in data. Yellow open circles show a $Z \to ee$ events in data. Black squares show a muon in simulated samples. Blue triangles show a pion in simulated samples. (a) A resolution of the core part (σ). (b) A slope of the tail part (α). (c) An additional slope of the tail part (n).

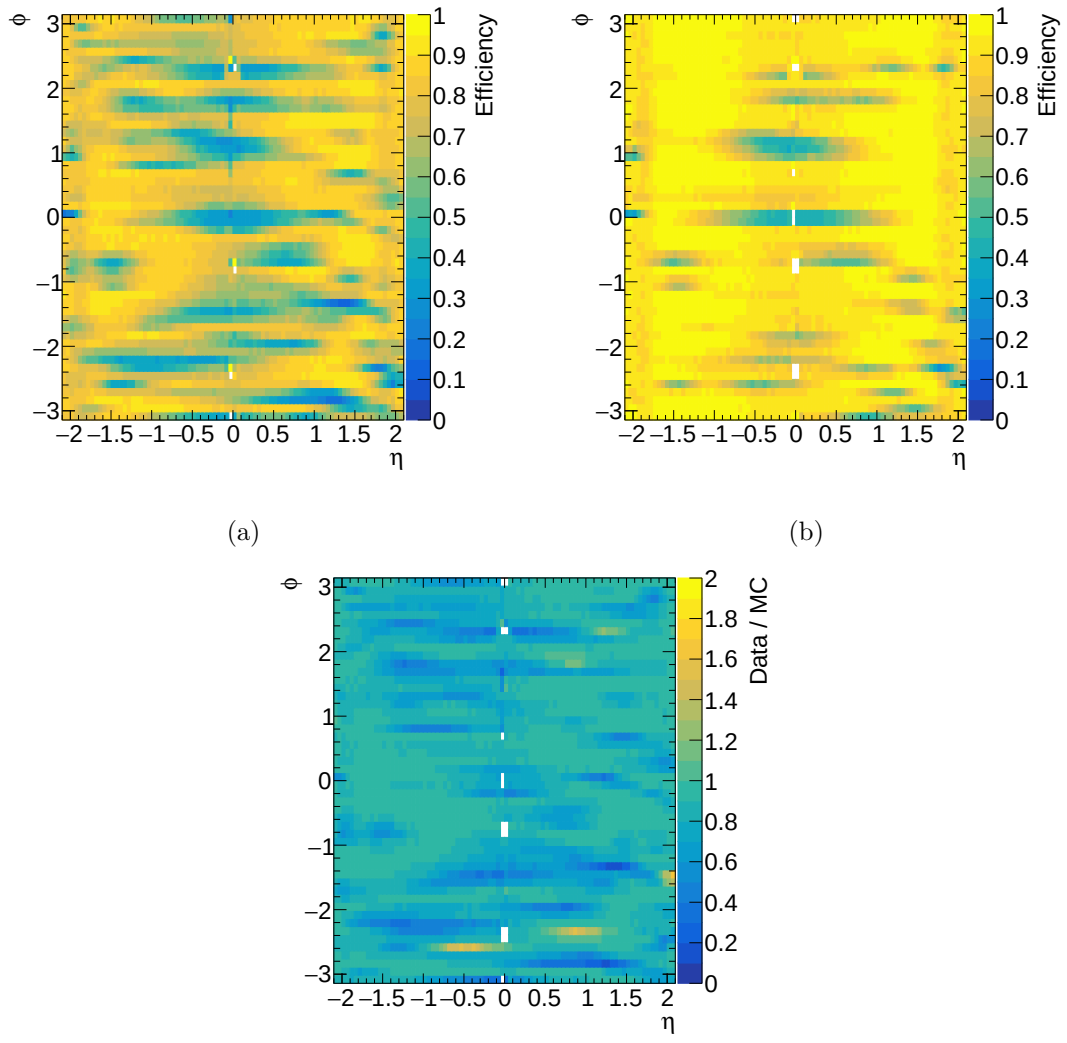

(a) (b)

(c)

Figure 5.13: Data/MC comparison with muon tracks. Selection efficiency of the number of Pixel-layers associated with the tracks. (a) Data (b) MC (c) Data/MC

Chapter 6

Event selection

There are two chargino production modes. One is the electroweak direct production of a chargino-pair or a chargino-neutralino pair. The other is a cascade decay from other heavier particles, e.g. gluino. In the latter case, the masses of heavier particles should be light enough to be produced in the LHC at 13 TeV for this search to have sensitivity. Although, some models (e.g. PGM models with some tuning parameters) predict heavier particles which are possible to be produced at the LHC energy, current limits on gluino is strict. In the former case, the production cross-section depends on only the chargino and neutralino masses. The electroweak direct production is more inclusive than the strong production. This thesis focuses on the electroweak direct production as illustrated in Fig. 6.1 (a).

When the mass difference between chargino and neutralino is quite small, it is difficult to detect the secondary particles. This analysis requires initial-state-radiation (ISR) jets as illustrated in Fig. 6.1 (b) to trigger the events. The chargino prouduction is often accompanied by ISR jets due to high-Q^2 required to produce charginos. The existence of high energy ISR jets and undetectable chargino/neutralino leads an observation of large $E_{\mathrm{T}}^{\mathrm{miss}}$ in the situation of no leptons. The large $E_{\mathrm{T}}^{\mathrm{miss}}$ signature is characteristic compared to a large momentum jet signature, and a trigger threshold of $E_{\mathrm{T}}^{\mathrm{miss}}$ is much less than a threshold of a single jet trigger. The $E_{\mathrm{T}}^{\mathrm{miss}}$ is used as a physics-object for triggering the events instead of jets.

6.1 Trigger

Events were triggered by a $E_{\mathrm{T}}^{\mathrm{miss}}$ trigger [32, 90]. Trigger thresholds and algorithms in the $E_{\mathrm{T}}^{\mathrm{miss}}$ calculation were changed depending on the instantaneous luminosity since the $E_{\mathrm{T}}^{\mathrm{miss}}$ trigger rate highly depends on the pile-up. For 2015–2016 data, the events were triggered by the $E_{\mathrm{T}}^{\mathrm{miss}}$ threshold of 50 GeV in the level-1 trigger, then they were triggered by the $E_{\mathrm{T}}^{\mathrm{miss}}$ threshold of 70–110 GeV in the high-level-trigger, where $E_{\mathrm{T}}^{\mathrm{miss}}$ in the high-level-trigger was calculated by the missing H_T (MHT) algorithm [32], where the calibrated anti-k_T jets with a radius parameter of 0.4 were used for the $E_{\mathrm{T}}^{\mathrm{miss}}$ calculation. For 2017 data, due to the serious pile-up condition, the events were triggered by the

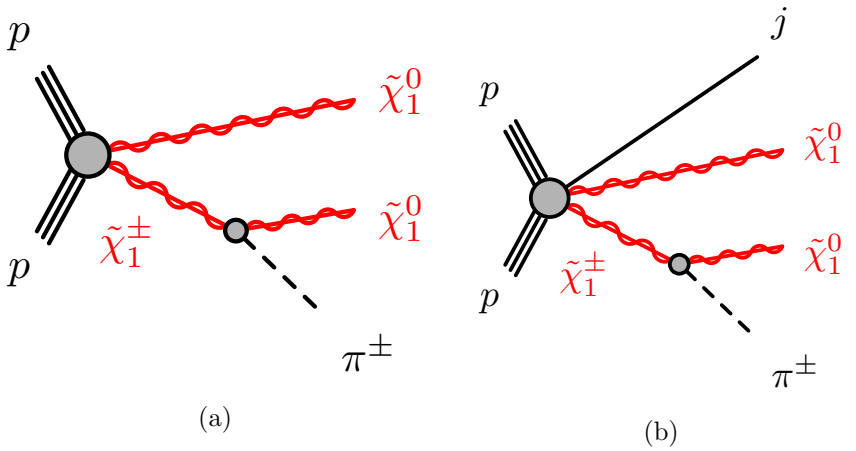

Figure 6.1: Feynman diagrams of (a) chargino-neutralino direct production (b) chargino-neutralino direct production with an association of one ISR jet.

$E_{\mathrm{T}}^{\mathrm{miss}}$ threshold of 55 GeV in level-1 trigger, then they were triggered in the high-level-trigger by the $E_{\mathrm{T}}^{\mathrm{miss}}$ threshold of 110 GeV which was calculated by the pile-up fit (pufit) algorithm [32], where topological clusters were used for the $E_{\mathrm{T}}^{\mathrm{miss}}$ calculation, and pileup were subtracted by the average of the low-p_{T} segmented calorimeter clusters in the events.

A trigger performance is not perfectly modelled in the simulation. In order to reduce the systematic uncertainties, the trigger efficiency is directly measured from observed data using $W \to \mu\nu$ events. The trigger $E_{\mathrm{T}}^{\mathrm{miss}}$ is calculated from only calorimeter energy deposits, leading that muon momentum are treated as $E_{\mathrm{T}}^{\mathrm{miss}}$. Similarly, signal charginos are treated as $E_{\mathrm{T}}^{\mathrm{miss}}$ because they do not leave their energies in the calorimeter and the muon spectrometer. Therefore, it is possible to measure the trigger efficiency in a similar topology to signals.

$W \to \mu\nu$ events are triggered by the single isolated muon, then are extracted by requiring

1. exact one muon identified as "Tight" quality and $p_{\mathrm{T}} > 27$ GeV
2. no electrons
3. 30 GeV $< m_T <$ 100 GeV, where transverse mass (m_T) is defined as

$$m_T = \sqrt{2p_T^{\mathrm{muon}} E_{\mathrm{T}}^{\mathrm{miss}} \left[1 - \cos\Delta\phi(\mathrm{muon}, E_{\mathrm{T}}^{\mathrm{miss}})\right]} \tag{6.1}$$

4. p_{T} of the highest-p_{T} jet (leading jet) > 140 GeV
5. $\Delta\phi(\mathrm{jets}, E_{\mathrm{T}}^{\mathrm{miss}}) > 1.0$, where $\Delta\phi(\mathrm{jets}, E_{\mathrm{T}}^{\mathrm{miss}})$ is defined as a minimum $\Delta\phi$ between $E_{\mathrm{T}}^{\mathrm{miss}}$ and each of the up to four highest-p_{T} jets.

The last two requirements are to match the kinematical topology with the events after a kinematic selection as discussed in Sec. 6.3. By using $W \to \mu\nu$ events extracted by this selection, a trigger efficiency is estimated as a ratio of events which passes $E_{\mathrm{T}}^{\mathrm{miss}}$ trigger to all events as a function of $E_{\mathrm{T}}^{\mathrm{miss}}$.

The observed trigger efficiency is shown in Fig. 6.2 (a) with all trigger menus used in this analysis. Due to a finite $E_{\mathrm{T}}^{\mathrm{miss}}$ resolution, the turn-on is mild, and the actual thresholds do not match exactly to the trigger names. However, most of the events with the offline $E_{\mathrm{T}}^{\mathrm{miss}} > 200$ GeV pass all the $E_{\mathrm{T}}^{\mathrm{miss}}$ triggers. Jet activities slightly affect the $E_{\mathrm{T}}^{\mathrm{miss}}$ trigger efficiency, although the $E_{\mathrm{T}}^{\mathrm{miss}}$ trigger should depend on only $E_{\mathrm{T}}^{\mathrm{miss}}$ ideally. In order to consider this effect, a two-dimensional map of $E_{\mathrm{T}}^{\mathrm{miss}}$ and leading jet p_{T} as shown in Fig. 6.2 (b) is applied to signal simulated samples.

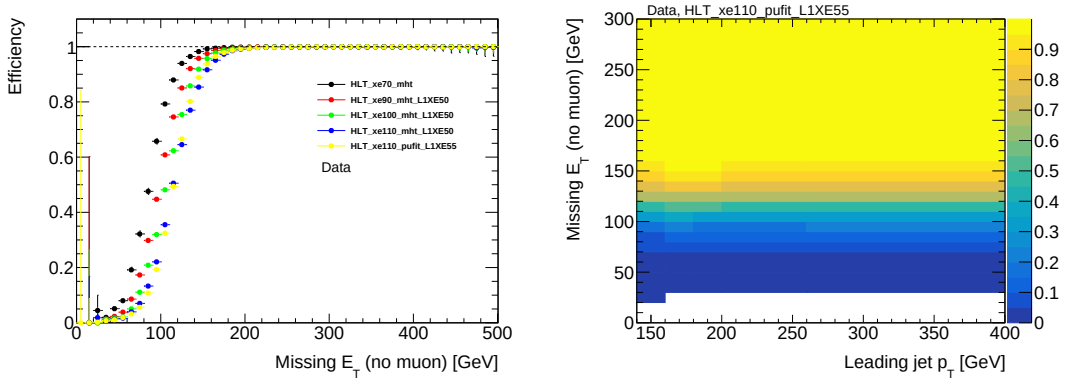

(a) (b)

Figure 6.2: $E_{\mathrm{T}}^{\mathrm{miss}}$ trigger efficiency measured from $W \to \mu\nu$ events. (a) Trigger efficiency as a function of the offline $E_{\mathrm{T}}^{\mathrm{miss}}$. Data points are coloured by $E_{\mathrm{T}}^{\mathrm{miss}}$ thresholds and trigger $E_{\mathrm{T}}^{\mathrm{miss}}$ reconstruction algorithms in the L1 and the HLT trigger. (b) $E_{\mathrm{T}}^{\mathrm{miss}}$ trigger efficiency in 2017 data as a function of a magnitude of the offline $E_{\mathrm{T}}^{\mathrm{miss}}$ and the leading jet p_{T}. A weak dependence on the jet p_{T} is observed.

6.2 Event cleaning

Events which are not triggered by a hard pp scattering are removed by the following criteria.

Non-collision background veto

Non-collision background events mainly come from beam scattering before collision point [91,92]. When a part of beams is scattered at the forward region of the beam pipe, some energetic particle can travel through the detector and leave large energy in the calorimeter without tracks from the nominal interaction point. Such an event appears to have jets and a small number of tracks.

Two cleaning criteria ("Loose" and "Tight") as described in Ref. [93] are applied to jets in this analysis. First, all jets with p_{T} higher than 20 GeV are required to pass the "Loose" jet cleaning criteria. If any jets do not pass these cleaning criteria, the event is rejected. The "Loose" cleaning rejects bad jets clearly identified as coming from non-collision background. Second, a leading jet is required to pass the "Tight" jet cleaning criteria. "Tight" criteria use precise inner-detector track information, so an η of a leading jet is required to be within the coverage of the inner tracker ($|\eta| < 2.4$). If the leading jet is not satisfied with the both requirements, the event is discarded.

An effect of this cleaning is shown in Fig. 6.3. Events from non-collision backgrounds peak around $\phi = 0$ and π are suppressed by the cleaning criteria.

Bad muon veto

A muon can have an anomalously large momentum with a large momentum error by a mis-reconstruction of a track or a mis-combination of an inner-detector track and a muon-spectrometer track. In order to reject such a muon, a muon is required that the relative curvature error ($\sigma_{q/p}/(q/p)$) is smaller than 0.2 and smaller than $\sigma_{q/p}/(q/p)$ of an inner-detector track and a muon-spectrometer track.

Additionally, in order to reduce bad events where fake muons create large $E_{\mathrm{T}}^{\mathrm{miss}}$, the following value :

$$\frac{E_{\mathrm{T}}^{\mathrm{miss,muon}}}{E_{\mathrm{T}}^{\mathrm{miss}}} \cos\left\{\phi(E_{\mathrm{T}}^{\mathrm{miss,muon}}) - \phi(E_{\mathrm{T}}^{\mathrm{miss}})\right\} \tag{6.2}$$

is required to be less than 0.5, where $E_{\mathrm{T}}^{\mathrm{miss,muon}}$ is defined as follows

$$\overrightarrow{E_{\mathrm{T}}}^{\mathrm{miss,muon}} = -\sum_{\mathrm{muons}} \overrightarrow{p_{\mathrm{T}}^{\mu}}. \tag{6.3}$$

6.3 Kinematic selection

A kinematical topology of the target signal is characterised by the high p_{T} jets, the large $E_{\mathrm{T}}^{\mathrm{miss}}$ and no leptons as shown in Fig. 6.1 (b). Kinematical selections are applied to reduce the SM processes as follows.

Lepton veto

If an event has a lepton (an electron or a muon) whose transverse momentum is higher than 10 GeV, the event is rejected. The lepton veto reduces events from $W \to \ell\nu$, $Z \to \ell\ell$ and t-quark production. Since a lepton leaves a track in the inner detector, a lepton failing identification criteria becomes one of the main backgrounds in this analysis. Properties of the background and a way of background estimation are discussed in Sec. 7.3.

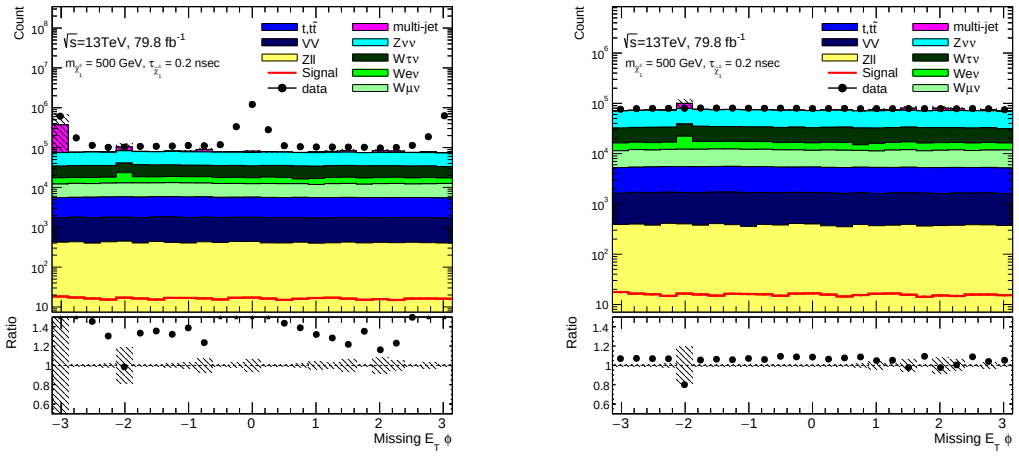

(a) (b)

Figure 6.3: $E_{\mathrm{T}}^{\mathrm{miss}}$ ϕ distribution (a) before applying the non-collision background veto (b) after applying the non-collision background veto

Energetic jet and $E_{\mathrm{T}}^{\mathrm{miss}}$

The leading jet p_{T} and the magnitude of $E_{\mathrm{T}}^{\mathrm{miss}}$ are required to be larger than 150 GeV and 200 GeV, respectively. The use of two different thresholds helps to extract signal events efficiently. Additionally, it is required that the minimum $\Delta\phi$ between $E_{\mathrm{T}}^{\mathrm{miss}}$ and each of the up to four highest-p_{T} jets with $p_{\mathrm{T}} >$ 50 GeV ($\Delta\phi(\mathrm{jets}, \mathrm{E}_{\mathrm{T}}^{\mathrm{miss}})$) is larger than 1.0. $E_{\mathrm{T}}^{\mathrm{miss}}$ produced from the SM processes not emitting neutrinos is mostly created by jet mismeasurement, resulting in a small distance between a jet and $E_{\mathrm{T}}^{\mathrm{miss}}$. Therefore, the above selection strongly reduces the SM processes not having neutrinos (multi-jets, t-quark production with no lepton).

Figure 6.4 shows distributions of kinematical variables used in the kinematic selection where the selection related to the plotting variable is not applied. The multi-jet event is not well modelled as shown in Fig. 6.4 (b). However, the multi-jet events are tightly reduced by the $E_{\mathrm{T}}^{\mathrm{miss}}$ and the minimum $\Delta\phi$ selection as shown in Fig. 6.4 (b) and (c), and do not remain after the kinematic selection.

Table 6.1 shows the cut-flow comparison between the observed data, the SM background in the simulated samples and the signal process in the simulated samples. There is a discrepancy in the amount of the observed data and simulated samples before the lepton veto because of the mismodelling of the multi-jet process. However, a reasonable agreement in the amount of observed data and simulated samples is seen after $E_{\mathrm{T}}^{\mathrm{miss}}$ selection. The number of events which pass the kinematic selection is well modelled.

$E_{\mathrm{T}}^{\mathrm{miss}}$ distribution after the kinematical selection is shown in Fig. 6.5. $E_{\mathrm{T}}^{\mathrm{miss}}$ distribution obtained from the simulated data is in good agreement with that of the observed

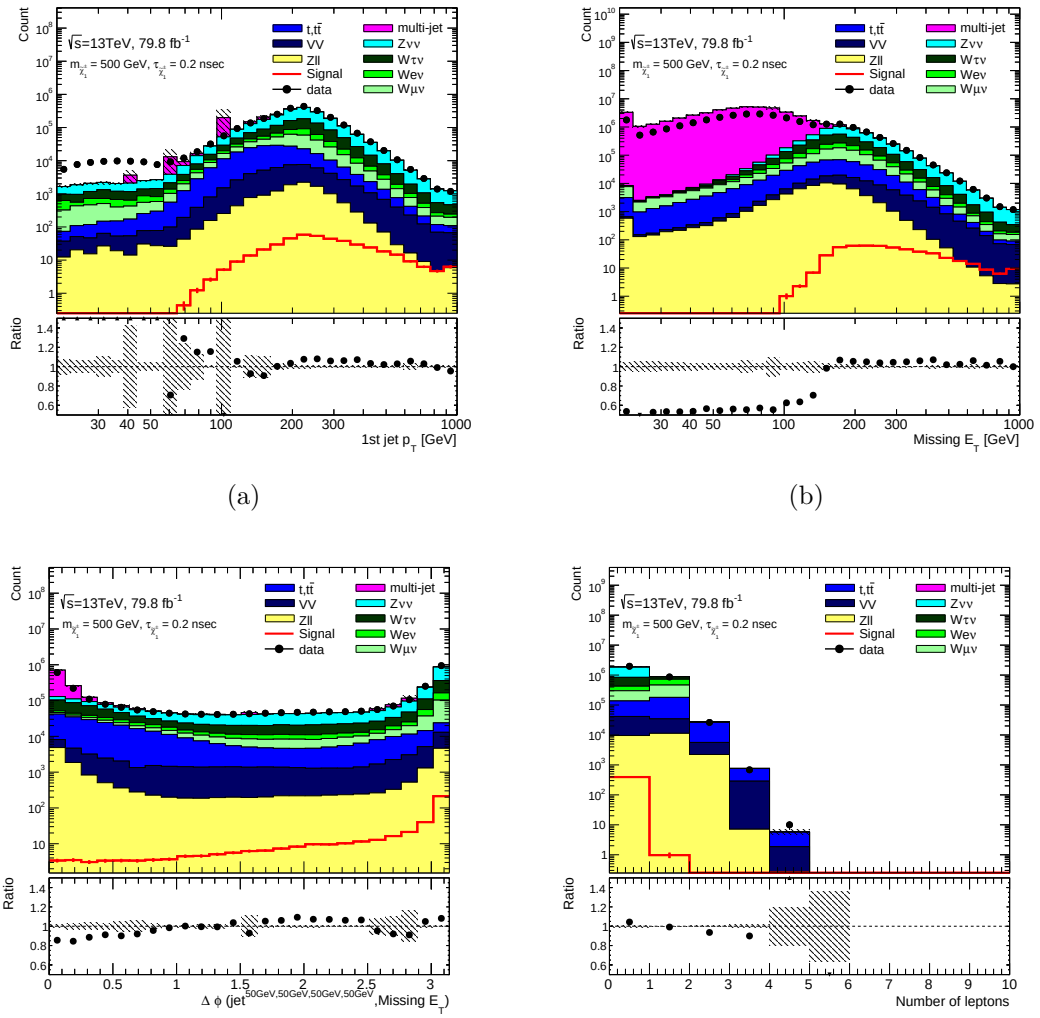

(a) (b)

(c) (d)

Figure 6.4: Kinematic distribution after all kinematic selections except for the selection related with the plotting variable. Multi-jets samples with the leading generator-level jet p_{T} smaller than 60 GeV are removed to reduce large statistical fluctuation. (a) Leading jet p_{T} (b) $E_{\mathrm{T}}^{\mathrm{miss}}$ (c) minimum $\Delta\phi$ (jets, $E_{\mathrm{T}}^{\mathrm{miss}}$) (d) The number of leptons

Requirement	Number of events		
	Observed	SM background (MC)	Signal (m=500 GeV)
Trigger	5.98×10^8	$(8.58 \pm 0.08)\times10^8$	990 ± 7
Event cleaning	4.15×10^8	$(7.18 \pm 0.07)\times10^8$	919 ± 6
Lepton veto	3.92×10^8	$(6.91 \pm 0.07)\times10^8$	917 ± 6
$E_{\mathrm{T}}^{\mathrm{miss}} > 200$ GeV	3.76×10^6	$(3.99 \pm 0.15)\times10^6$	463 ± 5
Leading jet $p_{\mathrm{T}} > 150$ GeV	3.20×10^6	$(3.30 \pm 0.03)\times10^6$	421 ± 4
$\Delta\phi_{\mathrm{min}}^{\mathrm{jet}-\mathrm{E}_{\mathrm{T}}^{\mathrm{miss}}} > 1.0$	1.97×10^6	$(1.89 \pm 0.02)\times10^6$	394 ± 4

Table 6.1: Summary of selection efficiency of the observed data, the SM background in MC simulation and signal process in MC simulation. Multi-jets samples with the leading generator-level jet p_{T} smaller than 60 GeV are removed to reduce large statistical fluctuation. Simulated samples are normalized to 79.8 fb^{-1}.

data. Table 6.2 shows the fraction of the SM background processes after the kinematic selection. The main remaining process is $Z \to \nu\nu$ and $W \to \tau\nu$ after the kinematic selection.

Processes	Kinematic selection	All selection
$W \to e\nu$	(6.7 ± 0.3) %	(34.6 ± 9.2)%
$W \to \mu\nu$	(8.6 ± 0.1) %	(0.2 ± 0.1)%
$W \to \tau\nu$	(21.9 ± 0.3) %	(44.6 ± 9.4)%
$Z \to \nu\nu$	(52.2 ± 0.6) %	(4.5 ± 1.6)%
$Z \to \ell\ell$	(0.5 ± 0.0) %	(0.4 ± 0.5)%
Di-boson	(1.7 ± 0.0) %	(2.4 ± 0.7)%
t-quark	(5.1 ± 0.1) %	(13.2 ± 3.0)%
Multi-jets	(3.4 ± 1.1) %	(0.0 ± 0.0)%

Table 6.2: The fraction of the SM process (a) after the kinematic selection and (b) after all the selection.

6.4 Disappearing track selection

A tracklet selection described in Sec. 5.2.2 is applied to events after applying the kinematic selection. A category for the events which pass both the kinematic selection and the disappearing track selection is called "signal region". A cut-flow is shown in Table 6.3. Requiring a track satisfied with the disappearance condition reduces both signal events and background events due to the signal acceptance and the no disappearing tracks in the SM processes, respectively. On the other hand, other requirements on tracklets, especially the impact parameter requirement and the quality requirement,

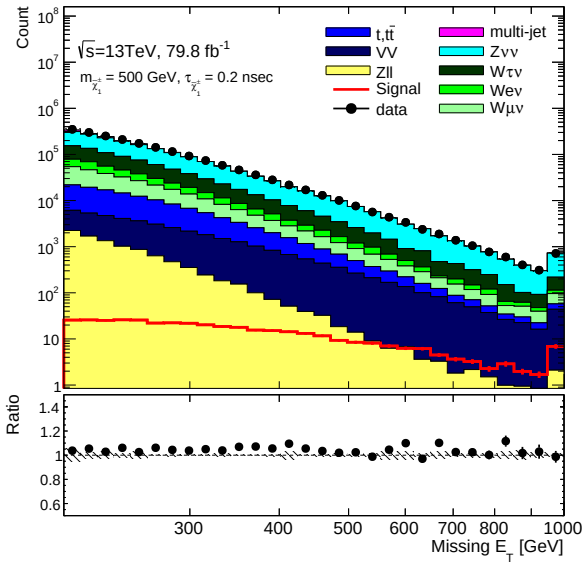

Figure 6.5: $E_{\mathrm{T}}^{\mathrm{miss}}$ distribution after kinematical selection. As signal samples, wino LSP models with a mass of 500 GeV and a lifetime of 0.2 ns are used. The data are shown in black points. Signal distributions are shown in red lines. The Standard Model processes are shown in different colours.

reject a large fraction of backgrounds compared to the signals, because most of the tracklets in the events after the kinematic selection are fake tracklets.

Table 6.2 shows a fraction of background components. After only the kinematic selection, a dominant background is $Z \to \nu\nu$ process. On the other hand, after the track requirements, a dominant background is $W \to \tau\nu$ process, and the next largest fraction comes from $W \to e\nu$ process. A jet derived from a quark and a gluon is highly rejected by the tracklet selection. A source of tracklet background is leptons (electron, muon and tau) coming from a W production process.

Requirement	Number of events		
	Observed	SM background (MC)	Signal (m=500 GeV)
Kinematic selection	1.97×10^6	$(1.889 \pm 0.022)\times10^6$	394 ± 4
Disappearance condition	3.89×10^4	$(3.066 \pm 0.035)\times10^4$	27.4 ± 1.1
Geometrical acceptance	2.84×10^4	$(2.245 \pm 0.030)\times10^4$	24.3 ± 1.0
Overlap removal	2.38×10^4	$(1.823 \pm 0.028)\times10^4$	22.8 ± 1.0
Isolation	1.79×10^4	$(1.402 \pm 0.021)\times10^4$	21.3 ± 0.9
Impact parameter	114	128 ± 24	18.0 ± 0.9
Quality	79	89 ± 16	16.9 ± 0.8

Table 6.3: A cut-flow of tracklet selection after applying kinematic selections. A chargino sample with a mass of 500 GeV and a lifetime of 0.2 ns is used as signal samples. The Pixel dead module correction is not applied here.

Chapter 7

Background estimation

7.1 Overview

This analysis extracts the signal event yield by fitting with tracklet p_{T} shapes. This is because the tracklet p_{T} shapes are clearly different between the signal events and the background events. A background estimation based on only MC samples would be not reliable due to the mismodellings of the event generation and the detector description including material budget. In this analysis, the background estimation is based on data-driven technique, where most of the background estimation is done using only observed data.

A tracklet p_{T} shape of a background differs among the cause and the origin. Background components are as follows

1. Charged particles hardly scattered by material of the tracker, which is called "Scattered" background. This origin can be further separated as follows
   (a) Charged hadrons (electrons) inelastically-scattering (causing bremsstrahlung) then lost hits expected to be along the direction of the seed-tracks.
   (b) Muons failing reconstructions of tracks in both the inner detector and the muon spectrometer.
2. Tracklets which are formed from hits originating from two or more particles (called "Fake" background)

The scattered hadron backgrounds have nearly the same p_{T} shape as the particles which are not scattered by material. The p_{T} shape is estimated using the tracks originating from each background source which does not scatter. Tracklet p_{T} shape of the lepton backgrounds is constructed by evaluating the probability that a lepton leaves a disappearing pixel tracklet. The probability is determined by using a high purity lepton from Z-boson. Although the estimation of the p_{T} shape of the scattered backgrounds is based on the p_{T} distribution of the source particles, the estimation of the p_{T} distribution of the fake backgrounds is hard to be constructed from the p_{T} shape of the source

particles because the wrong-hit combination causes a wrong p_{T} measurement. The p_{T} shape of the fake backgrounds is estimated by extrapolating it from a fake-background enriched region.

The isolation with jets is required in a disappearing track selection. Applying this requirement reduces high p_{T} tracks from hadrons and electrons to a negligible level at a very high p_{T} region. However, due to the poor p_{T} resolution of tracklets, high p_{T} tracklets, which originate from a low p_{T} particle, may remain in the signal region. This effect is evaluated by using the smearing function as discussed in Sec. 5.2.4.

The p_{T} shape fitting without any constraints on the background event yield has less discovery sensitivity because the structure of the p_{T} shapes is smeared by the poor tracklet p_{T} resolution. This analysis evaluates the yields for each a background source from background enhanced samples in addition to the p_{T} shapes.

In this section, estimations of the p_{T} shape and the yield of each background sources are described.

7.2 Hadron

When a hadron interacts with material of the tracker, the hadron changes the direction or decays into other particles, and the outer hits produced by secondary charged particles are not able to be associated in the tracking algorithm, then the trajectory looks like disappearing and pass the disappearance condition. Since the scattered probability does not depend on the p_{T} shown in Fig. 7.1, the tracklet p_{T} distribution of the scattered hadrons is obtained by smearing the track p_{T} distribution of non-scattered hadrons without any p_{T}-dependent scaling.

In order to extract the p_{T} distribution of non-scattered hadrons in a similar condition to tracklets in the signal region, a similar track selection to the disappearing track selection is applied except for the requirements on the number of SCT hits, the number of TRT hits and adding a requirement on the calorimeter energy deposit as follows

1. The number of SCT hits is more than 6
2. The number of TRT hits is more than 15
3. $E_T^{\mathrm{clus40}}/p_{\mathrm{T}} > 0.3$,

where E_T^{clus40} is defined as the sum of calorimeter cluster energy associated with the track within a cone of ΔR=0.4. The first and the second requirements are to ensure that a track is not hardly scattered by the material and the track is not a fake. The third requirement on the energy deposit is required in order to suppress muon contamination shown in Fig. 7.2.

The p_{T} distribution of non-scattered hadrons extracted by applying all the requirements described above is shown in Fig. 7.3 (a). Due to the poor tracklet p_{T} resolution, the template used in a fitting in the signal region is emulated by smearing the p_{T} distribution with the resolution function measured in observed data as described in Sec. 5.2.4.

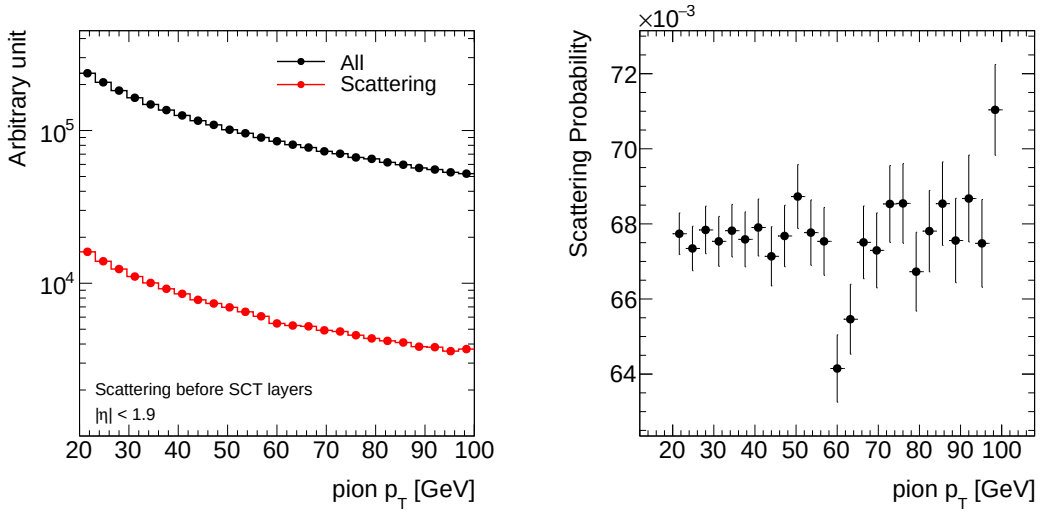

(a) (b)

Figure 7.1: (a) Pion p_{T} distribution in the simulated samples. All pions are shown as black points, and pions scattering before SCT detector are shown as red points. (b) Scattering probability as a function of pion p_{T}. The scattering probability in this p_{T} scale is independent of its energy.

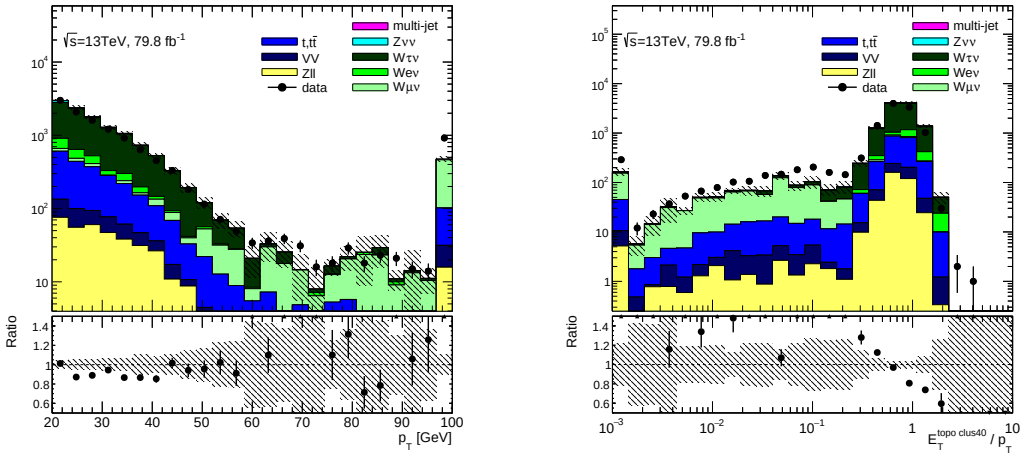

(a) Track p_{T} (b) $E_T^{\mathrm{clus40}}/p_{\mathrm{T}}$

Figure 7.2: (a) Track p_{T} and (b) $E_T^{\mathrm{clus40}}/p_{\mathrm{T}}$ before a requirement on the large energy deposit. Dark green filled histograms are $W \to \tau\nu$, and light green filled histograms are $W \to \mu\nu$. Although a dominant background is $W \to \tau\nu$, other tracks from $W \to \mu\nu$ process leaking from the lepton veto remains in high p_{T} regions.

Figure 7.3 (b) is a smeared p_{T} distribution. Small electron contamination around 70–90 GeV is negligible after smearing due to the poor p_{T} resolution.

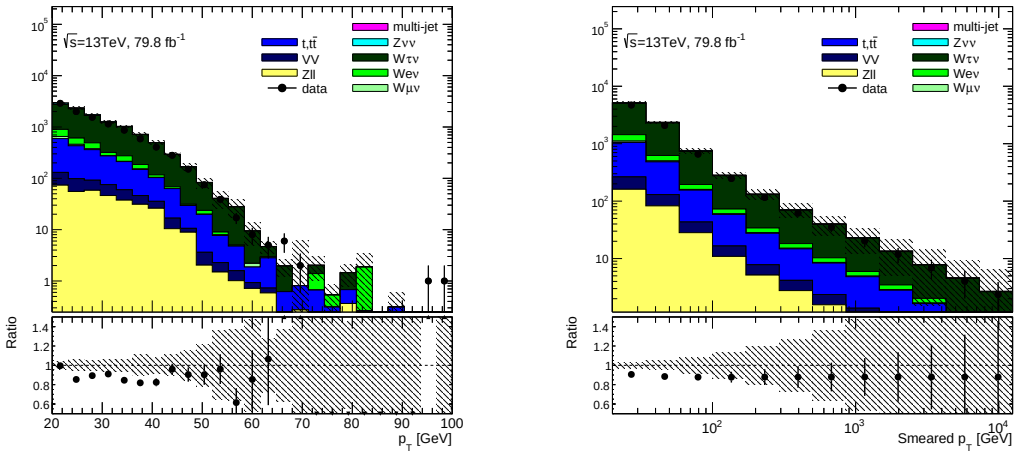

(a) Before smearing

(b) After smearing

Figure 7.3: Track p_{T} after requiring that $E_T^{\mathrm{clus40}}/p_{\mathrm{T}}$ is larger than 0.3. Muon candidates are rejected by the calorimeter requirement. (a) Track p_{T} before applying the p_{T} smearing. (b) Track p_{T} after applying the p_{T} smearing.

The bulk of the pion p_{T} shape is not changed by the calorimeter energy requirement because its threshold is small. However, the calorimeter requirement changes the tail fraction as shown in Fig. 7.4 (a) because the existence of high-energy calorimeter-clusters associated with a track enhances the existence of a high-energy jet which vetos the track due to the requirement on the isolation between the jet and the track. This difference disappears after smearing p_{T} due to the poor tracklet p_{T} resolution as shown in Fig. 7.4 (b).

A yield of the hadron background is effectively normalised at the low p_{T} region in the fitting. Since the number of low p_{T} tracklets is much larger than the high p_{T} tracklets as shown in Figure 7.3 (b) and most of the tracklets originating from signal charginos have high p_{T}, the number of high p_{T} hadron tracklets can be evaluated with small statistical uncertainties.

7.3 Lepton

Only electrons and muons are referred to as leptons here. Leptons can be clearly identified because they leave their characteristic signatures in the detector. Although they leave clear signatures, they may leave disappearing track signature and the lepton-identification fails because of missing the standard track originating from them. Using the benefit of leptons being easy to control, the number of lepton backgrounds in the sig-

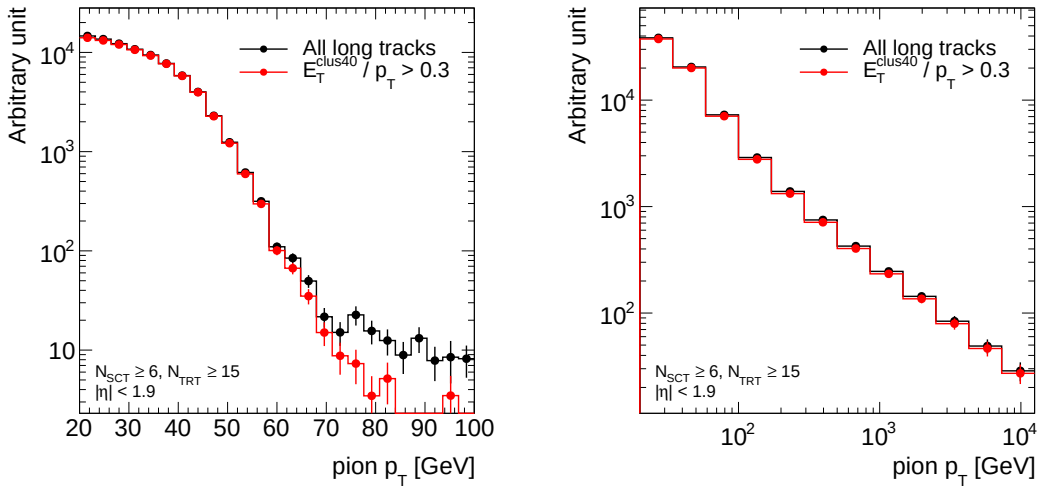

(a) (b)

Figure 7.4: Pion p_{T} distribution (a) with and (b) without the requirement on calorimeter.

nal region is estimated using the probability of a lepton being identified as a disappearing track.

Electrons and muons behave quite differently. Electrons leave their signs at the calorimeter. On the other hand, muons leave little energies in the calorimeter and leave tracks in the muon spectrometer. Due to the difference, two components are separately treated and evaluated.

The number and p_{T} shape of leptons in the signal region ($N_{\mathrm{SR}}(p_{\mathrm{T}})$) is estimated by converting the number and the p_{T} shape in the one-lepton region (control region) as the following formula

$$N_{\mathrm{SR}}(p_{\mathrm{T}}) = \sum_{\eta_i,\phi_j} \mathcal{P}(p_{\mathrm{T}},\eta_i,\phi_j) N_{\mathrm{CR}}(p_{\mathrm{T}},\eta_i,\phi_j), \tag{7.1}$$

where the first term, $\mathcal{P}$, is a transfer factor from the one-lepton events to zero-lepton events. It is defined as the ratio of the probability of the lepton having the pixel tracklets to the probability of the lepton having the standard tracks. The transfer factor is evaluated as a function of p_{T}, η and ϕ. The second term, N_{CR} is the number of leptons identified using the standard tracks in the one-lepton control region. Two terms are separately discussed in following sections.

Extraction of events with exactly one lepton

In order to extract a similar kinematical topology to the signal region, almost the same kinematical selection as in the signal region is used. The differences from the normal kinematical selection are the requirement on exactly one lepton instead of the lepton veto and the use of alternative $E_{\mathrm{T}}^{\mathrm{miss}}$ definition. Alternative $E_{\mathrm{T}}^{\mathrm{miss}}$ is calculated by excluding

the lepton term to emulate the case that the lepton is identified as a disappearing track. In the case of an electron failing a lepton identification, the electron energy contribution is added to the jet term because the electron deposits sizable energy in the calorimeter. On the other hand, in the muon case, since the corresponding jet term is quite small, the alternative $E_{\mathrm{T}}^{\mathrm{miss}}$ is quite different from the original one. This difference causes a difference in the kinematical distribution between electrons and muons as shown in Fig. 7.5 (a) and (b).

Events in the exactly one lepton region are triggered by single isolated-lepton triggers [32, 90, 94, 95]. For the electron trigger, it is required that the p_{T} of an electron is higher than 22 GeV in the Level-1 trigger and 26 GeV in the High-Level-Trigger, and the electron satisfies the "Tight" quality criteria and is isolated. For selecting muon events, it is required that the p_{T} of a muon is higher than 15 or 20 GeV in the Level-1 trigger and 22–26 GeV in the High-Level-Trigger, and the muon is isolated.

A lepton is required to have an isolated inner-detector track satisfying the disappearing track selection except for some conditions

1. p_{T} is greater than 15 GeV instead of 5 GeV
2. the number of TRT hits is more than 5 instead of the TRT veto
3. No requirement on the SCT hits is applied
4. No requirement on isolation with jets is applied.

Figure 7.5 (c) and (d) show lepton p_{T} distributions in the lepton control regions. The difference between electrons and muons comes from the $E_{\mathrm{T}}^{\mathrm{miss}}$ definition mentioned above and the difference in calorimeter energy deposit. A difference of normalisation between data and MC in Fig. 7.5 comes from a Pixel dead module as discussed in Sec. 5.2.4 because the scale factor is not applied here.

An estimation of the transfer factor from good leptons to disappearing tracks

The first term of Eq. 7.1 is measured using $Z \to \ell\ell$ events. In order to ensure that disappearing tracks come from leptons, the events are required to contain the following signatures

1. One lepton identified as high purity leptons (named as "tag" lepton)
   (a) $p_{\mathrm{T}} > 30$ GeV
   (b) $|\eta| < 2.5$
   (c) $|\eta| < 1.37$ and $1.52 < |\eta|$ for electrons
   (d) Identified as "Tight" quality as described in Sec. 4.
2. One isolated track associated with characteristic signature used in lepton reconstruction steps (named as "probe" lepton)

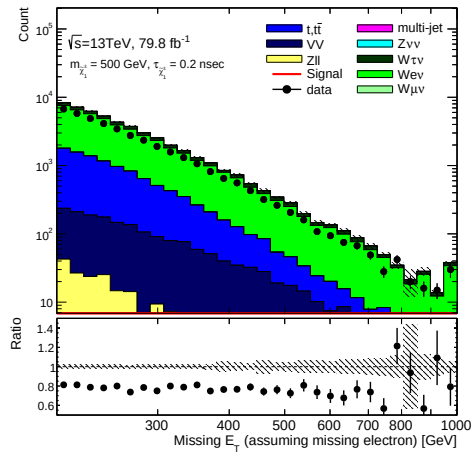

(a)

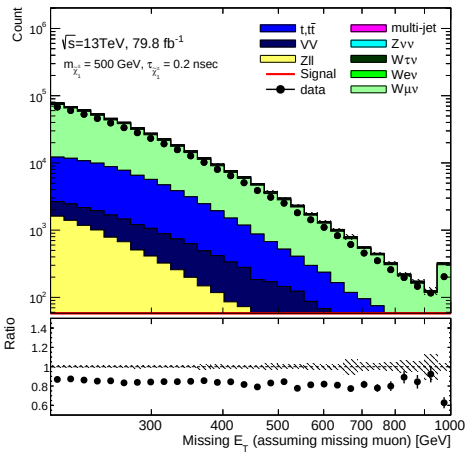

(b)

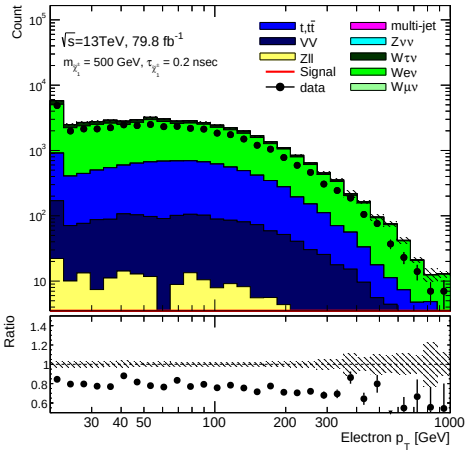

(c)

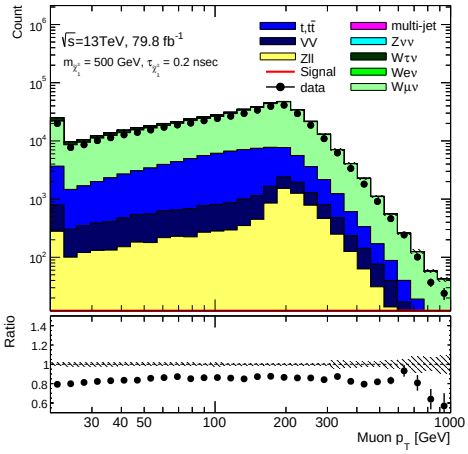

(d)

Figure 7.5: One lepton events (a) $E_{\mathrm{T}}^{\mathrm{miss}}$ distribution in electron control region (b) $E_{\mathrm{T}}^{\mathrm{miss}}$ distribution in muon control region (c) Electron p_{T} distribution in electron control region (d) Muon p_{T} distribution in muon control region

(a) For electron case, a track is associated with an electromagnetic calorimeter cluster with the p_{T} higher than 10 GeV and $|\eta|$ smaller than 2.5.

(b) For muon case, a track is associated with a muon-spectrometer track with the p_{T} higher than 10 GeV and $|\eta|$ smaller than 2.5.

3. An event has the above two objects and the mass reconstructed from tag lepton and probe lepton is within a narrow mass window around the Z mass.

   (a) $|M_{\mathrm{tag,probe}} - M_{\mathrm{Z}}| < 10$ GeV, where $M_{\mathrm{tag,probe}}$ is a reconstructed mass from a tag lepton and a probe lepton.

   (b) $\Delta\phi$(tag, probe) > 0.1

The events are selected by using single-isolated-lepton triggers. In order to extract the only clean $Z \to \ell\ell$ events, the events having more than two different lepton flavours are rejected.

By using high purity lepton objects extracted here, a ratio of the probability of probe lepton having an associated tracklet to that of the probe lepton having an associated standard track is evaluated. In order to use tracks with a similar condition with the disappearing track candidates, the associated standard tracks and the associated pixel tracklets are required to pass track selections as follows

1. $p_{\mathrm{T}} > 15$ GeV
2. Isolation with jets are applied only for pixel tracklet selection
3. No different flavour leptonic objects around the tracks
   (a) ΔR(track, muons) > 0.4 for electrons
   (b) ΔR(track, MS-tracks) > 0.4 for electrons
   (c) ΔR(track, electrons) > 0.4 for muons
4. ΔR(tracks, probe) < 0.2
5. The number of TRT hits is more than 5 for standard track selection
6. No hits in SCT and TRT for pixel-tracklet selection

Figure 7.6 show the di-lepton mass ($M_{\mathrm{tag,probe}}$) distribution with a requirement on tracks associated with the probe lepton. A difference between data and MC simulation comes from the mismodelling of Pixel detector condition discussed in Sec. 5.2.4. Most of the events around the Z-mass peak are produced by $Z \to \ell\ell$ events, and the contamination from other particles is small enough to be neglected. The small mismodelling around the Z-mass peak comes from the absence of the energy calibration, which is used for reconstructed lepton, for the energy of EM calorimeter and MS tracks. As this mismodelling does not affect the purity of lepton events very much, no additional corrections of EM clusters and MS tracks are applied.

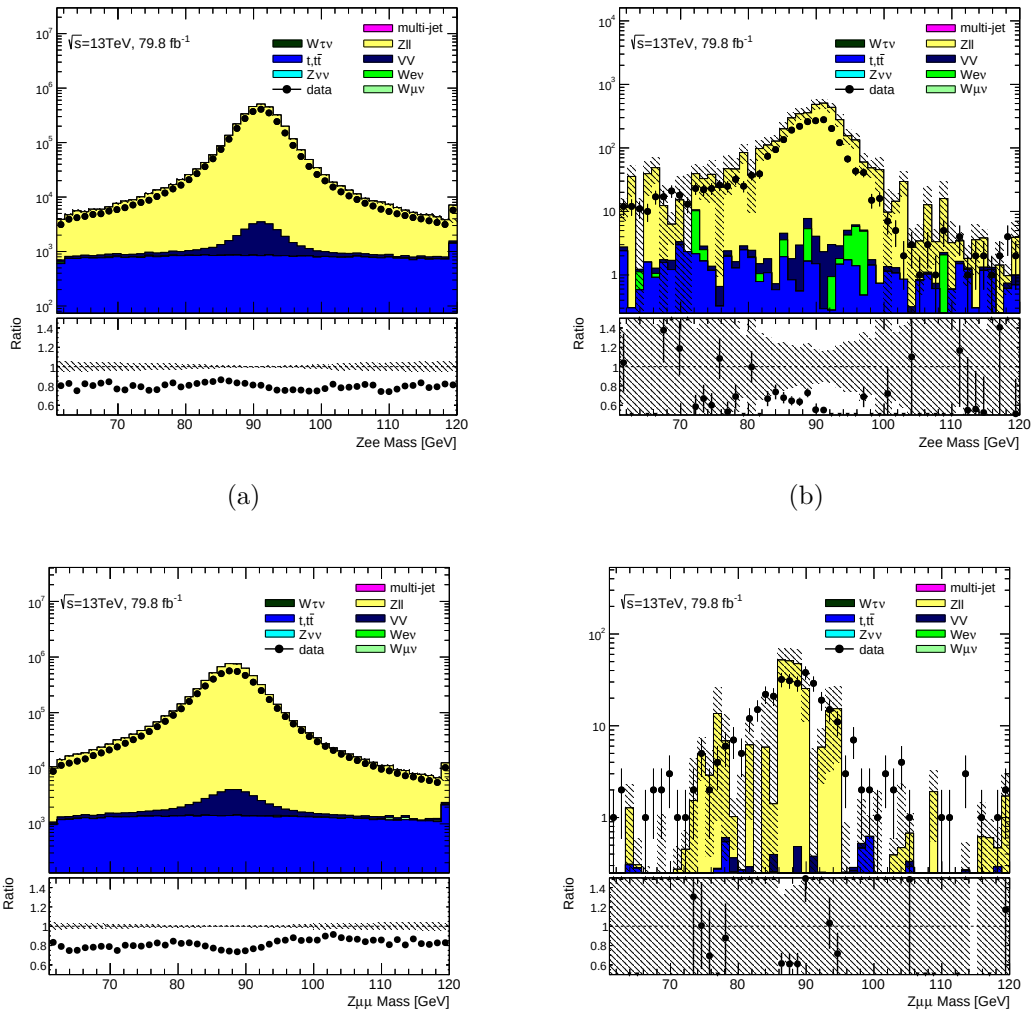

Figure 7.6: Di-lepton mass distribution with a large mass window ($|M_{\mathrm{tag,probe}} - M_{\mathrm{Z}}| < 30$ GeV). (a) $Z \to ee$ associated with the long standard tracks (b) $Z \to ee$ associated with pixel tracklets (c) $Z \to \mu\mu$ associated with the long standard tracks (d) $Z \to \mu\mu$ associated with pixel tracklets

The transfer factor is calculated as the ratio of the number of events having pixel tracklets to those having the standard tracks as a function of p_{T} and η. Figure 7.7 shows the transfer factor for electrons. Electrons leave large fractions of energies in the calorimeter. Therefore high p_{T} electrons do not pass the disappearing track selection due to the isolation requirement with jets. An η dependence in the transfer factors is due to the material budget of the inner tracker shown in Fig. 2.3. Figure 7.8 shows the transfer factor for muons. The p_{T} dependencies of muon are different because muons do not leave their energies in the calorimeter like electrons. Since muons are heavier than electrons and produce bremsstrahlung less frequently, the transfer factor for muons is smaller than electrons.

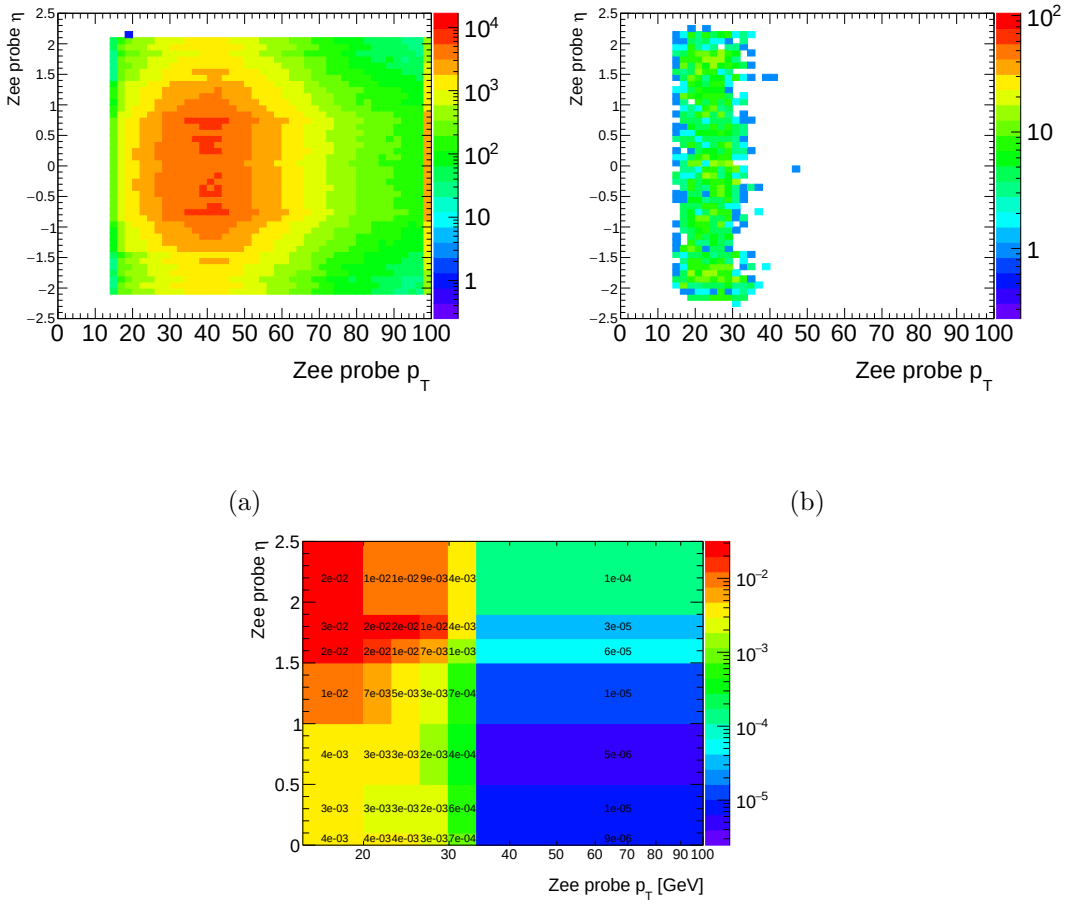

Figure 7.7: (a) The number of electrons associated with the long standard tracks as function of p_{T}-η. (b) The number of electrons associated with the pixel tracklets as function of p_{T}-η. (c) The ratio of the number of electrons having pixel tracklets to those having the standard tracks (transfer factor) as function of p_{T}-η.

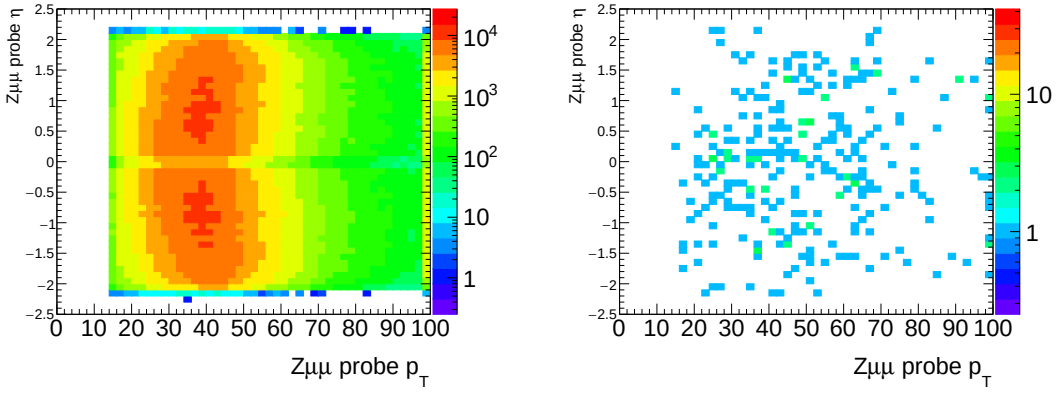

(a) (b)

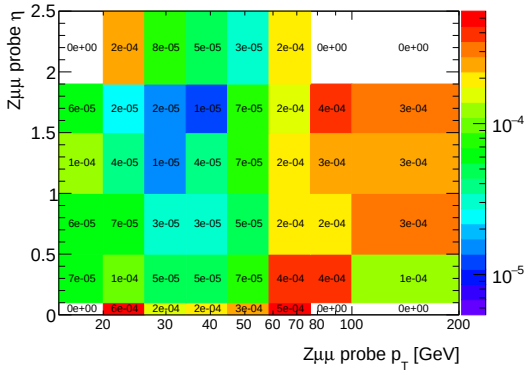

(c)

Figure 7.8: (a) The number of muons associated with the long standard tracks as function of p_{T}-η. (b) The number of muons associated with the pixel tracklets as function of p_{T}-η. (c) The ratio of the number of muons having pixel tracklets to those having the standard tracks (transfer factor) as function of p_{T}-η.

Tag and Probe method for estimation of MSTracks

In the disappearing track selection, a veto of muon-spectrometer tracks is required. Therefore, as the transfer factor of muons, the effects should be added in addition to the transfer factor of MS-tracks. For the estimation of the MS-track transfer factor, $Z \to \mu\mu$ events are used. The ratio of the probability of a lepton not having a muon-spectrometer track to that of a lepton having a muon-spectrometer track is evaluated.

1. One lepton identified as high purity leptons (named as "tag" lepton)
   (a) $p_{\mathrm{T}} > 20$ GeV
   (b) $|\eta| < 2.5$
   (c) Identified as "Tight"
2. One isolated inner-detector tracks (named as "probe" lepton)
   (a) $p_{\mathrm{T}} > 15$ GeV
   (b) $|\eta| < 2.5$
   (c) Normal disappearing track condition, except an isolation with muons and SCT veto
3. An event has the above two objects and the mass reconstructed from tag lepton and probe lepton is within a narrow mass window around the Z mass.
   (a) $|M_{\mathrm{tag,probe}} - M_{\mathrm{Z}}| < 10$ GeV
   (b) $\Delta\phi$(tag, probe) > 0.1
   (c) No electrons

And events need to be triggered by the isolated single muon trigger.

For MS tracks, the following selections are required.

1. $p_{\mathrm{T}} > 5$ GeV
2. ΔR(probe inner-detector track, MS-track) < 0.2

Figure 7.9 shows the mass distribution in this selection. As shown in Fig. 7.9 (b), high purity $Z \to \mu\mu$ events are selected.

Figure 7.10 shows the transfer factor as a function of η and ϕ of muon probes. Unlike the inner detector, the muon spectrometer is not uniform in ϕ as shown in Fig. 7.10 (c). A peak around $\eta = 0$ is due to the inactive region of the muon spectrometer. This region is not used in this search.

Template for the signal region

Figure 7.11 show the two-dimensional distribution of electrons as a function of p_{T} and η and that of muons as a function of η and ϕ after applying each transfer factor. The p_{T} templates after applying the smearing method to the lepton p_{T} in the one-lepton control region shown in Fig. 7.5 (c) and (d) are shown in Fig. 7.12. As shown in Fig. 7.12, $W \to \ell\nu$ events are dominant backgrounds.

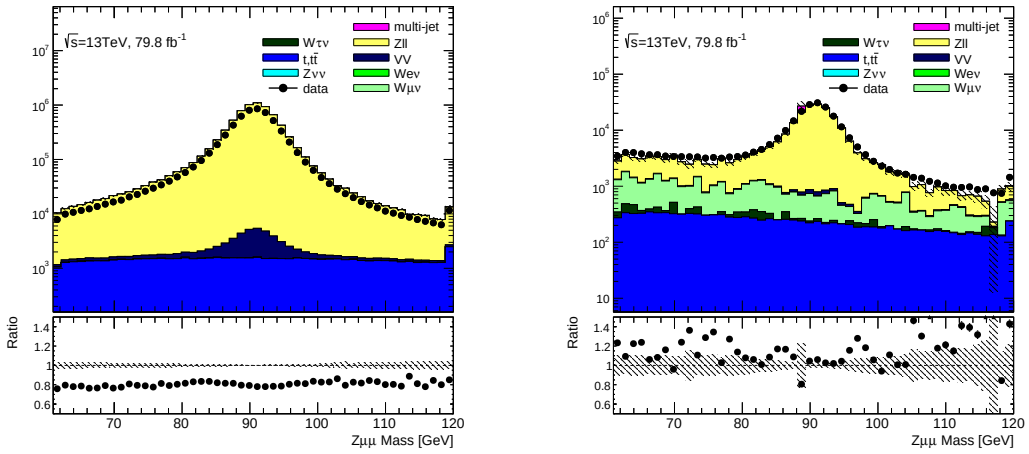

(a) (b)

Figure 7.9: Di-muon mass distribution. (a) $Z \to \mu\mu$ events associated with MS-tracks (b) $Z \to \mu\mu$ events not associated with MS-tracks

7.4 Fake

Fake tracklets are formed from a wrong combination of hits. In this case, tracklets have almost a random p_{T} and d_0 significance distribution. Since there is no correlation between them, tracklets with large d_0 significance are used as a control sample.

Figure 7.13 shows a d_0 significance distribution after an application of all selection with loose $E_{\mathrm{T}}^{\mathrm{miss}}$ selection ($E_{\mathrm{T}}^{\mathrm{miss}} > 120$ GeV) and except for the d_0 significance selection, where one-wrong-combination is defined as one of the hits in tracks does not come from the same particle and multi-wrong-combination is defined as two or more hits in tracks do not come from the same particle. The difference in the d_0 significance between data and MC is due to misalignment in the detector and other imperfection in the modelling of the simulation. Most of the tracklets having d_0 significance larger than 10 come from a wrong combination of hits.

To extract the p_{T} template for the fake background, large d_0 significance (> 10) is required. Figure 7.14 shows the p_{T} distribution in the fake control region, where an empirical function

$$f(p_{\mathrm{T}}) = e^{A \log p_{\mathrm{T}} + B(\log p_{\mathrm{T}})^2} \tag{7.2}$$

is used to fit data. This function is a quadratic function for a log-log axis, and able to model the p_{T} shape in the fake control region.

The yield of fake tracklet background in the signal region is evaluated using the so-called ABCD method. When there is no correlation between a variable a and b, the double ratio

$$r_{\mathrm{ABCD}} = \frac{N(a \in A, b \in B)}{N(a \in A', b \in B)} \Big/ \frac{N(a \in A, b \in B')}{N(a \in A', b \in B')}, \tag{7.3}$$

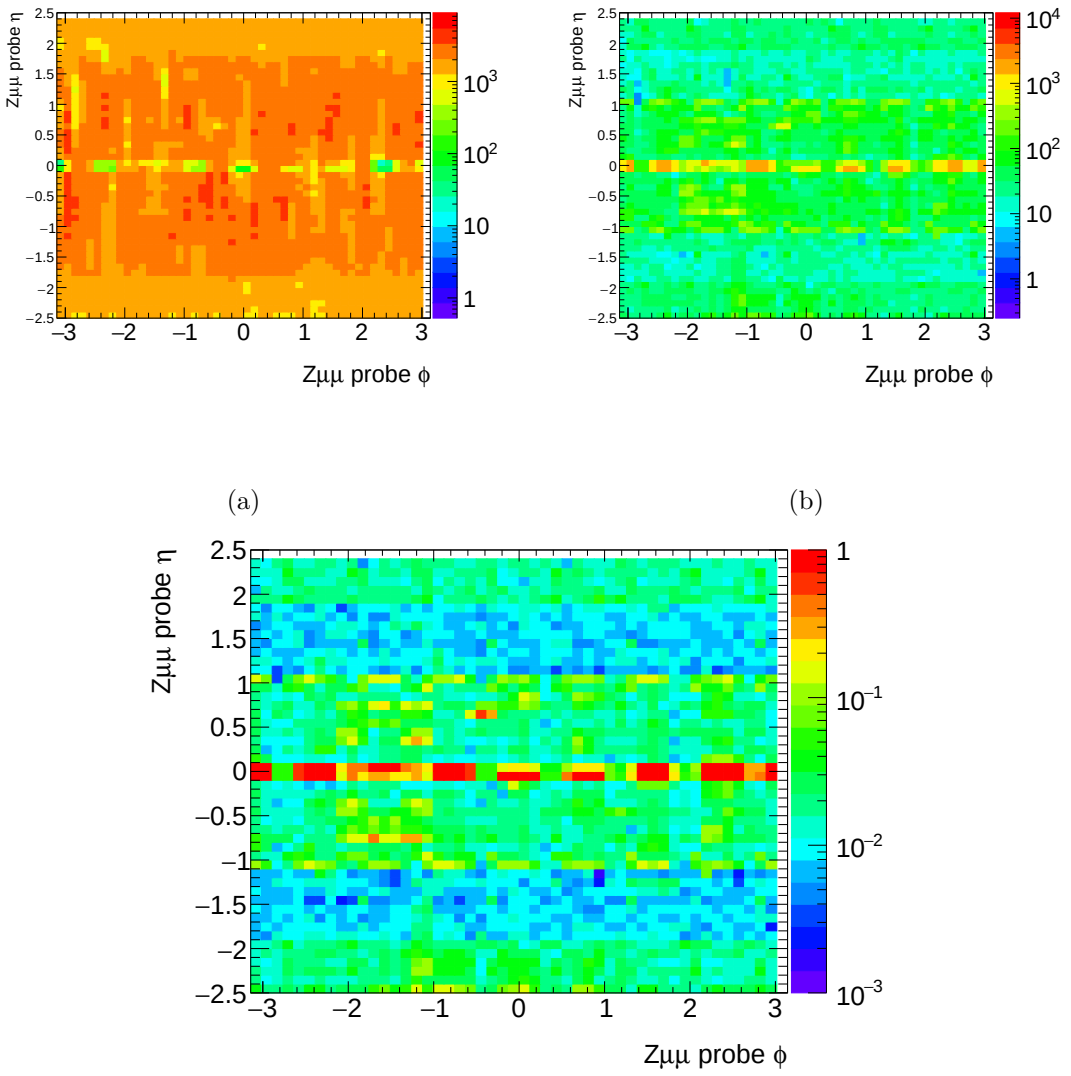

Figure 7.10: (a) The number of the standard tracks associated with MS tracks as function of ϕ-η. (b) The number of the standard tracks not associated with MS tracks as function of ϕ-η. (c) The ratio of the number of the standard tracks associated with MS-tracks to those not associated with MS-tracks (transfer factor of MS-tracks) as function of ϕ-η.

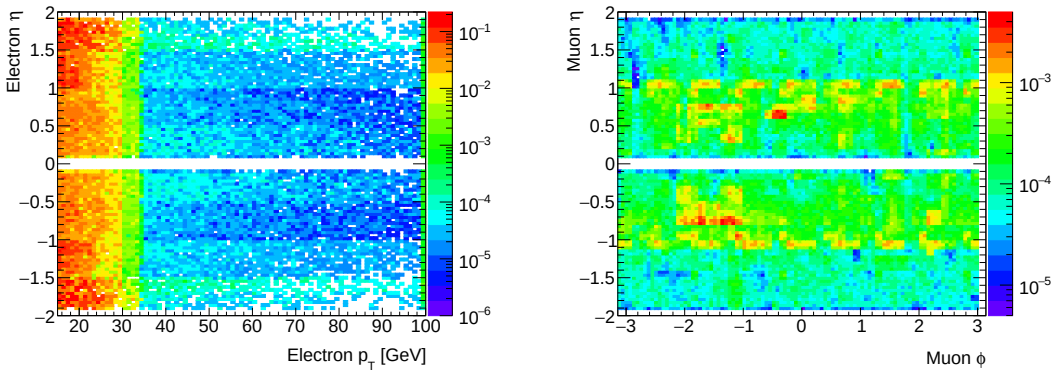

(a) (b)

Figure 7.11: (a) Two dimensional distribution of electrons as a function of p_{T} and η after applying transfer factor. (b) Two dimensional distribution of muons as a function of η and ϕ after applying transfer factor.

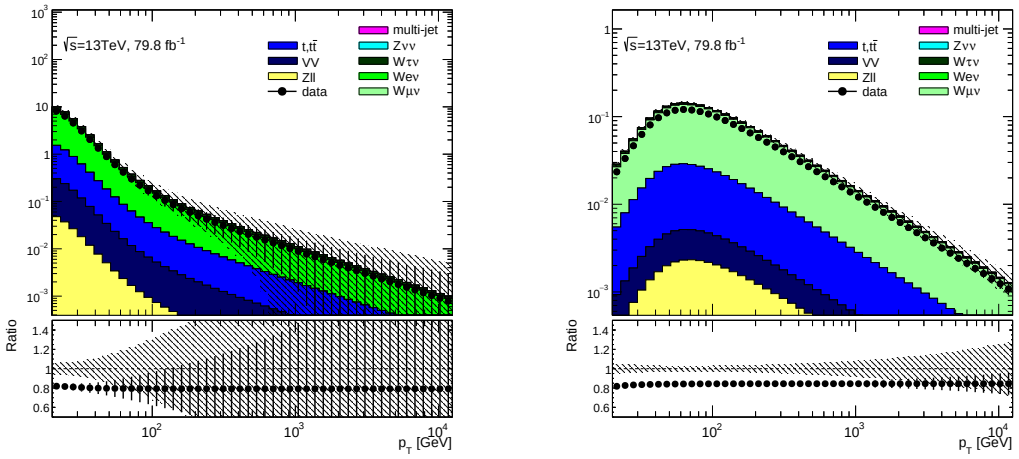

(a) (b)

Figure 7.12: p_{T} template after p_{T} smearing (a) for electron (b) for muon. Black points are observed data. Filled histograms are MC simulated samples. The same smearing function, which is measured from observe data, is applied for both observed data and MC simulated samples.

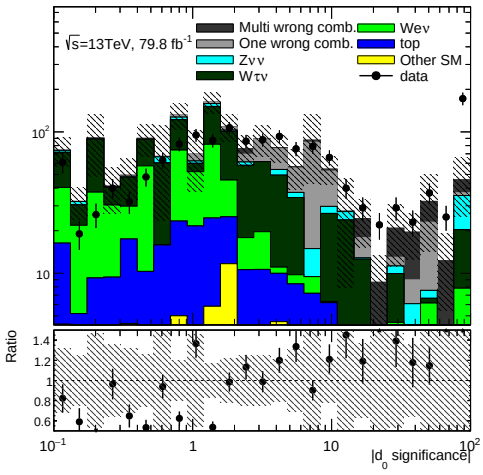

Figure 7.13: $|d_0$ significance$|$ distribution after all selection with loose $E_{\mathrm{T}}^{\mathrm{miss}}$ selection ($E_{\mathrm{T}}^{\mathrm{miss}} > 120$ GeV) and except for d_0 significance selection. Black point shows observed data, and filled histograms show the SM simulated process. Light grey and dark grey histograms show fake tracklets.

where $N(a \in A, b \in B)$ represents the number of events where variable a is satisfied with the condition A and variable b is satisfied with the condition B, is expected to be unity typically. The number of events in the interesting region ($N(a \in A, b \in B)$) is evaluated from the other three regions. The d_0 significance value of a pixel tracklet does not depend on the $E_{\mathrm{T}}^{\mathrm{miss}}$ value, because track information of the pixel tracklet is not used in the $E_{\mathrm{T}}^{\mathrm{miss}}$ calculation. The number of fake tracks in the signal region can be evaluated by the formula

$$N_{\text{small d}_0\text{,large E}_{\mathrm{T}}^{\mathrm{miss}}} = N_{\text{small d}_0\text{,low E}_{\mathrm{T}}^{\mathrm{miss}}} \times \frac{N_{\text{large d}_0\text{,large E}_{\mathrm{T}}^{\mathrm{miss}}}}{N_{\text{large d}_0\text{,low E}_{\mathrm{T}}^{\mathrm{miss}}}}, \tag{7.4}$$

where low $E_{\mathrm{T}}^{\mathrm{miss}}$ and large $E_{\mathrm{T}}^{\mathrm{miss}}$ region are defined as 120 GeV $< E_{\mathrm{T}}^{\mathrm{miss}} <$ 200 GeV and 200 GeV $< E_{\mathrm{T}}^{\mathrm{miss}}$, respectively, and small d_0 and large d_0 regions are defined as $|d_0$ significance$| < 1.5$ and $|d_0$ significance$| > 10$, respectively.

Figure 7.15 shows a dependence on d_0 significance and $E_{\mathrm{T}}^{\mathrm{miss}}$. The p_{T} shape is independent of the $E_{\mathrm{T}}^{\mathrm{miss}}$ and d_0 significance within an uncertainty of the fit function.

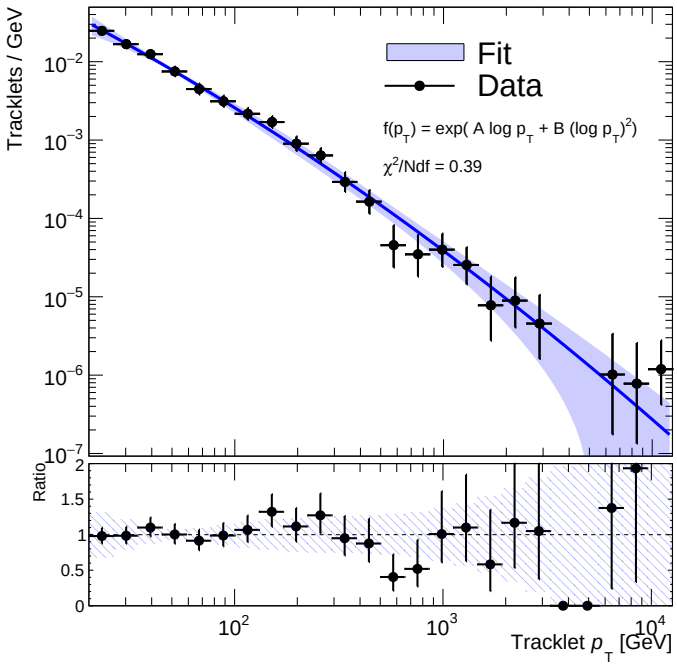

Figure 7.14: The transverse momentum of tracklets in the fake control region. Observed data are shown as black points. The fit function is shown as a blue line and the blue band is the 1-σ uncertainty.

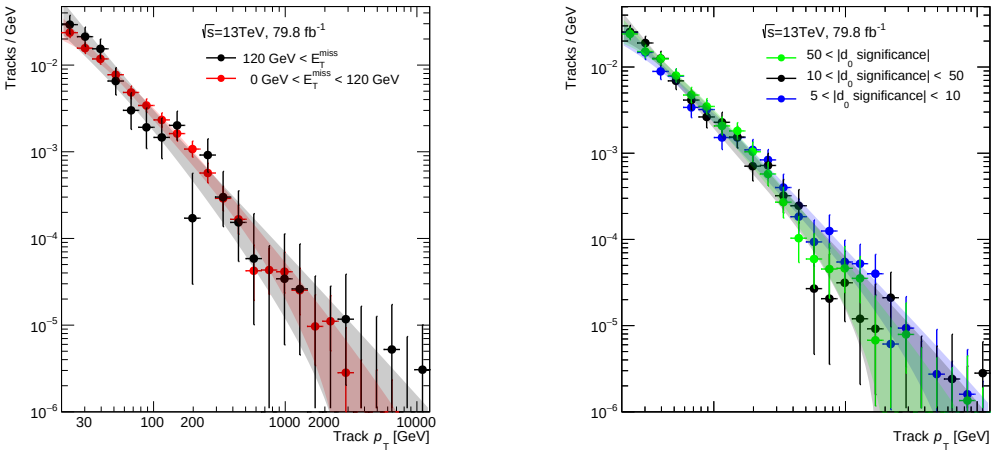

(a) (b)

Figure 7.15: Dependence of the fake-tracklet p_{T} on (a) the $E_{\mathrm{T}}^{\mathrm{miss}}$ requirement with d_0 significance > 10 and (b) the d_0 significance requirement with no $E_{\mathrm{T}}^{\mathrm{miss}}$ requirement.

Chapter 8

Extraction of signal yield

A signal yield is extracted by using an unbinned extended maximum likelihood technique. A likelihood function consists of sub-terms about the total number in the signal region, p_{T} shape and systematic uncertainties. A p_{T} shape for signal charginos is constructed using a generator-level p_{T} distribution of the charginos which pass the event selection, then the p_{T} distribution is smeared using the smearing function as discussed in Sec. 5.2.4. p_{T} shapes for background is already discussed in Chapter 7. In order to constrain the fake track events, the high $E_{\mathrm{T}}^{\mathrm{miss}}$ region ($E_{\mathrm{T}}^{\mathrm{miss}} > 200$ GeV) and low $E_{\mathrm{T}}^{\mathrm{miss}}$ region (120 GeV $< E_{\mathrm{T}}^{\mathrm{miss}} < 200$ GeV) are fit simultaneously.

8.1 Unbinned extended maximum likelihood fit

The likelihood function ($\mathcal{L}$) for the tracklet p_{T} in an ensemble of observed events is defined as

$$\begin{aligned}
\mathcal{L}(\mu_s, \boldsymbol{n}^{\mathrm{H}}, \boldsymbol{n}^{\mathrm{L}}, \boldsymbol{\theta}, r_{\mathrm{f}} \mid \vec{p_{\mathrm{T}}}) \equiv & \prod_{R\in\{H,L\}} \mathcal{P}(n_{\mathrm{obs}}^{\mathrm{R}} | \mu_s n_{\mathrm{s}}^{\mathrm{R}} + n_{\mathrm{h}}^{\mathrm{R}} + n_{\mathrm{e}}^{\mathrm{R}} + n_{\mu}^{\mathrm{R}} + n_{\mathrm{f}}^{\mathrm{R}}) \\
\times & \prod_{R\in\{H,L\}} \mathcal{L}_{\mathrm{shape}}(\vec{p_T}; \mu_s, \boldsymbol{n}^{\mathrm{R}}, \boldsymbol{\theta}) \\
\times & \prod_{R\in\{H,L\}} \mathcal{L}_{\mathrm{sys}}(\boldsymbol{n}^{\mathrm{R}}), \\
\times & \mathcal{L}_{\mathrm{sys}}(\boldsymbol{\theta}), \\
\times & \mathcal{L}_{\mathrm{sys,fake}}(\boldsymbol{n}^{\mathrm{H}}, \boldsymbol{n}^{\mathrm{L}}, r_{\mathrm{f}}). \qquad (8.1)
\end{aligned}$$

The first term is an extended term and constrains the sum of the number of each components by the observed number of events, where $n_{\mathrm{obs}}^{\mathrm{H(L)}}$, $n_{\mathrm{s}}^{\mathrm{H(L)}}$, $n_{\mathrm{h}}^{\mathrm{H(L)}}$, $n_{\mathrm{e}}^{\mathrm{H(L)}}$, $n_{\mu}^{\mathrm{H(L)}}$ and $n_{\mathrm{f}}^{\mathrm{H(L)}}$ are the number of total observed events, signal events for a given model, hadron track events, electron track events, muon track events and fake track events in the signal region, respectively. "H (L)" represents high (low) $E_{\mathrm{T}}^{\mathrm{miss}}$ region. The function

of $\mathcal{P}(n|\mu)$ represents the Poisson distribution

$$\mathcal{P}(n|\mu) = \frac{\mu^n e^{-\mu}}{n!}. \tag{8.2}$$

The second term is a shape term and evaluates the probability of the observed p_{T} for each event. The variables, $\boldsymbol{n}^{\mathrm{H\ (L)}}$ and $\boldsymbol{\theta}$, are the number of events for each source and the systematic uncertainties for the p_{T} template, respectively, as follows

$$\begin{aligned}
\boldsymbol{n}^{\mathrm{H}} &\equiv \{n_{\mathrm{s}}^{\mathrm{H}}, n_{\mathrm{h}}^{\mathrm{H}}, n_{\mathrm{e}}^{\mathrm{H}}, n_{\mu}^{\mathrm{H}}, n_{\mathrm{f}}^{\mathrm{H}}, n_{\mathrm{FakeCR}}^{\mathrm{H}}\} && (8.3)\\
\boldsymbol{n}^{\mathrm{L}} &\equiv \{n_{\mathrm{s}}^{\mathrm{L}}, n_{\mathrm{h}}^{\mathrm{L}}, n_{\mathrm{e}}^{\mathrm{L}}, n_{\mu}^{\mathrm{L}}, n_{\mathrm{f}}^{\mathrm{L}}, n_{\mathrm{FakeCR}}^{\mathrm{L}}\} && (8.4)\\
\boldsymbol{\theta} &\equiv \{\vec{\theta}_{\mathrm{s}}, \vec{\theta}_{\mathrm{h}}, \vec{\theta}_{\mu}, \vec{\theta}_{\mathrm{e}}, \vec{\theta}_{\mathrm{f}}\} && (8.5)\\
\vec{\theta}_{\mathrm{s}} &\equiv \{\sigma_{\mathrm{s}}^{\mathrm{smear}}, \alpha_{\mathrm{s}}^{\mathrm{smear}}\} && (8.6)\\
\vec{\theta}_{\mathrm{h}} &\equiv \{\sigma_{\mathrm{h}}^{\mathrm{smear}}, \alpha_{\mathrm{h}}^{\mathrm{smear}}, \nu_{\mathrm{h}}^{\mathrm{smear}}\} && (8.7)\\
\vec{\theta}_{\mu} &\equiv \left\{\sigma_{\mu}^{\mathrm{smear}}, \alpha_{\mu}^{\mathrm{smear}}\right\} && (8.8)\\
\vec{\theta}_{\mathrm{e}} &\equiv \{\sigma_{\mathrm{e}}^{\mathrm{smear}}, \alpha_{\mathrm{e}}^{\mathrm{smear}}, \nu_{\mathrm{e}}^{\mathrm{smear}}\} && (8.9)\\
\vec{\theta}_{\mathrm{f}} &\equiv \left\{p_0^{\mathrm{fit}}, p_1^{\mathrm{fit}}\right\}, && (8.10)
\end{aligned}$$

where the parameters $\vec{\theta}_{\mathrm{h}}$, $\vec{\theta}_{\mu}$, $\vec{\theta}_{\mathrm{e}}$, $\vec{\theta}_{\mathrm{s}}$ and $\vec{\theta}_{\mathrm{f}}$ are nuisance parameters used to include uncertainties in the hadron smearing function, muon smearing function, electron smearing function, signal smearing function and fake background p_{T}-spectra, respectively. The formulation of $\mathcal{L}_{\mathrm{shape}}$ is given as

$$\mathcal{L}_{\mathrm{shape}}(\vec{p_T}; \mu_s, \boldsymbol{n}, \boldsymbol{\theta}) = \prod^{n_{\mathrm{obs}}} \frac{\mu_s n_{\mathrm{s}} \mathcal{F}_{\mathrm{s}}(p_T; \vec{\theta}_{\mathrm{s}}) + \sum_{c\in\{h,e,\mu,f\}} n_{\mathrm{c}} \mathcal{F}_{\mathrm{c}}(p_T; \vec{\theta}_{\mathrm{c}})}{\mu_s n_{\mathrm{s}} + \sum_{c\in\{h,e,\mu,f\}} n_{\mathrm{c}}}, \tag{8.11}$$

where $\mathcal{F}_{\mathrm{s}}$, $\mathcal{F}_{\mathrm{h}}$, $\mathcal{F}_{\mathrm{e}}$, $\mathcal{F}_{\mu}$ and $\mathcal{F}_{\mathrm{f}}$ are the probability density functions of signals, hadrons, electrons, muons and fake tracks, respectively.

The third term is for systematic uncertainties of the number of events of signal, electron and muon components. The formulation of $\mathcal{L}_{\mathrm{syst}}$ is given as

$$\mathcal{L}_{\mathrm{syst}}(\boldsymbol{n}) = Bi\mathcal{N}(n_{\mathrm{s}} \mid n_{\mathrm{s}}^{\mathrm{exp}}, \sigma_{d,n_{\mathrm{s}}}^2, \sigma_{u,n_{\mathrm{s}}}^2) \times \prod_{c\in\{e,\mu\}} \mathcal{N}(n_{\mathrm{c}} \mid n_{\mathrm{c}}^{\mathrm{exp}}, \sigma_{n_{\mathrm{c}}}^2), \tag{8.12}$$

where the function of $\mathcal{N}(x \mid \mu, \sigma^2)$ and $Bi\mathcal{N}(x \mid \mu, \sigma_d^2, \sigma_u^2)$ represent a normal distribution and an asymmetric Gaussian distribution

$$\mathcal{N}(x \mid \mu, \sigma^2) = \frac{1}{\sqrt{2\pi\sigma^2}} \exp\left(-\frac{(x-\mu)^2}{2\sigma^2}\right) \tag{8.13}$$

$$Bi\mathcal{N}(x \mid \mu, \sigma_{\mathrm{d}}^2, \sigma_{\mathrm{u}}^2) = \begin{cases} \exp\left(-\frac{(x-\mu)^2}{2\sigma_{\mathrm{d}}^2}\right) & x < \mu \\ \exp\left(-\frac{(x-\mu)^2}{2\sigma_{\mathrm{u}}^2}\right) & \text{other} \end{cases}, \tag{8.14}$$

where μ is the expected mean and σ is the uncertainty. The uncertainties are summarised in Sec. 9.

The fourth term is for systematic uncertainties for a p_{T} smearing function and the formulation is given as

$$\begin{aligned}\mathcal{L}_{\mathrm{syst}}(\boldsymbol{\theta}) &= \prod_{c\in\{s,e,h,\mu\}} \mathcal{N}(\sigma_{\mathrm{c}}^{\mathrm{smear}} \mid \sigma_{\mathrm{c}}^{\mathrm{smear,exp}}, \sigma^2_{\sigma_{\mathrm{c}}^{\mathrm{smear}}}) \\ &\times \prod_{c\in\{s,e,h,\mu\}} \mathcal{N}(\alpha_{\mathrm{c}}^{\mathrm{smear}} \mid \alpha_{\mathrm{c}}^{\mathrm{smear,exp}}, \sigma^2_{\alpha_{\mathrm{c}}^{\mathrm{smear}}}) \\ &\times \prod_{c\in\{e,h\}} \mathcal{N}(\nu_{\mathrm{c}}^{\mathrm{smear}} \mid \nu_{\mathrm{c}}^{\mathrm{smear,exp}}, \sigma^2_{\nu_{\mathrm{c}}^{\mathrm{smear}}}), \end{aligned} \tag{8.15}$$

The last term is for systematic uncertainties related with a fake tracklet. r_{f} represents a logarithmic ratio for the number in the ABCD method as follow

$$r_{\mathrm{f}} = \log r_{\mathrm{ABCD}} = \log\left(\frac{n_{\mathrm{f}}^{\mathrm{H}}/n_{\mathrm{FakeCR}}^{\mathrm{H}}}{n_{\mathrm{f}}^{\mathrm{L}}/n_{\mathrm{FakeCR}}^{\mathrm{L}}}\right). \tag{8.16}$$

where $n_{\mathrm{fakeCR}}^{\mathrm{H(L)}}$ is the number of the fake events in the fake control region. This term should be zero-consistent when the ABCD method ideally works. The formulation of $\mathcal{L}_{\mathrm{syst,fake}}$ is given as

$$\begin{aligned}\mathcal{L}_{\mathrm{syst,fake}}(\boldsymbol{n}^{\mathrm{H}}, \boldsymbol{n}^{\mathrm{L}}, r_{\mathrm{f}}) &= \mathcal{N}(r_{\mathrm{f}} \mid r_{\mathrm{f}}^{\mathrm{exp}}, \sigma^2_{r_{\mathrm{f}}}) \\ &\times \mathcal{P}\left(n_{\mathrm{FakeCR}}^{\mathrm{H,obs}} | n_{\mathrm{FakeCR}}^{\mathrm{H}}\right) \times \mathcal{P}\left(n_{\mathrm{FakeCR}}^{\mathrm{L,obs}} | n_{\mathrm{FakeCR}}^{\mathrm{L}}\right), \end{aligned} \tag{8.17}$$

As the probability density function of fake tracks, the polynomial function is used as described in Sec. 7.4. The high $E_{\mathrm{T}}^{\mathrm{miss}}$ signal region and the low $E_{\mathrm{T}}^{\mathrm{miss}}$ control region are fit simultaneously, so the correlation between parameters are automatically incorporated.

8.2 Hypothesis testing

In order to claim a discovery or to set exclusion limits, test statistic is defined as follows

$$\tilde{q}_0 = -2\ln\tilde{\lambda}(0) \qquad (\hat{\mu} \geq 0) \tag{8.18}$$

$$\tilde{q}_\mu = -2\ln\tilde{\lambda}(\mu) \quad (0 \leq \hat{\mu} \leq \mu) \tag{8.19}$$

$$\tilde{\lambda}(\mu) = \frac{\mathcal{L}(\mu, \hat{\hat{\boldsymbol{\theta}}}(\mu))}{\mathcal{L}(\hat{\mu}, \hat{\boldsymbol{\theta}})} \qquad (\hat{\mu} \geq 0), \tag{8.20}$$

where $\hat{\hat{\boldsymbol{\theta}}}$ is a $\boldsymbol{\theta}$ which maximises $\mathcal{L}$ for given μ. $\hat{\mu}$ and $\hat{\boldsymbol{\theta}}$ are μ and $\boldsymbol{\theta}$ which maximise $\mathcal{L}$, respectively. For the test of a discovery or an exclusion, the p-values, which is defined as cumulative distribution

$$p_0 \equiv \int_{\tilde{q}_0^{\mathrm{obs}}}^{\infty} f(\tilde{q}_0 \mid 0) d\tilde{q}_0 \tag{8.21}$$

$$p_\mu \equiv \int_{\tilde{q}_\mu^{\mathrm{obs}}}^{\infty} f(\tilde{q}_\mu \mid \mu) d\tilde{q}_\mu \tag{8.22}$$

are generally used. When p-values are less than the traditional threshold (e.g. 0.05 (95%), 1.3×10^{-3} (3-σ discovery), 2.9×10^{-7} (5-σ discovery)), one can claim the discovery or the exclusion.

For a limit setting, in order to avoid claiming a limit for which this analysis does not have sensitivity due to negative background fluctuations, this analysis uses CL_s [96] as defined

$$\mathrm{CL}_s(\mu) = \frac{p_{\mathrm{s+b}}}{1-p_{\mathrm{b}}} \tag{8.23}$$

$$\mathrm{CL}_{s+b}(\mu) = p_{\mathrm{s+b}} = \int_{\tilde{q}_\mu^{\mathrm{obs}}}^{\infty} f(\tilde{q}_\mu \mid \mu)\, d\tilde{q}_\mu \tag{8.24}$$

$$\mathrm{CL}_b(\mu) = 1-p_{\mathrm{b}} = \int_{\tilde{q}_\mu^{\mathrm{obs}}}^{\infty} f(\tilde{q}_\mu \mid 0)\, d\tilde{q}_\mu. \tag{8.25}$$

For the exclusion limit setting, 95% CL_s, where CL_s is less than 5%, is used. In order to minimise the calculation time of p-value, the calculation is done using asymptotic formulas [97], where it is assumed that the test statistic can be approximated to $\tilde{q}_\mu \approx \frac{\mu-\hat{\mu}}{\sigma^2}$ by Wald's theorem [98]. The parameters used in the approximation are determined using Asimov dataset which is constructed to satisfy all parameters set to be their expected values.

Chapter 9

Systematic uncertainties

There are three types of uncertainties: for common uncertainties affecting both signal and background processes, uncertainties relevant only for signal or background processes. As common systematic uncertainties, there are smearing-function-related uncertainties, which change the p_{T} templates. The smearing-function-related uncertainties are evaluated for each a particle. Signal systematic uncertainties are assessed as a normalisation uncertainty. As a background systematic uncertainty, an uncertainty of the method of the fake normalisation estimation is considered.

9.1 Common systematic uncertainty

Smearing function

Since the smearing function is directly measured from observed data, the MC simulation uncertainties are not necessary to be considered. However, a time dependence was observed as shown in Fig. 9.1. The maximum difference between all period and all p_{T} bins is assigned as the uncertainty. For muons, 7.3% and 17.1% are assigned for σ and α, respectively. For electrons, 8.5% and 21.2% are assigned for σ and α, respectively. For n parameter for electrons and pions, 100% uncertainties are assigned. For signals, the maximum difference between all period for the highest p_{T} bins, 6.32% and 10.1%, are assigned for σ and α, respectively.

9.2 Signal systematic uncertainty

In this section, signal-related uncertainties are discussed. Theoretical cross-section uncertainties are already discussed in Sec. 3.2.1.

Generator modelling

Since this analysis requires high p_{T} jets in the kinematical selection, a modelling of ISR jets affects the signal kinematical acceptance. In order to evaluate the generator uncertainties, the generator tunes in the event generation are varied, and

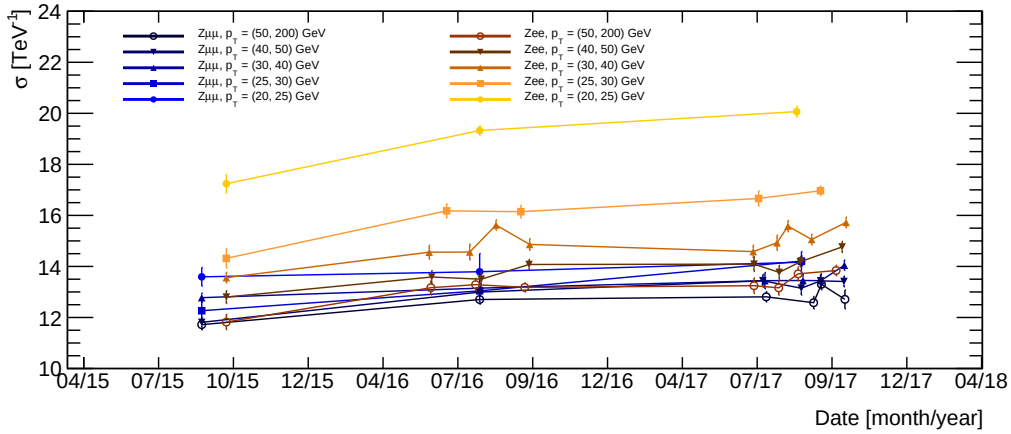

(a)

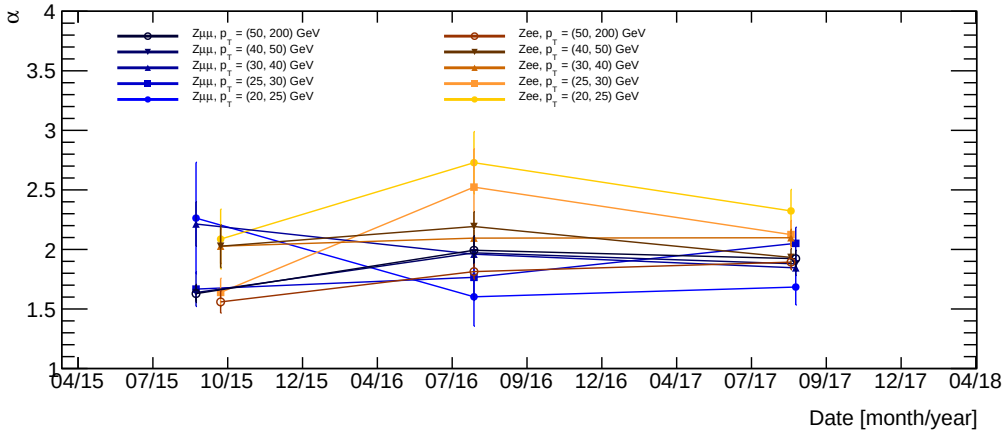

(b)

Figure 9.1: Time dependence of smearing function parameters, (a) σ and (b) α, observed from observed data for muons (labelled as $Z \to \mu\mu$) and for electrons (labelled as $Z \to ee$) separated in ranges of p_{T}. The resolution σ becomes worse as the integrated luminosity increases.

the change in the kinematical acceptance at the generator-level between samples are assigned to the uncertainty. Three variations are considered as follows

- Renormalisation scale and factorisation scale are varied by factors of 0.5 and 2.0 from the default ones ($M^2 + p_T^2$).
- CKKW-L merging scale [36,99], which determines the process (matrix-element or parton-shower) of additional partons, is varied by factors of 0.5 and 2.0 from the default one (1/4 of chargino mass).
- Parameters in the parton shower tuning [43] are varied by the uncertainties. Although there are five variation sets, only one set related to ISR α_s has a non-negligible effect.

Figure 9.2 shows the relative changes by variation as a function of chargino mass. Because the lifetime variation does not change the generator-level kinematical acceptance within the considered lifetime range, common uncertainties are used for all chargino lifetimes. Figure 9.2 (g) and (h) show combined systematic uncertainties from the event modelling in the event-generator. These uncertainties are assigned to each signal mass points.

Jet energy scale/resolution

Although jet energy scale and resolution are calibrated, there is a small discrepancy between data and MC simulation. The uncertainties of jet energy scale and resolution are sensitive to this analysis because of the use of high p_{T} jet to select signal events. The impact is evaluated by comparing the kinematical acceptance with varying jet performance by their uncertainties discussed in Ref. [77]. This analysis uses a strongly-reduced nuisance-parameter set, where several effects of parameters are combined, because of a negligible impact from the correlation between errors of the parameters. The impacts from the jet energy scale are 2–3%, and ones from jet energy resolution are less than 1%.

$E_{\mathrm{T}}^{\mathrm{miss}}$

$E_{\mathrm{T}}^{\mathrm{miss}}$ is reconstructed using all hard objects and the soft term as described in Sec. 4.6. Effects to $E_{\mathrm{T}}^{\mathrm{miss}}$ from the jet uncertainties are contained in the evaluation of jet energy scale and resolution uncertainties as discussed above. The uncertainties related to the soft term is evaluated by comparing the observed data to three different MC-generators as described in Ref. [89]. These effects on this analysis are evaluated by comparing the kinematical acceptance varying the uncertainties. The impact is less than 1%.

Trigger efficiency

Since trigger efficiency is directly evaluated from observed data, the only statistical uncertainty of the measurement is considered as the systematic uncertainty, and it is found to be negligible.

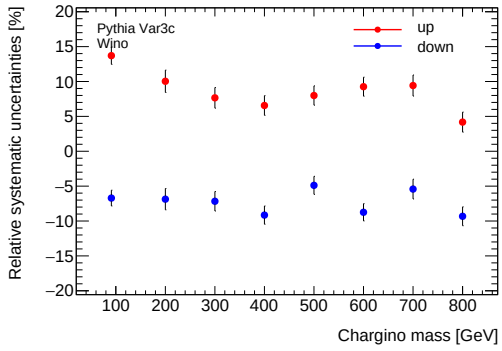

(a) ISR α_s (VAR3c)

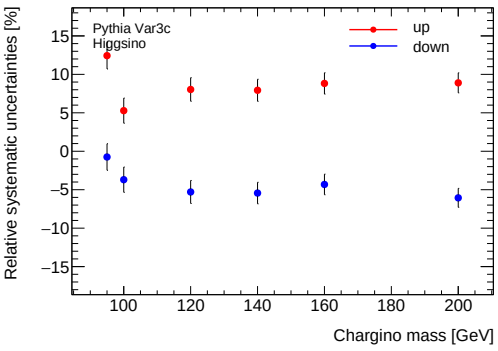

(b) ISR α_s (VAR3c)

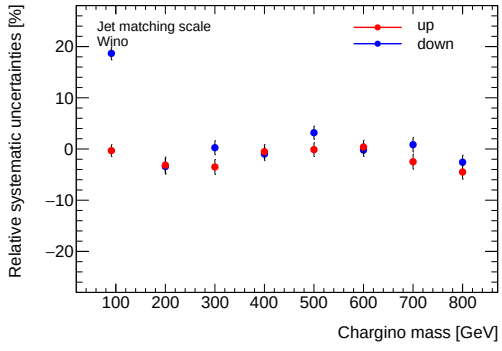

(c) CKKW-L merging scale

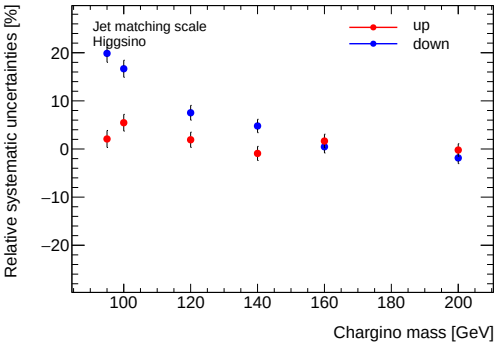

(d) CKKW-L merging scale

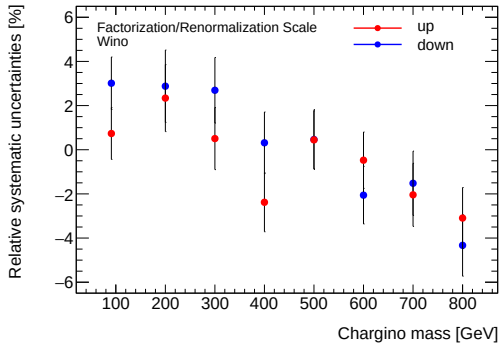

(e) R/F Scale

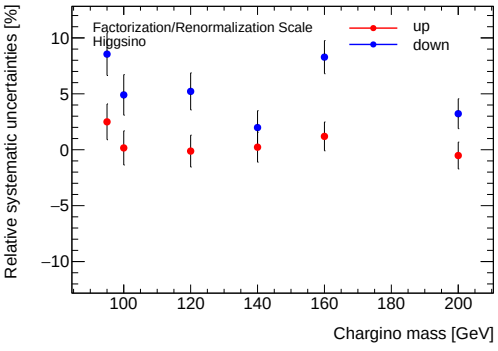

(f) R/F Scale

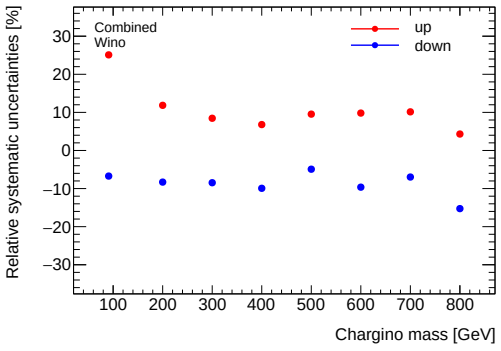

(g) Combined

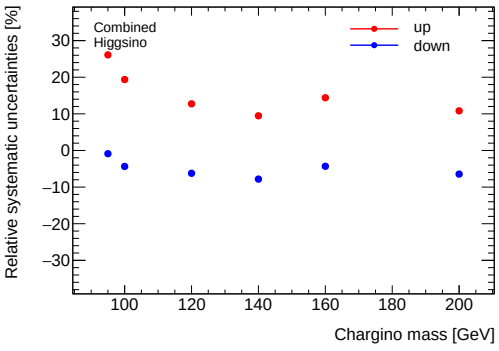

(h) Combined

Figure 9.2: Uncertainties related to the event modelling in the event-generator. (a) Pythia parton shower generator tuning for wino samples (b) Pythia parton shower generator tuning for higgsino samples (c) Jet merging scale for wino samples (d) Jet merging scale for higgsino samples (e) Factorisation/Renormalisation scale for wino samples (f) Factorisation/Renormalisation scale for higgsino samples (g) Combined uncertainties for wino samples (h) Combined uncertainties for higgsino samples

Pile-up

Pile-up distribution uncertainties are assigned to cover the discrepancy in the average interaction per bunch crossing ($\langle\mu\rangle$) between MC simulation and observed data derived from the visible cross-section measurements as shown in Fig. 9.3 (a), where the nominal variation corresponds to the scale-factor to match the Pile-up distribution in MC with observed data. The impact on the signal kinematical acceptance is less than 0.5%. On the other hand, the effect on the track reconstruction is higher as shown in Fig. 5.3, so the effects on the tracking efficiency from the $\langle\mu\rangle$ scale factor (μ_{SF}) uncertainties are also evaluated. Due to the smaller effects on the kinematical acceptance than the track reconstruction, the impacts are evaluated independently on the chargino mass and lifetime. Moreover, no kinematic selection is applied to increase statistics. Figure 9.3 (b) shows a tracklet reconstruction and selection efficiency as a function of decay radius with pile-up variations. The change in signal acceptance is less than 2.3%, which is assigned as the pile-up systematic uncertainty.

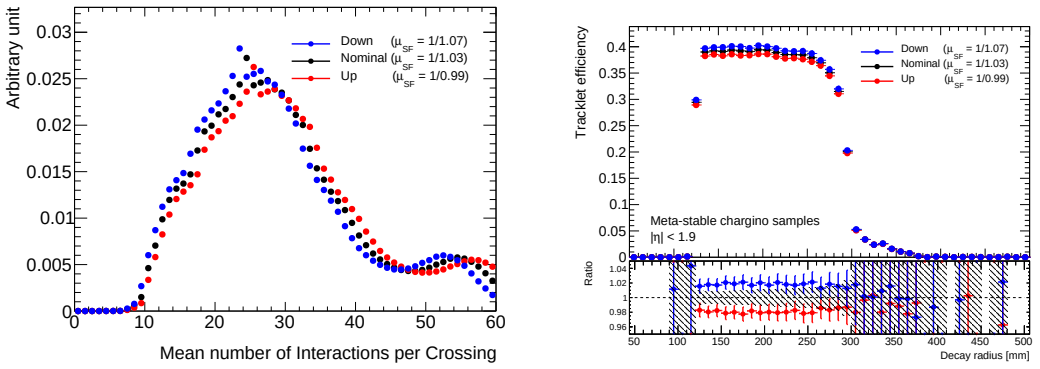

(a) (b)

Figure 9.3: Tracklet reconstruction and selection efficiency with pile-up variations.

Track reconstruction efficiency / selection efficiency

Since a detector modelling is not perfect, it is necessary to incorporate the possible difference in the tracking reconstruction and selection efficiency in observed data and MC simulation. The uncertainties in the track reconstruction efficiency and the selection efficiency are evaluated by comparing the tracklet in the observed data and MC simulation using artificial pixel tracklets in $Z \to \mu\mu$ events discussed in section 5.2.3. Figure 9.4 shows the comparison of tracklet reconstruction efficiency between the observed data and MC simulation. The maximum difference of 2.8%, is assigned to the reconstruction efficiency uncertainty. Figure 9.5 and Table 9.1 show a comparison of track selection efficiency at each selection criteria. The maximum effect comes from the isolation requirement, which comes from the mismodelling in the number of tracks. The maximum difference of 4.2 % is assigned to the track selection efficiency uncertainties.

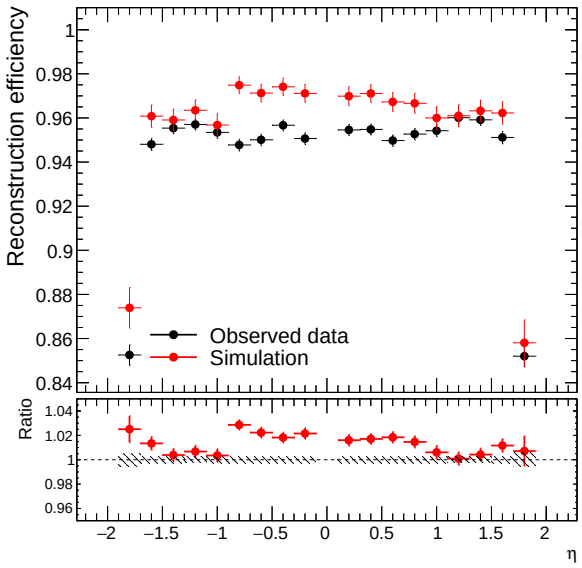

Figure 9.4: Data/MC comparison of reconstruction efficiency for muon tracks.

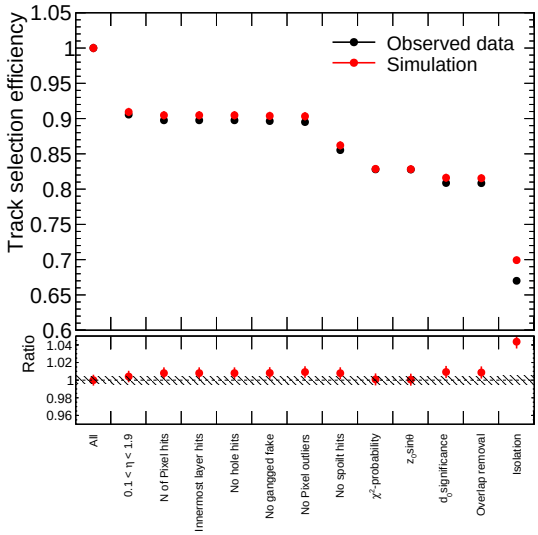

Figure 9.5: Data/MC comparison of selection efficiency for muon tracks.

selection	Data	MC
All	1	1
$0.1 < \eta < 1.9$	0.906	0.909
N of Pixel hits	0.898	0.905
Innermost layer hits	0.898	0.905
No hole hits	0.898	0.905
No ganged fake	0.896	0.904
No Pixel outliers	0.895	0.903
No spoilt hits	0.855	0.862
χ^2-probability	0.828	0.829
$z_0 \sin\theta$	0.828	0.828
d_0 significance	0.809	0.816
Overlap removal	0.808	0.815
Isolation	0.670	0.699

Table 9.1: Cut-flow of relative selection efficiency.

d_0 significance bias

A shift of transverse impact parameter is observed as shown in Fig. 9.6, where muon tracklets are extracted by the same selection used for the measurements of the smearing function discussed in section 5.2.4 except for the d_0 significance requirement. The mean value of d_0 significance is shifted from negative to positive at the first technical shutdown in 2016, and their bias is disappeared from 2017. The effects of this bias are summarised in Tables 9.2 and 9.3. This shift is observed in about half of the total luminosity. Therefore the half efficiency loss by a shift of the d_0 significance by 0.4 is subtracted from the total signal selection efficiency and the same uncertainty of the same amount is assigned.

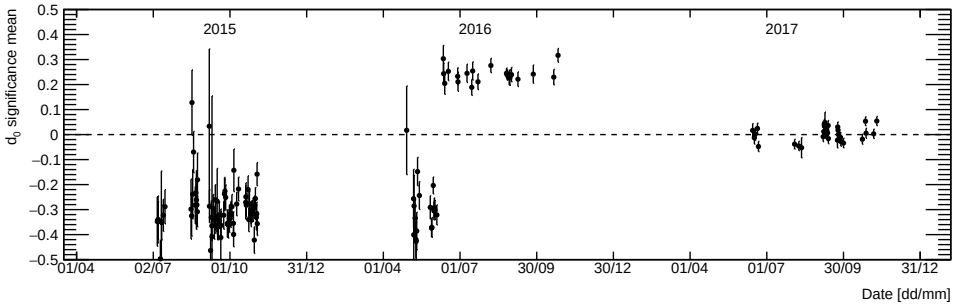

Figure 9.6: History of d_0 significance (d_0/σ_{d_0}) of pixel tracklets. A shift from a negative bias to positive bias in June 2016 corresponds to the first technical shutdown in 2016.

Mass (GeV)	91	200	300	400	500	600	700	800	900
Loss	-1.8%	-2.0%	-2.5%	-2.8%	-2.6%	-2.7%	-2.7%	-2.9%	-3.1%

Table 9.2: Signal selection loss by a shift of the d_0 significance by 0.4 for wino samples.

Mass (GeV)	95	100	120	140	160	200
Loss	-2.7%	-2.2%	-2.4%	-2.4%	-2.2%	-2.1%

Table 9.3: Signal selection loss by a shift of the d_0 significance by 0.4 for higgsino samples.

Integrated luminosity

As discussed in the section 3.1.1, 2.0% is assigned to the uncertainty of the integrated luminosity.

Tables 9.4 and 9.5 summarise all the considered uncertainties.

9.3 Background systematic uncertainty

This analysis relies on the data-driven method. Uncertainties in the object reconstruction are negligible compared to fitting uncertainties coming from the statistical uncer-

Source	Chargino mass (GeV) 91	200	300	400	500	600	700	800
(**Theoretical uncertainty**)								
Cross-section($\tilde{\chi}_1^+\tilde{\chi}_1^-$)	±2.6	±4.0	±4.9	±5.6	±6.3	±6.8	±7.3	±7.7
Cross-section($\tilde{\chi}_1^+\tilde{\chi}_1^0$)	±2.0	±3.4	±4.4	±5.4	±6.2	±6.8	±7.3	±7.7
Cross-section($\tilde{\chi}_1^-\tilde{\chi}_1^0$)	±4.1	±5.5	±6.3	±7.0	±7.6	±8.2	±8.9	±9.5
(**Uncertainties on the acceptance**)								
Scale+PS+PDF	$^{+25.1}_{-6.7}$	$^{+11.9}_{-8.3}$	$^{+8.5}_{-8.5}$	$^{+6.8}_{-9.9}$	$^{+9.5}_{-4.9}$	$^{+9.8}_{-9.6}$	$^{+10.1}_{-7.0}$	$^{+4.3}_{-15.3}$
JES	$^{+3.2}_{-3.1}$	$^{+2.6}_{-2.4}$	$^{+2.0}_{-1.8}$	$^{+1.8}_{-1.6}$	$^{+1.8}_{-2.0}$	$^{+1.4}_{-1.9}$	$^{+1.3}_{-0.9}$	$^{+1.4}_{-1.9}$
JER	$^{+0.8}_{-0.0}$	$^{+0.3}_{-0.0}$	$^{+0.2}_{-0.0}$	$^{+0.4}_{-0.0}$	$^{+0.1}_{-0.0}$	$^{+0.0}_{-0.2}$	$^{+0.0}_{-0.4}$	$^{+0.0}_{-0.2}$
TST	$^{+0.7}_{-1.1}$	$^{+0.4}_{-0.6}$	$^{+0.2}_{-0.4}$	$^{+0.2}_{-0.3}$	$^{+0.1}_{-0.2}$	$^{+0.2}_{-0.2}$	$^{+0.2}_{-0.2}$	$^{+0.1}_{-0.3}$
Trigger efficiency	$^{+0.0}_{-0.1}$	$^{+0.0}_{-0.1}$	$^{+0.0}_{-0.1}$	$^{+0.0}_{-0.2}$	$^{+0.0}_{-0.2}$	$^{+0.0}_{-0.2}$	$^{+0.0}_{-0.2}$	$^{+0.0}_{-0.3}$
Pile-up modeling				$^{+2.1\%}_{-2.3\%}$				
Tracklet reconstruction efficiency				±2.8%				
Signal selection efficiency				±4.2%				
d_0 bias	±0.9	±1.0	±1.3	±1.4	±1.3	±1.4	±1.4	±1.6
Luminosity				±2.0%				
Sub-total	$^{+26.0}_{-9.6}$	$^{+13.6}_{-10.5}$	$^{+10.6}_{-10.6}$	$^{+9.3}_{-11.7}$	$^{+11.4}_{-8.0}$	$^{+11.6}_{-11.5}$	$^{+11.8}_{-9.3}$	$^{+7.6}_{-16.6}$

Table 9.4: Summary of systematic uncertainties [%] in the expectation of signal events in wino case.

Source	Chargino mass (GeV) 95	100	120	140	160	200
(**Theoretical uncertainty**)						
Cross-section($\tilde{\chi}_1^+\tilde{\chi}_1^-$)	±2.9	±3.0	±3.2	±3.5	±3.7	±4.1
Cross-section($\tilde{\chi}_1^+\tilde{\chi}_1^0$)	±2.1	±2.2	±2.4	±2.7	±2.9	±3.4
Cross-section($\tilde{\chi}_1^-\tilde{\chi}_1^0$)	±4.2	±4.3	±4.6	±4.9	±5.1	±5.5
(**Uncertainties on the acceptance**)						
Scale+PS+PDF	$^{+26.1}_{-0.9}$	$^{+19.4}_{-4.4}$	$^{+12.7}_{-6.2}$	$^{+9.5}_{-7.8}$	$^{+14.4}_{-4.3}$	$^{+10.8}_{-6.5}$
JES	$^{+3.1}_{-3.6}$	$^{+2.9}_{-2.8}$	$^{+3.3}_{-2.6}$	$^{+2.9}_{-2.4}$	$^{+2.7}_{-2.2}$	$^{+2.1}_{-2.0}$
JER	$^{+0.0}_{-0.2}$	$^{+0.5}_{-0.0}$	$^{+0.5}_{-0.0}$	$^{+0.0}_{-0.0}$	$^{+0.4}_{-0.0}$	$^{+0.0}_{-0.1}$
TST	$^{+0.7}_{-1.3}$	$^{+0.7}_{-1.0}$	$^{+0.7}_{-0.8}$	$^{+0.5}_{-0.7}$	$^{+0.5}_{-0.0}$	$^{+0.3}_{-0.4}$
Trigger efficiency	$^{+0.0}_{-0.1}$	$^{+0.0}_{-0.1}$	$^{+0.0}_{-0.1}$	$^{+0.0}_{-0.1}$	$^{+0.0}_{-0.1}$	$^{+0.0}_{-0.1}$
Pile-up modeling			$^{+2.1\%}_{-2.3\%}$			
Tracklet reconstruction efficiency			±2.8%			
Signal selection efficiency			±4.2%			
d_0 bias	±1.4	±1.1	±1.2	±1.2	±1.1	±1.1
Luminosity			±2.0%			
Sub-total	$^{+27.0}_{-7.0}$	$^{+20.5}_{-0.8}$	$^{+14.5}_{-9.1}$	$^{+11.6}_{-10.2}$	$^{+15.8}_{-7.7}$	$^{+12.5}_{-9.1}$

Table 9.5: Summary of systematic uncertainties [%] in the expectation of signal events in higgsino case.

tainties in the background control regions. The uncertainties related to the number of lepton backgrounds in the signal region, the number of fake tracklets in the control region, p_{T} shape function of fake tracklets and smearing function are incorporated in the procedure for signal extraction.

Log ABCD ratio

The number of fake background events is estimated using the ABCD method, where it is assumed that a distribution of a d_0 significance of a fake tracklet is independent on the $E_{\mathrm{T}}^{\mathrm{miss}}$. The validity is evaluated by setting a pseudo signal region, where no signal remains, by using customised d_0 significance requirement, $2 < |d_0 \text{ significance}| < 5$, as shown in Fig. 9.7. Here hadron and muon templates estimated using normal d_0 significance requirements ($|d_0 \text{ significance}| < 1.5$) are used, and hadron template is substituted for the electron template. The fit is done without any ABCD ratio constraints. By the fitting, the evaluated value is $r_f = 0.29 \pm 0.41$. Since this is a consistent value with zero, the ABCD method is valid within the statistical uncertainties. This observed value is used as a constraint on r_f in the signal extraction.

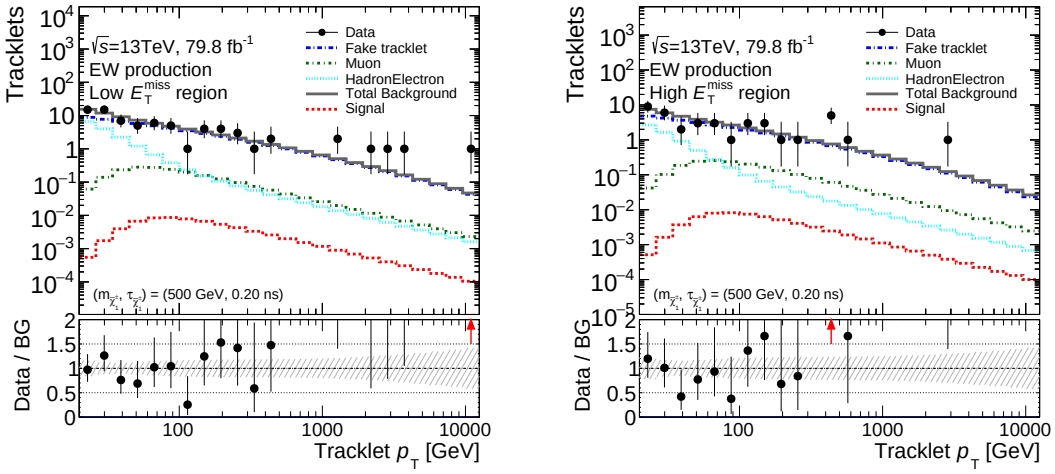

(a) (b)

Figure 9.7: Fit result using the tracklets with $2 < |d_0 \text{ significance}| < 5$. (a) Low $E_{\mathrm{T}}^{\mathrm{miss}}$ region (120 GeV $< E_{\mathrm{T}}^{\mathrm{miss}} <$ 200 GeV) (b) High $E_{\mathrm{T}}^{\mathrm{miss}}$ region (200 GeV $< E_{\mathrm{T}}^{\mathrm{miss}}$)

Chapter 10

Result

10.1 Shape fitting

A null-hypothesis test described in Sec. 8.2 is applied to the events which pass the event selection (Chapter 6) using p_{T} templates (Chapter 7) assuming only the Standard Model. Figure 10.1 show p_{T} distributions of observed tracklets with the expected signal and background p_{T} templates after the background-only fitting. Templates for the signals are not used in the fitting, but shown in the figures as setting signal strength (μ) to 1. Table 10.1 is a summary of fitting parameters. The parameters which are constrained in the control region are not changed significantly before and after the fitting, and the observed numbers of events in each a source are consistent with the expected number. A p-value for background-only hypothesis (p_0) for a wino model with the mass of 500 GeV and the lifetime of 0.2 ns is 0.36, and that for a higgsino model with the mass of 160 GeV and the lifetime of 0.04 ns is 0.37. There is no significant deviations from the SM prediction are found. Table 10.2 is a summary of background component in the high p_{T} ($p_{\mathrm{T}} > 100$ GeV) region. The observed number of high p_{T} tracklets are consistent with the expected numbers within the uncertainties. The number of the four background sources in the high p_{T} region are comparable to each other, and the fake background is dominant contribution.

The CL_s for an exclusion limit is calculated for a wino model with the mass of 500 GeV and the lifetime of 0.2 ns and a higgsino model with the mass of 160 GeV and the lifetime of 0.04 ns. The observed cross-section 95% CL_s upper limit for the wino model is 70 fb, and expected one is 69^{+29}_{-20} fb. The observed cross-section 95% CL_s upper limit for the higgsino model is 1.6 pb, and expected one is $1.6^{+0.7}_{-0.5}$ pb. A visible cross-section is defined as a signal yield in the signal region with normalised by the integrated luminosity. The observed visible cross-section 95% CL_s upper limit for the wino model is 0.18 fb, and expected one is $0.18^{+0.07}_{-0.05}$. The observed visible cross-section 95% CL_s upper limit for the higgsino model is 0.17 fb, and expected one is $0.17^{+0.08}_{-0.05}$.

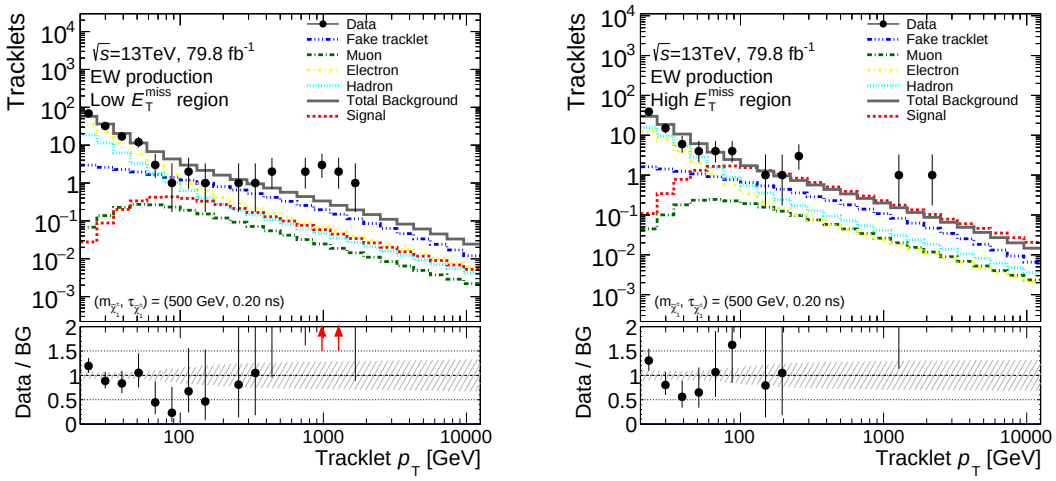

(a) (b)

Figure 10.1: The p_{T} distributions of the observed disappearing track candidates for (a) Low $E_{\mathrm{T}}^{\mathrm{miss}}$ selection and (b) High $E_{\mathrm{T}}^{\mathrm{miss}}$ selection are shown as black points. The coloured lines show the expected p_{T} distribution of signal (red, μ=1), fake background (blue), electron background (yellow), muon background (green), hadron background (light blue) and the total backgrounds (gray), which are determined by the background-only fitting. The signal strength (μ) is set to 1, but the signal template is not used in the fitting.

Source	Region	Without fit	With fit	Observed
Hadron	High MET	-	37.6 ± 11.2	
Electron	High MET	28.7 ± 5.9	28.9 ± 5.9	
Muon	High MET	1.9 ± 0.2	1.9 ± 0.2	
Fake	High MET	-	10.3 ± 5.8	
Total	High MET	-	78.7 ± 8.8	79
Hadron	Low MET	-	44.4 ± 23.1	
Electron	Low MET	82.1 ± 16.7	83.5 ± 16.8	
Muon	Low MET	2.1 ± 0.2	2.1 ± 0.2	
Fake	Low MET	-	18.8 ± 9.3	
Total	Low MET	-	148.8 ± 12.2	149
Fake	Fake CR, High MET	-	32.0 ± 5.8	32
Fake	Fake CR, Low MET	-	79.0 ± 8.8	79
p_0^{fake}		-	1.00 ± 0.24	
p_1^{fake}		-	0.071 ± 0.024	
r_{f}		0.29 ± 0.41	0.30 ± 0.37	
$\sigma_{\text{h}}^{\text{smearing}}$		0 ± 0.07	-0.01 ± 0.07	
$\alpha_{\text{h}}^{\text{smearing}}$		0 ± 0.17	0.03 ± 0.17	
$\nu_{\text{h}}^{\text{smearing}}$		0 ± 1.00	-0.20 ± 0.96	
$\sigma_{\mu}^{\text{smearing}}$		0 ± 0.07	-0.00 ± 0.07	
$\alpha_{\mu}^{\text{smearing}}$		0 ± 0.17	0.00 ± 0.17	
$\sigma_{\text{e}}^{\text{smearing}}$		0 ± 0.08	-0.09 ± 0.09	
$\alpha_{\text{e}}^{\text{smearing}}$		0 ± 0.21	-0.01 ± 0.23	
$\nu_{\text{e}}^{\text{smearing}}$		0 ± 1.00	-0.00 ± 1.00	

Table 10.1: The fitting parameters without and with the background-only fitting. The top 12 rows show the number of each background source, and other bottom rows show the parameters for the p_{T} templates. The expected numbers of the events are consistent with the observed events shown in the rightest column.

	Number (Fraction)	
Region	High $E_{\mathrm{T}}^{\mathrm{miss}}$	Low $E_{\mathrm{T}}^{\mathrm{miss}}$
Observed	7	15
Expected BG	7.0 ± 1.6	12.0 ± 2.6
Source		
Hadron	1.8 ± 0.6 (25.9 ± 11.3 %)	2.1 ± 1.1 (17.5 ± 11.1 %)
Electron	1.1 ± 0.2 (15.6 ± 5.0 %)	3.1 ± 0.6 (26.0 ± 7.9 %)
Muon	0.9 ± 0.1 (12.6 ± 3.2 %)	0.9 ± 0.1 (7.1 ± 1.8 %)
Fake	3.2 ± 1.8 (46.0 ± 16.3 %)	5.9 ± 3.0 (49.4 ± 15.2 %)

Table 10.2: The number of events having high p_{T} ($p_{\mathrm{T}} > 100$ GeV) tracklets and the fraction of the background sources. The observed numbers of events are consistent with the expected ones for both low and high $E_{\mathrm{T}}^{\mathrm{miss}}$ region.

10.2 Model-independent limit

The result in Sec. 10.1 depends on the given signal p_{T} distribution. This section shows a model-independent result. The observed number of events having the high p_{T} tracklet is compared to the expected number which is estimated by fitting with the background-only hypothesis with blinding of events having the high p_{T} tracklet in high $E_{\mathrm{T}}^{\mathrm{miss}}$ region. The blind threshold is set to 75 GeV, 100 GeV, 200 GeV and 300 GeV. The number of expected backgrounds, the number of observed events and p-value (p_0) are shown in Table 10.3. The discovery p-value (p_0) ranges from 0.11 to 1.00. There is no significant excess.

The 95% CL upper limit for a visible cross-section is also shown in Table 10.3. By using the visible cross-section, the exclusion limit for other BSM models predicting a disappearing track can be evaluated.

Threshold	75 GeV	100 GeV	200 GeV	300 GeV
Observed events	12	7	6	2
Expected BG	9.2 ± 2.0	6.9 ± 1.7	3.0 ± 0.8	2.3 ± 0.7
p_0	0.25	0.51	0.11	1.00
$\sigma_{\mathrm{vis}}^{95\%}$ [fb]	0.14	0.10	0.11	0.06

Table 10.3: The observed number of events in the high tracklet p_{T} and high $E_{\mathrm{T}}^{\mathrm{miss}}$ signal region and the expected number estimated by the fitting except for the high tracklet p_{T} and high $E_{\mathrm{T}}^{\mathrm{miss}}$ signal region. The model-independent discovery p-value (p_0) and the model-independent visible cross-section upper limit ($\sigma_{\mathrm{vis}}^{95\%}$) are shown for each tracklet p_{T} threshold.

Chapter 11

Discussion, interpretation and perspective

11.1 Interpretation

11.1.1 Constraints on the long-lived wino models

Exclusion limits for a wino LSP model with signal strength ($\mu_{\rm sig}$) of unity are evaluated as a function of chargino mass and chargino lifetime. As discussed in Chapter 8, the yield and the $p_{\rm T}$ shape of signal events are evaluated using MC simulation for each mass point with the lifetime re-weighting technique (Eq. 3.2). Figure 11.1 (a) shows an expected number of signal events in the signal region as a function of the chargino mass and chargino lifetime. Figure 11.1 (b) shows a signal acceptance $\times$ efficiency as a function of the chargino mass and chargino lifetime. Signals with their lifetime of 1 ns have higher acceptance $\times$ efficiency than others because the pixel tracklets are sensitive to the signals decaying between the fourth Pixel-layers (r = 123 mm) and the first SCT-layers (r = 299 mm), corresponding to the $c\tau$ of 0.4 ns to 1.0 ns. Figure 11.2 (a) shows exclusion limits at 95% CLs in the chargino mass and lifetime plane. The upper exclusion limit for the predicted lifetime is set at 490 GeV by this analysis. This analysis has low sensitivity for very short lifetimes ($<$ 0.02 ns) and long lifetimes ($>$ 0.85 ns) compared to the LEP results and the ATLAS/CMS previous results, respectively, because of the difference of the track length. This analysis is the most sensitive for model-favoured lifetime of 0.2 ns. Figure 11.2 (b) shows exclusion limits in the chargino mass and mass splitting plane. The mass splitting is computed using a relation between the wino mass splitting and lifetime described in Sec. 1.6.2. This analysis has better sensitivity than LEP for the mass splitting smaller than 290 MeV.

Figure 11.3 (a) and (b) show constraints for AMSB parameters with $\tan\beta = 5$ and 10, respectively. The relation between the wino mass and AMSB parameters are calculated using SOFTSUSY 4.1.5. The Higgs mass is also calculated using SOFTSUSY without three–loop correction. This analysis excludes $m_{3/2}$ up to 150 TeV, and some parameters are satisfied with observed Higgs mass.

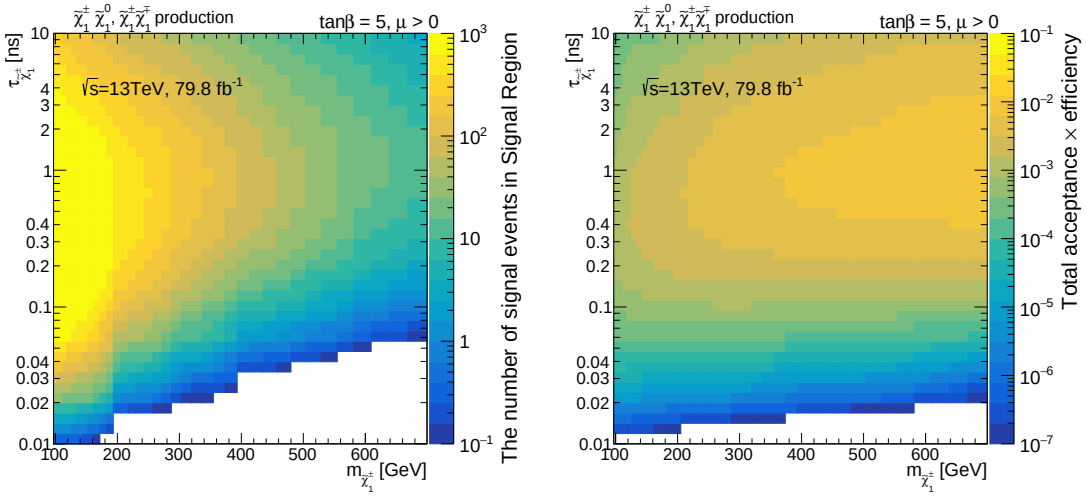

(a) (b)

Figure 11.1: (a) The number of signal events in the signal region (b) The signal acceptance × efficiency as a function of chargino mass and chargino lifetime.

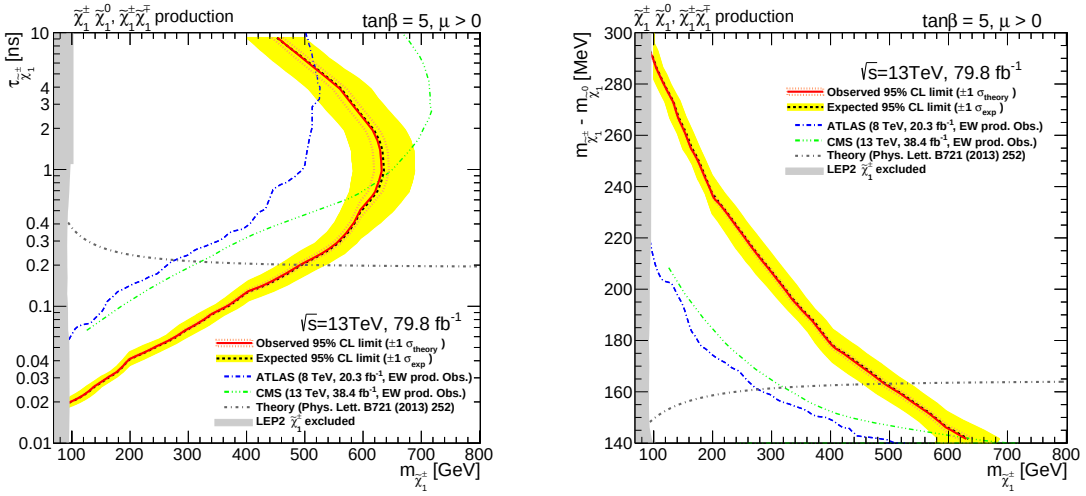

(a) (b)

Figure 11.2: Exclusion limit on (a) the chargino mass and the chargino lifetime (b) the chargino mass and mass splitting between the chargino and the neutralino. Observed exclusion limit is shown as a red curve. The dotted orange line around observed limits shows the cross-section uncertainties discussed in Sec. 3.2.1. The expected sensitivity is shown as a black dotted line, and the 1 sigma fluctuation is represented as a yellow band. Grey chained line in (a) ((b)) shows a relation between wino mass and wino lifetime (mass splitting) calculated with up to two–loop. LEP (Ref. [100]), ATLAS (Ref. [20]) and CMS results (Ref. [21]) are shown as a grey band, a blue line and a green line, respectively.

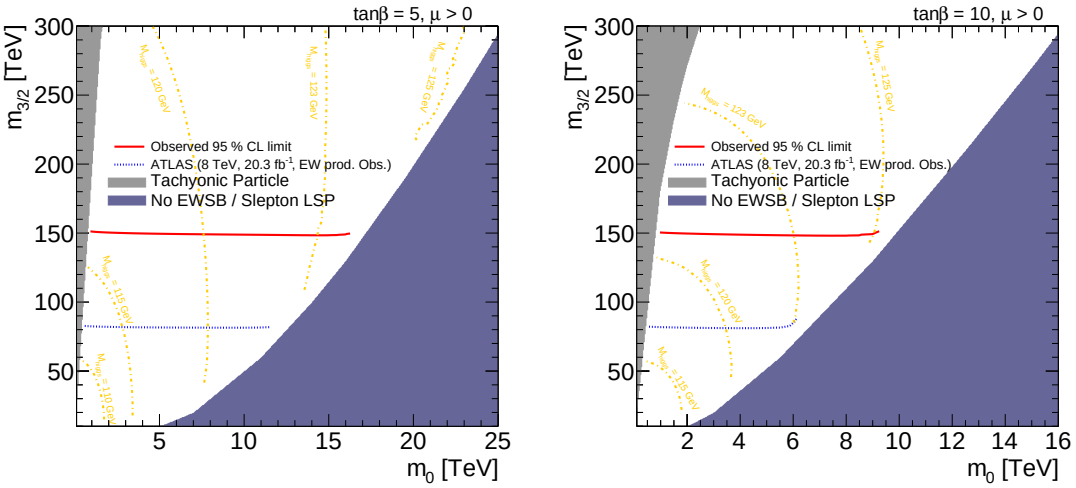

(a) $\tan\beta = 5$ (b) $\tan\beta = 10$

Figure 11.3: Constraints in the $m_{3/2} - m_0$ plane. New constraint from this analysis is represented by the red line. Blue line is ATLAS Run 1 results (Ref. [20]). Small m_0 and large $m_{3/2}$ regions are forbidden due to the existence of tachyonic particles. Large m_0 and small $m_{3/2}$ regions are forbidden due to slepton LSP or no electroweak symmetry breaking. Orange chains show a contour of the Higgs mass. The exclusion lines near the boundaries on the forbidden regions are not plotted due to the difficulties of the extrapolation.

In the pure gravity mediation model, the gluino can be light enough to be detected in LHC experiments. Figure 11.4 shows constraints on the gluino and chargino masses. In the case of AMSB-like (L=0), the gluino is too heavy to be produced in the LHC. On the other hand, there are some viable parameter regions where gluino is light to be produced in the LHC. As shown in this figure, inclusive gluino search with hadronic jets in the final states (Ref. [101]) is more sensitive than this analysis when L equals to about 1.

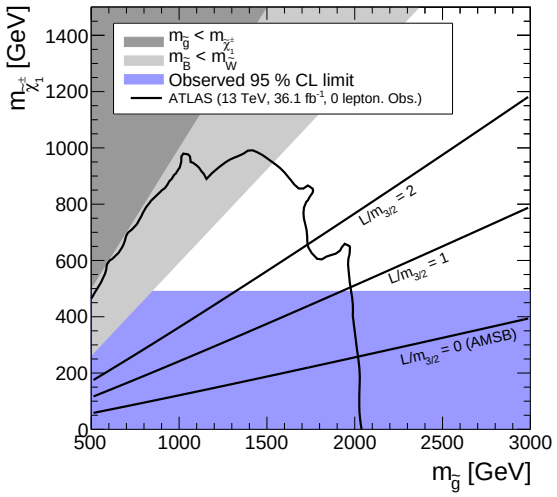

Figure 11.4: Constraints on the gluino mass – chargino mass plane. Excluded parameters are shown as blue shade. A result in zero lepton analysis (Ref. [101]) is shown as a black line. Dark grey and light grey shade represent model-disfavour regions where the gluino mass is lighter than the chargino mass and where the bino mass is lighter than wino mass, respectively. The black lines represent a relation between gluino mass and chargino mass with different L parameters in the pure gravity mediation model, where the relation (Eqs. 1.10–1.13) is used.

11.1.2 Constraints on the long-lived higgsino models

Figure 11.5 (a) and (b) show the exclusion limits for higgsino models. This analysis excludes the higgsino masses up to 170 GeV for the predicted lifetime. It is more sensitive than LEP for the mass splitting smaller than 330 MeV.

Figure 11.6 shows constraints on higgsino mass and bino and wino masses in the MSSM. Here mass splitting between the lightest chargino and the lightest neutralino is computed using the radiative correction and chargino/neutralino mixing. For a simple setup, bino mass and wino mass are assigned to common mass. For a light bino and wino mass case, this analysis has a higher exclusion sensitivity than LEP for bino/wino mass larger than 40 TeV. For a lighter bino and wino case, this analysis is not sensitive for higgsinos.

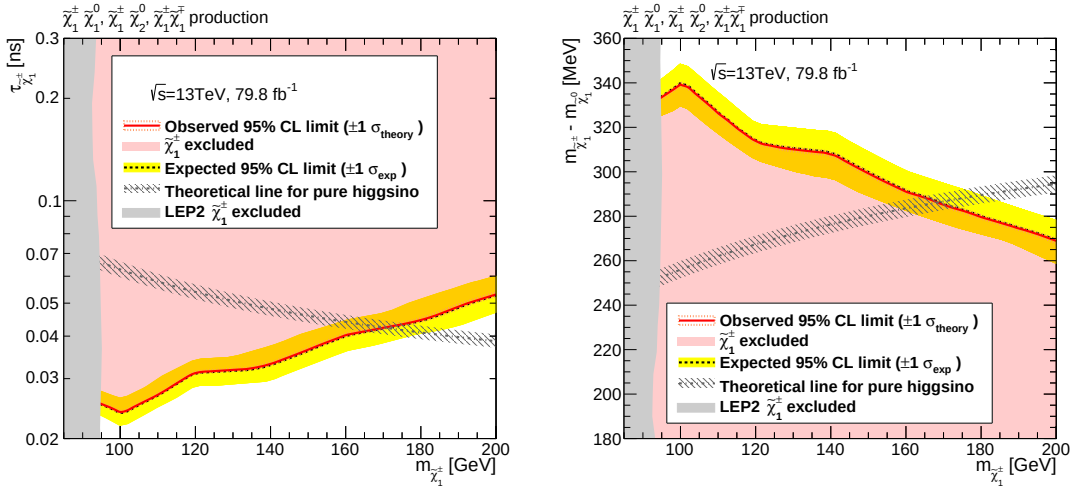

(a) (b)

Figure 11.5: Constraints of higgsino models on (a) chargino mass and chargino lifetime (b) chargino mass and mass splitting between chargino and neutralino. Observed exclusion limit is shown as a red curve, and a red-shaded region represents excluded parameters. The dotted orange line around observed limits shows the cross-section uncertainties discussed in Sec. 3.2.1. The expected sensitivity is shown as a black dotted line, and the 1 sigma fluctuation is represented as a yellow band. Grey chained line in (a) ((b)) shows a relation between higgsino mass and higgsino lifetime (mass splitting) calculated with up to one–loop, where naive systematics uncertainty for higgsino theory ($\Delta_{2-\mathrm{loop}}\delta m = (\frac{\alpha^2}{4\pi})^2 \pi m_t \sim 3.9$MeV) is assigned as a gray hatch. LEP result [100] is shown as a grey band.

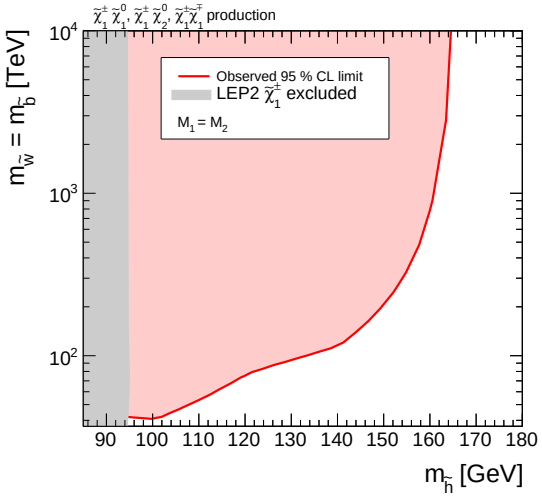

Figure 11.6: Constraints on the higgsino mass – bino/wino mass plane. Excluded parameters are shown as a red-shaded region. LEP result [100] is shown as a grey band.

11.2 Future experiments

In case the energy or the luminosity of the LHC is not sufficient to discover new physics, more powerful collider would be needed. This section focuses on future hadron colliders.

11.2.1 High-Luminosity Large Hadron Collider

After the Run 3, where 300 fb^{-1} of data will be collected, the LHC is planned to be upgraded for high luminosity run, which is called High-Luminosity LHC (HL-LHC). The HL-LHC will deliver 3000 fb^{-1} of collisions in 10 years, and the high luminosity experiments will be run with a higher pile-up of 200. In parallel to the upgrade of the LHC machine, the ATLAS detector will be upgraded to be tolerant to the harsh pile-up condition. Especially, the inner tracker will be replaced because high radiation would cause serious damage to the performance of the inner tracker located at the nearest position to the beam pipe. The new tracker, called "Inner Tracker" (ITk) [102], is shown in Fig. 11.7. All sub-detectors consist of silicon sensors, and the position of layers is very much different from the current layout Fig. 2.2.

The discovery potential of winos/higgsinos is evaluated assuming the latest ITk layout, the centre of mass energy of 14 TeV, $\mu = 200$ and the integrated luminosity of 3000 fb^{-1} [103]. The analysis strategy follows the ATLAS Run 2 analysis. The strategy of a kinematic selection is the same with the current analysis: no lepton, large $E_{\mathrm{T}}^{\mathrm{miss}}$, high p_{T} jet and large $\Delta\phi$(jets,$E_{\mathrm{T}}^{\mathrm{miss}}$). The thresholds are optimised to maximise a discovery sensitivity at the 3000 fb^{-1}. The short tracks, which has at least four hits, are used as well as the Run 2 analysis.

The kinematic properties of both the signal charginos and the SM processes are

evaluated using the generator-level variables, then smearing them by the parametrised detector functions [104]. The signal tracking acceptance and the tracklet background rate are evaluated by GEANT4 simulation and the track reconstruction algorithm based on the current ATLAS algorithm as discussed in Sec. 4.1 with a tune of a configuration.

Figure 11.8 shows the signal track reconstruction efficiencies with the ITk layout and the current ATLAS layout, respectively. The fourth layer of the ITk is located farther than the current ATLAS fourth layer, resulting in lower signal acceptance than the current ATLAS tracker. On the other hand, the reconstruction efficiency at the maximum point is better than the Run 2 because of a lower rate of the assignment of wrong hits thanks to the sensor pitches and the layout. Tracklet p_{T} resolution is also evaluated with the GEANT4 simulation, and is applied to the generator-level chargino p_{T}.

The expected number of backgrounds is evaluated based on the estimated yields of background components in an ATLAS analysis (Ref. [105]). The number of scattered-background is obtained with scaling the ATLAS results by the ratio of material budget. The number of fake backgrounds is obtained with scaling the ATLAS result by the ratio of the number of tracks in the fake dominant region. Since the number of fake tracks exponentially increases as a function of the number of hits, the fake track events dominate the background in the HL-LHC.

Figure 11.9 shows a discovery sensitivity for the wino LSP scenario and the higgsino LSP scenario. The HL-LHC has the potential to access the wino for up to about 850 GeV and the higgsino up to about 250 GeV.

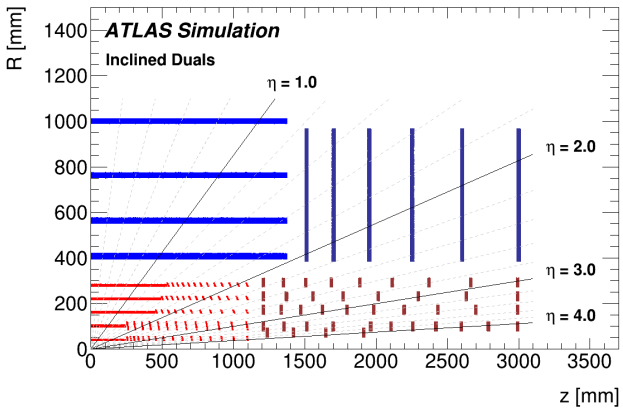

Figure 11.7: Illustration of the ITk layout [102]. Pixel sensors are shown as red lines. Strip sensors are shown as blue lines.

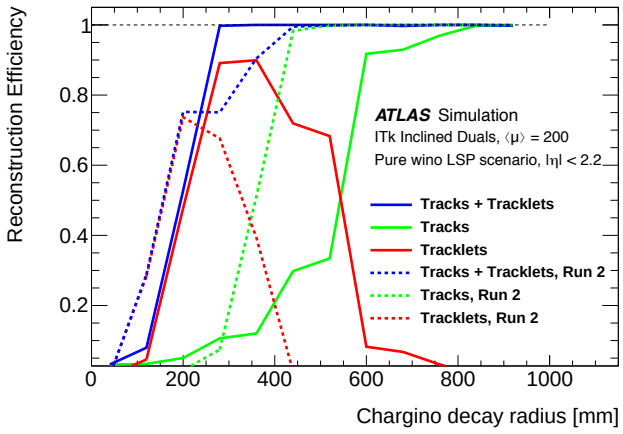

Figure 11.8: A signal reconstruction efficiency as a function of the chargino decay radius [102]. Solid lines are ones for the ITk. Dotted lines are ones for the current ATLAS layout. Red lines show pixel tracklets.

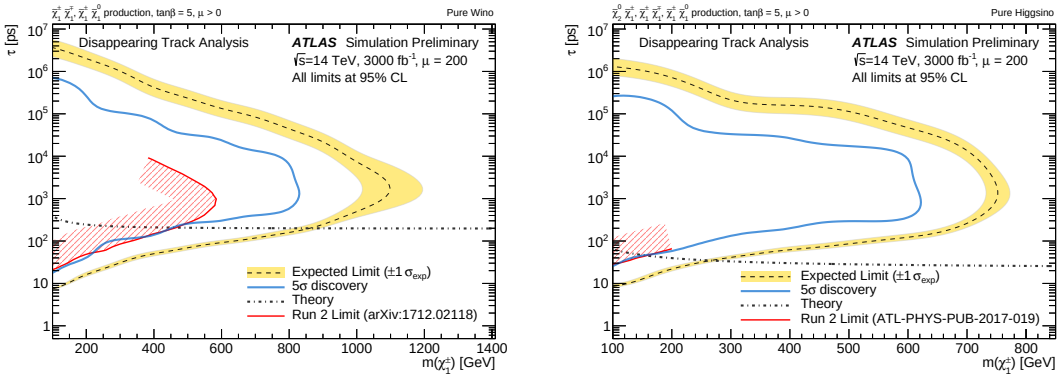

(a) (b)

Figure 11.9: Expected sensitivities with the ITk layouts with 3000 fb^{-1} [103] (a) for pure wino (b) for pure higgsino. Yellow bands show the exclusion limits at the HL-LHC. Blue lines show the discovery limits at the HL-LHC. Red regions show the ATLAS Run 2 exclusion limits with 36.1 fb^{-1}.

11.2.2 Future Circular Collider

CERN is considering the construction of a next-generation collider, the so-called Future Circular Collider (FCC) [106]. FCC would be constructed near the LHC, and the tunnel is designed to have 100 km circumference. The FCC could have three operating modes. FCC-ee is an electron-positron collider and would be operated at the centre of mass energy of 91 GeV to 365 GeV. The main aim of the FCC-ee is precision measurements of the Standard Model. The FCC-ee would produce huge numbers of Z bosons, WW pairs, Higgs bosons and $t\bar{t}$ pairs depending on the centre of mass energy. FCC-hh is a hadron collider like the LHC and would be operated at the centre of mass energy of 100 TeV with 16 T bending magnets. The FCC-hh program can access new physics at O(10) TeV. FCC-eh is an electron-proton collider and would be operated with a 50 TeV proton beam and a 60 GeV electron beam. The FCC-eh can measure the quark/gluon structure in proton with great accuracy.

From the view of WIMP dark matter, the FCC-hh has the highest sensitivity among three options, the discovery potential is therefore evaluated [107]. Figure 11.10 (a) shows the number of signal chargino decays and the reference FCC-hh inner tracker in the conceptual design report [106]. In this study, an optimised layout is also considered as shown in Fig. 11.10 (b), which has an additional silicon layer and the positions of the inner five layers are optimised.

The signal acceptance is evaluated assuming that all signal tracks can be reconstructed if the signal chargino passes through at least five silicon layers in the tracker. The backgrounds from the scattered-sources are evaluated by scaling the ATLAS Run 2 result by the ratio of material budget. The fake background is evaluated using GEANT4 simulation and a simple tracking algorithm as described in Ref. [107]. Pile-up collisions are produced by PYTHIA with two different models of soft QCD processes: only non-diffractive processes and a mixture of diffractive and non-diffractive processes. Since the fake rate depends on η as shown in Fig. 11.11 (a), tracks with small η ($|\eta| < 1$) are used in this study. The fake rate strongly depends on the pile-up, the QCD process and the number of hits in the track as shown in Fig. 11.11 (b). In order to suppress the fake tracklet rate, this analysis requires at least five hits for all tracks, which is a different condition from the ATLAS analysis.

Recently, the fast timing silicon detectors are being developed. Such detectors can measure the particles arrival time with O(10) ps. Since fake tracks are formed from uncorrelated hits, e.g. originating from different collision points, the relation of the timing between the hits in the track is not consistent to be a track originating from a single particle. About 96% of fake tracks can be removed by checking the hit time assuming 50 ps time resolution at each pixel sensor.

The strategy of the kinematic selection is the same with Run 2 analysis: no lepton, high p_{T} jet and large $E_{\mathrm{T}}^{\mathrm{miss}}$. A kinematic selection is optimised for 3 TeV wino and 1 TeV higgsino assuming the integrated luminosity of 3 ab^{-1}. Figure 11.12 shows a discovery sensitivity in the FCC-hh. The difference between the soft QCD processes in pile-up collisions is assigned to uncertainties as represented as error bands. The sensitivities strongly depend on the tracker layout. The FCC-hh with the optimised tracker layout

has potential to discover charginos with masses predicted from the relic density of dark matter.

The time measurements can determine the velocity, and mass ($m = \frac{p}{\beta\gamma}$). So after the discovery of the new particles, this could determine the mass and the model parameters, that is discussed in the article [108].

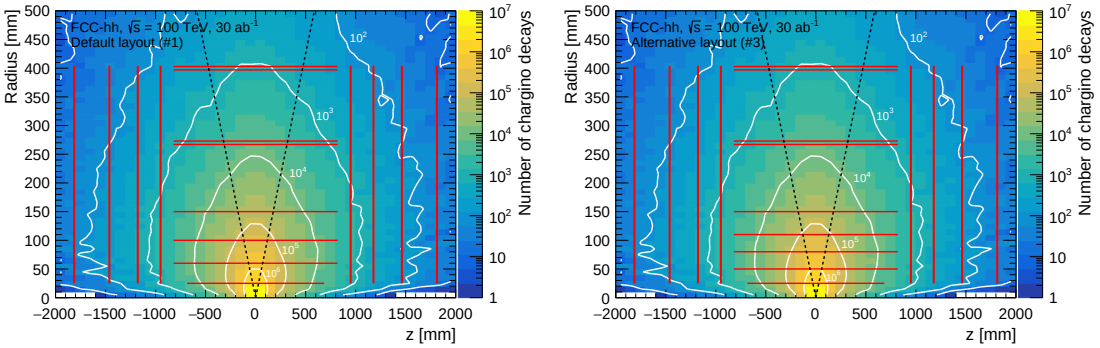

(a) (b)

Figure 11.10: (a) Reference layout in the FCC conceptual design report. (b) Optimised layout for disappearing track analysis. Red lines show positions of silicon detectors. The dotted black lines correspond to $|\eta| = 1$.

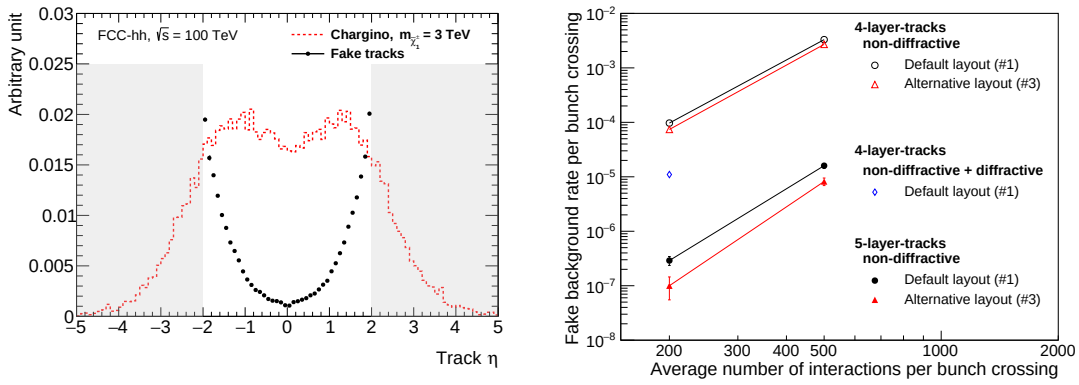

(a) (b)

Figure 11.11: (a) Fake track rate as a function of η. Black points show fake track rate. (b) Fake track rate as a function of pileup. Black circles show a fake rate using default layout (Fig. 11.10 (a)). Red triangles show a fake rate using optimised layout (Fig. 11.10 (b)). The blue diamond shows a fake rate estimated including diffractive process. The open symbols represent a fake rate usinig four-layer-tracks. The filled symbols represent a fake rate usinig five-layer-tracks.

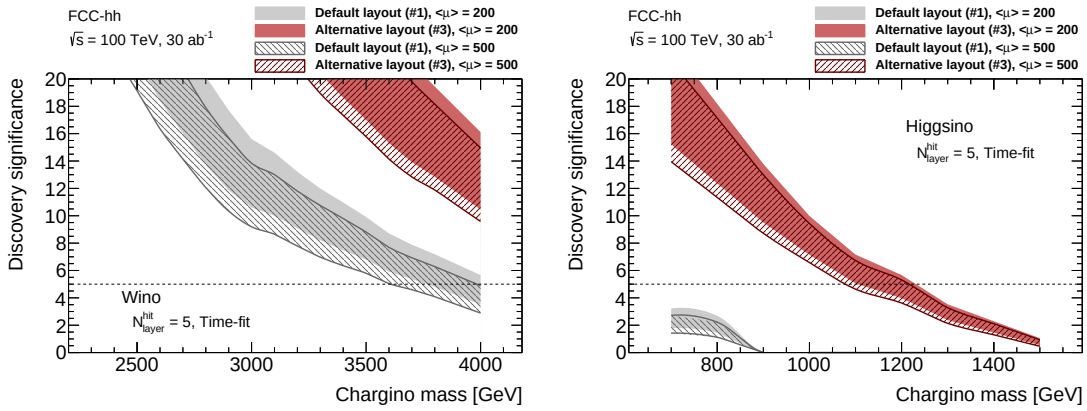

(a) (b)

Figure 11.12: Discovery sensitivities (a) for pure winos (b) for pure higgsinos. Black graphs show the sensitivities using default layout. Red graphs show the one using optimised layout. Solid one is for $\mu = 200$, and hatched one is for $\mu = 500$.

Chapter 12

Conclusion

This thesis presents a search for heavy meta-stable charged particles at a centre of mass energy of 13 TeV. Such new particles are predicted from well-motivated models in the supersymmetric theory, while their typical lifetimes (0.2 ns and 0.04 ns) are too short to reconstruct with conventional tracking techniques in the ATLAS experiment. The introduction of pixel-tracklets, which are quite short, makes it possible to access such charginos.

The analysis is designed to maximise the signal acceptance of short-lived charginos by using the pixel-tracklets. Focusing on the direct chargino and neutralino pair production makes the search inclusive, namely independent of heavier supersymmetric particles. The properties of short tracks are measured from mostly observed data. The background estimation is based on the p_{T} spectrum fitting; templates used in the fit are derived from observed data.

This analysis uses the data recorded by the ATLAS detector in 2015–2017 with an integrated luminosity of 80 fb^{-1}. No significant excess from the Standard Model prediction is found in the signal enhanced region. This result gives a new constraint for new particles: 490 GeV for the pure-wino LSP model and 170 GeV for the pure-higgsino LSP model.

There is still room to allow the existence of the heavier charginos because wino (higgsino) mass up to 3 (1) TeV is motivated from the observed value of the dark-matter relic density. Next-generation colliders, the High-Luminosity LHC and the Future Circular Collider, have potential to discover such charginos.

Acknowledgements

First of all, I would like to thank my supervisor, Prof. Shoji Asai, for his suggestion for a subject and a direction of my research in more than five years. I learnt the mind of a scientist from his attitude, passion and deep knowledge into physics. My first step as a researcher could not be productive without his advice and help.

I am also grateful to Prof. Ryu Sawada for his support of my research. I could not smoothly proceed with my research in the collaboration without his great assistance. His deep understanding of a physics analysis and software always guided me to better solutions.

I would like to thank Prof. Junichi Tanaka and Prof. Koji Terashi. A discussion about future perspectives and technologies on this field excited and motivated me. I'm looking forward to expanding these studies more in the near future.

I would like to thank Prof. Takashi Yamanaka and Prof. Shimpei Yamamoto for their supports in my early stage. They supported me in my early career, especially during the master course. Their support formed the basis of this research and indicated the direction to the current position.

I am grateful to all the professors and staffs, Prof. Masaya Ishino, Prof. Yasuyuki Okumura, Prof. Yuji Enari, Prof. Tatsuya Masubuchi, Prof. Tomoyuki Saito and Prof. Takuya Nobe, for all their support. Discussions in weekly meetings and much chat in a coffee break were suggestive and productive. I was very impressed by their hard work and vitality.

I am grateful to my colleagues at the University of Tokyo and ATLAS-Japan. Without them, I could not have such a fruitful life in these five years and a special stay in CERN.

Lastly, I would like to express my deepest gratitude for my family.

Appendix A

Tracklet q/p_T distribution and a smearing function

$\Delta q/p_T$ distributions of MC simulation samples for a electron, a muon and a pion are shown in Fig. A.1 for each p_{T} slices. A tracklet originating from a low p_{T} electron has poor resolution than others due to the small mass. A tracklet originating from a high p_{T} electron and a chargino has good resolution than others. Since these particle leave a large energy deposit to each pixel sensor, the hit position can be measured more precisely. This effect is not observed in observed data as shown in Fig. A.2 because an other effect, e.g. misalignment, dominantly contributes to the resolution.

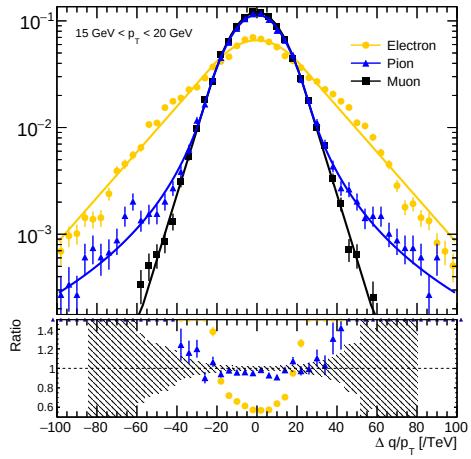

(a)

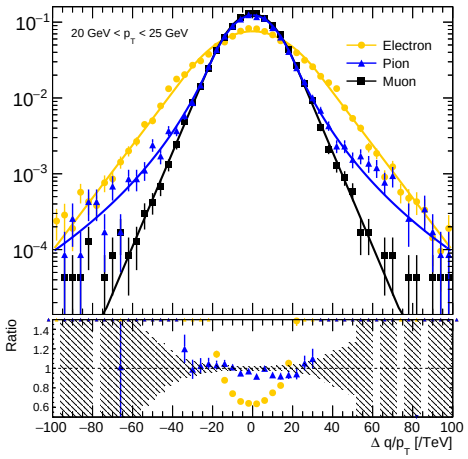

(b)

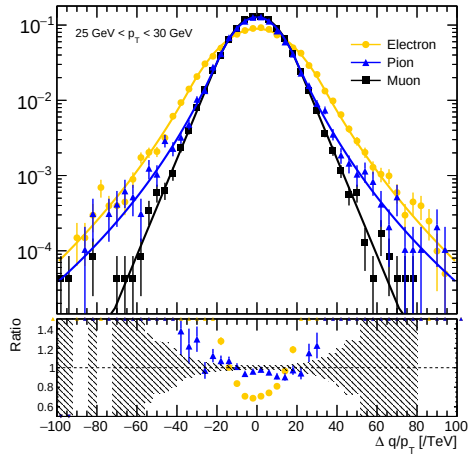

(c)

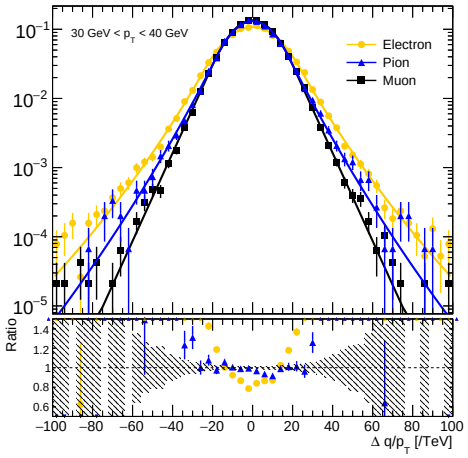

(d)

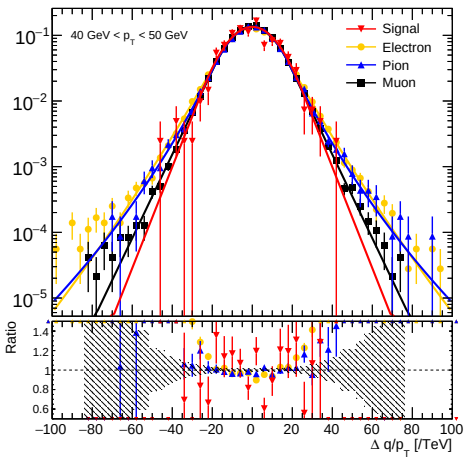

(e)

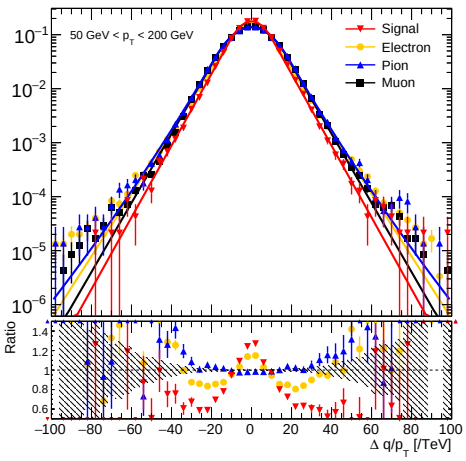

(f)

Figure A.1: $\Delta q/p_T$ distribution for MC simulated samples with fit functions for particle p_{T} slices: (a) 15 GeV $< p_{\mathrm{T}} <$ 20 GeV (b) 20 GeV $< p_{\mathrm{T}} <$ 25 GeV (c) 25 GeV $< p_{\mathrm{T}} <$ 30 GeV (d) 30 GeV $< p_{\mathrm{T}} <$ 40 GeV (e) 40 GeV $< p_{\mathrm{T}} <$ 50 GeV (f) 50 GeV $< p_{\mathrm{T}} <$ 200 GeV. A black square shows a muon. A blue triangle shows a pion. A yellow circle shows a electron. A red triangle shows a charginos.

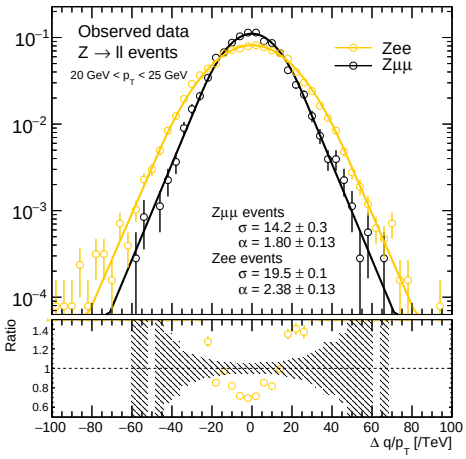

(a)

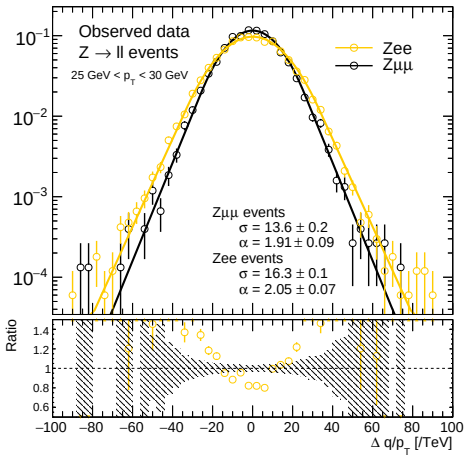

(b)

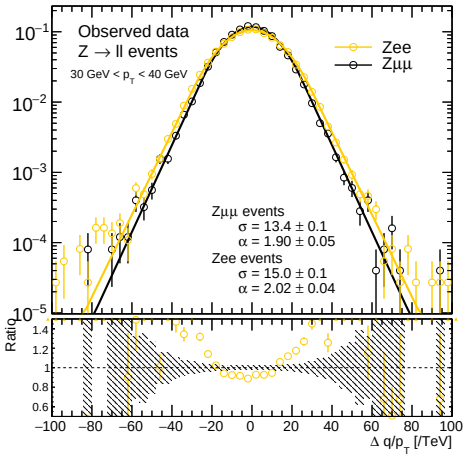

(c)

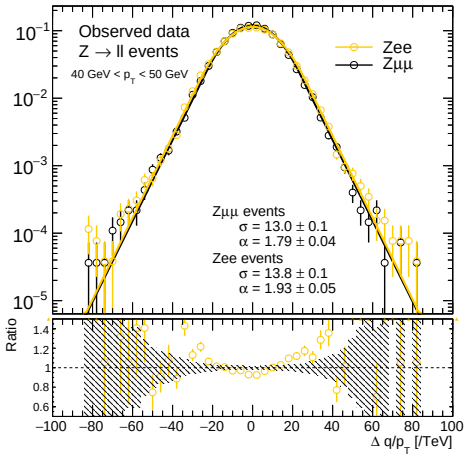

(d)

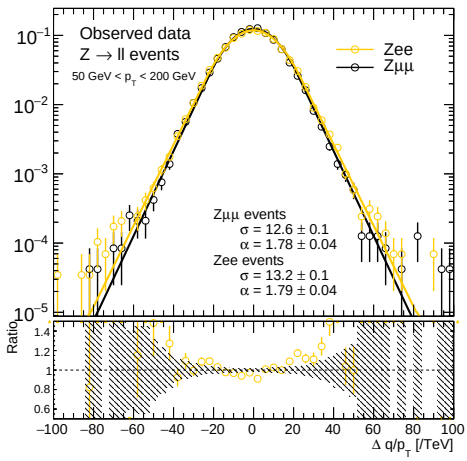

(e)

Figure A.2: $\Delta q/p_T$ distribution for observed data with fit functions for particle p_{T} slices: (a) 20 GeV $< p_{\mathrm{T}} <$ 25 GeV (b) 25 GeV $< p_{\mathrm{T}} <$ 30 GeV (c) 30 GeV $< p_{\mathrm{T}} <$ 40 GeV (d) 40 GeV $< p_{\mathrm{T}} <$ 50 GeV (e) 50 GeV $< p_{\mathrm{T}} <$ 200 GeV. A black circle shows a $Z \to \mu\mu$ process. A yellow circle shows a $Z \to ee$ process.

Bibliography

[1] ATLAS Collaboration, *Observation of a new particle in the search for the Standard Model Higgs boson with the ATLAS detector at the LHC*, *Phys. Lett. B* **716** (2012) 1 [1207.7214].

[2] CMS Collaboration, *Observation of a new boson at a mass of 125 GeV with the CMS experiment at the LHC*, *Phys. Lett. B* **716** (2012) 30 [1207.7235].

[3] S. P. Martin, *A Supersymmetry primer*, hep-ph/9709356.

[4] K. Abe, Y. Haga, Y. Hayato, M. Ikeda, K. Iyogi, J. Kameda et al., *Search for proton decay via $p \to e^+\pi^0$ and $p \to \mu^+\pi^0$ in 0.31 megaton$\cdot$years exposure of the super-kamiokande water cherenkov detector*, *Phys. Rev. D* **95** (2017) 012004.

[5] L. J. Hall, D. Pinner and J. T. Ruderman, *A natural susy higgs near 125 gev*, *Journal of High Energy Physics* **2012** (2012) 131.

[6] Planck Collaboration, *Planck 2018 results. VI. Cosmological parameters*, *Submitted to A&A* (2018) [1807.06209].

[7] N. Arkani-Hamed, A. Delgado and G. Giudice, *The well-tempered neutralino*, *Nuclear Physics B* **741** (2006) 108 .

[8] A. M. Baldini, Y. Bao, E. Baracchini, C. Bemporad, F. Berg, M. Biasotti et al., *Search for the lepton flavour violating decay $\mu^+ \to e^+\gamma$ with the full dataset of the meg experiment*, *The European Physical Journal C* **76** (2016) 434.

[9] L. Randall and R. Sundrum, *Out of this world supersymmetry breaking*, *Nuclear Physics B* **557** (1999) 79 .

[10] M. Ibe and T. T. Yanagida, *The lightest higgs boson mass in pure gravity mediation model*, *Physics Letters B* **709** (2012) 374 .

[11] M. Ibe, S. Matsumoto and T. T. Yanagida, *Pure gravity mediation with $m_{3/2} = 10 - -100$ TeV*, *Phys. Rev. D* **85** (2012) 095011.

[12] B. Bhattacherjee, B. Feldstein, M. Ibe, S. Matsumoto and T. T. Yanagida, *Pure gravity mediation of supersymmetry breaking at the large hadron collider*, *Phys. Rev. D* **87** (2013) 015028.

[13] T. Gherghetta, G. F. Giudice and J. D. Wells, *Phenomenological consequences of supersymmetry with anomaly induced masses*, *Nuclear Physics B* **559** (1999) 27 .

[14] S. Thomas and J. D. Wells, *Phenomenology of massive vectorlike doublet leptons*, *Phys. Rev. Lett.* **81** (1998) 34.

[15] M. Cirelli, N. Fornengo and A. Strumia, *Minimal dark matter*, *Nuclear Physics B* **753** (2006) 178 [0512090].

[16] M. Ibe, S. Matsumoto and R. Sato, *Mass splitting between charged and neutral winos at two-loop level*, *Physics Letters B* **721** (2013) 252 [1212.5989].

[17] J. McKay and P. Scott, *Two-loop mass splittings in electroweak multiplets: Winos and minimal dark matter*, *Phys. Rev. D* **97** (2018) 055049.

[18] N. Nagata and S. Shirai, *Higgsino dark matter in high-scale supersymmetry*, *Journal of High Energy Physics* **2015** (2015) 29.

[19] C.-H. Chen, M. Drees and J. F. Gunion, *Erratum: Nonstandard string-susy scenario and its phenomenological implications [phys. rev. d 55, 330 (1997)]*, *Phys. Rev. D* **60** (1999) 039901 [9902309].

[20] ATLAS Collaboration, *Search for charginos nearly mass degenerate with the lightest neutralino based on a disappearing-track signature in pp collisions at* $\sqrt{s} = 8$ *TeV with the ATLAS detector*, *Phys. Rev. D* **88** (2013) 112006 [1310.3675].

[21] CMS Collaboration, *Search for disappearing tracks as a signature of new long-lived particles in proton-proton collisions at* $\sqrt{s} = 13$ *TeV*, *Journal of High Energy Physics* **2018** (2018) 16.

[22] L. Evans and P. Bryant, *LHC machine*, *Journal of Instrumentation* **3** (2008) S08001.

[23] ATLAS Collaboration, *The ATLAS Experiment at the CERN Large Hadron Collider*, *JINST* **3** (2008) S08003.

[24] CMS Collaboration, *The CMS experiment at the CERN LHC*, *Journal of Instrumentation* **3** (2008) S08004.

[25] ALICE Collaboration, *The ALICE experiment at the CERN LHC*, *Journal of Instrumentation* **3** (2008) S08002.

[26] LHCb Collaboration, *The LHCb detector at the LHC*, *Journal of Instrumentation* **3** (2008) S08005.

[27] ATLAS Collaboration, *Study of the material of the ATLAS inner detector for Run 2 of the LHC*, *JINST* **12** (2017) P12009 [1707.02826].

[28] M. Capeans, G. Darbo, K. Einsweiller, M. Elsing, T. Flick, M. Garcia-Sciveres et al., *ATLAS Insertable B-Layer Technical Design Report*, Tech. Rep. CERN-LHCC-2010-013. ATLAS-TDR-19, Sep, 2010.

[29] G. Avoni, M. Bruschi, G. Cabras, D. Caforio, N. Dehghanian, A. Floderus et al., *The new LUCID-2 detector for luminosity measurement and monitoring in ATLAS*, *Journal of Instrumentation* **13** (2018) P07017.

[30] S. van der Meer, *Calibration of the effective beam height in the ISR*, Tech. Rep. CERN-ISR-PO-68-31. ISR-PO-68-31, CERN, Geneva, 1968.

[31] ATLAS Collaboration, *Luminosity determination in pp collisions at* $\sqrt{s} = 8$ *TeV using the ATLAS detector at the LHC*, *Eur. Phys. J. C* **76** (2016) 653 [1608.03953].

[32] ATLAS Collaboration, *Performance of the ATLAS trigger system in 2015*, *Eur. Phys. J. C* **77** (2017) 317 [1611.09661].

[33] S. Agostinelli, J. Allison, K. Amako, J. Apostolakis, H. Araujo, P. Arce et al., *Geant4 a simulation toolkit*, *Nuclear Instruments and Methods in Physics Research Section A: Accelerators, Spectrometers, Detectors and Associated Equipment* **506** (2003) 250 .

[34] J. Allison, K. Amako, J. Apostolakis, H. Araujo, P. A. Dubois, M. Asai et al., *Geant4 developments and applications*, *IEEE Transactions on Nuclear Science* **53** (2006) 270.

[35] J. Allison, K. Amako, J. Apostolakis, P. Arce, M. Asai, T. Aso et al., *Recent developments in geant4*, *Nuclear Instruments and Methods in Physics Research Section A: Accelerators, Spectrometers, Detectors and Associated Equipment* **835** (2016) 186 .

[36] T. Sjöstrand, S. Ask, J. R. Christiansen, R. Corke, N. Desai, P. Ilten et al., *An Introduction to PYTHIA 8.2*, *Comput. Phys. Commun.* **191** (2015) 159 [1410.3012].

[37] A. Ryd, D. Lange, N. Kuznetsova, S. Versille, M. Rotondo, D. P. Kirkby et al., *EvtGen: A Monte Carlo Generator for B-Physics*, .

[38] R. D. Ball, V. Bertone, S. Carrazza, C. S. Deans, L. D. Debbio, S. Forte et al., *Parton distributions with lhc data*, *Nuclear Physics B* **867** (2013) 244 .

[39] ATLAS Collaboration, "The Pythia 8 A3 tune description of ATLAS minimum bias and inelastic measurements incorporating the Donnachie–Landshoff diffractive model." ATL-PHYS-PUB-2016-017, 2016.

[40] F. E. Paige, S. D. Protopopescu, H. Baer and X. Tata, *ISAJET 7.69: A Monte Carlo event generator for pp,* $\bar{p}p$*, and* e^+e^- *reactions*, hep-ph/0312045.

[41] H. Fukuda, N. Nagata, H. Otono and S. Shirai, *Higgsino dark matter or not: Role of disappearing track searches at the lhc and future colliders*, *Physics Letters B* **781** (2018) 306 .

[42] J. Alwall, R. Frederix, S. Frixione, V. Hirschi, F. Maltoni, O. Mattelaer et al., *The automated computation of tree-level and next-to-leading order differential cross sections, and their matching to parton shower simulations*, *JHEP* **07** (2014) 079 [1405.0301].

[43] ATLAS Collaboration, "ATLAS Pythia 8 tunes to 7 TeV data." ATL-PHYS-PUB-2014-021, 2014.

[44] J. Debove, B. Fuks and M. Klasen, *Transverse-momentum resummation for gaugino-pair production at hadron colliders*, *Physics Letters B* **688** (2010) 208 .

[45] J. Debove, B. Fuks and M. Klasen, *Threshold resummation for gaugino pair production at hadron colliders*, *Nuclear Physics B* **842** (2011) 51 .

[46] J. Debove, B. Fuks and M. Klasen, *Joint resummation for gaugino pair production at hadron colliders*, *Nuclear Physics B* **849** (2011) 64 .

[47] B. Fuks, M. Klasen, D. R. Lamprea and M. Rothering, *Gaugino production in proton-proton collisions at a center-of-mass energy of 8 TeV*, *JHEP* **10** (2012) 081 [1207.2159].

[48] B. Fuks, M. Klasen, D. R. Lamprea and M. Rothering, *Precision predictions for electroweak superpartner production at hadron colliders with Resummino*, *Eur. Phys. J. C* **73** (2013) 2480 [1304.0790].

[49] C. Borschensky, M. Krämer, A. Kulesza, M. Mangano, S. Padhi, T. Plehn et al., *Squark and gluino production cross sections in pp collisions at $\sqrt{s}$ = 13, 14, 33 and 100tev*, *The European Physical Journal C* **74** (2014) 3174.

[50] T. Gleisberg, S. Hoeche, F. Krauss, M. Schonherr, S. Schumann, F. Siegert et al., *Event generation with SHERPA 1.1*, *JHEP* **02** (2009) 007 [0811.4622].

[51] The NNPDF collaboration, R. D. Ball, V. Bertone, S. Carrazza, C. S. Deans, L. Del Debbio et al., *Parton distributions for the lhc run ii*, *Journal of High Energy Physics* **2015** (2015) 40.

[52] Y. Li and F. Petriello, *Combining qcd and electroweak corrections to dilepton production in the framework of the fewz simulation code*, *Phys. Rev. D* **86** (2012) 094034.

[53] S. Frixione, G. Ridolfi and P. Nason, *A positive-weight next-to-leading-order monte carlo for heavy flavour hadroproduction*, *Journal of High Energy Physics* **2007** (2007) 126.

[54] S. Alioli, P. Nason, C. Oleari and E. Re, *NLO single-top production matched with shower in POWHEG: s- and t-channel contributions*, *JHEP* **09** (2009) 111 [0907.4076].

[55] R. Frederix, E. Re and P. Torrielli, *Single-top t-channel hadroproduction in the four-flavour scheme with powheg and amc@nlo*, *Journal of High Energy Physics* **2012** (2012) 130.

[56] E. Re, *Single-top wt-channel production matched with parton showers using the powheg method*, *The European Physical Journal C* **71** (2011) 1547.

[57] P. Artoisenet, R. Frederix, O. Mattelaer and R. Rietkerk, *Automatic spin-entangled decays of heavy resonances in monte carlo simulations*, *Journal of High Energy Physics* **2013** (2013) 15.

[58] M. Czakon and A. Mitov, *Top++: A program for the calculation of the top-pair cross-section at hadron colliders*, *Computer Physics Communications* **185** (2014) 2930 .

[59] N. Kidonakis, *Two-loop soft anomalous dimensions for single top quark associated production with a W- or H-*, *Phys. Rev.* **D82** (2010) 054018 [1005.4451].

[60] P. Kant, O. Kind, T. Kintscher, T. Lohse, T. Martini, S. Molbitz et al., *Hathor for single top-quark production: Updated predictions and uncertainty estimates for single top-quark production in hadronic collisions*, *Computer Physics Communications* **191** (2015) 74 .

[61] M. Aliev, H. Lacker, U. Langenfeld, S. Moch, P. Uwer and M. Wiedermann, *Hathor – hadronic top and heavy quarks cross section calculator*, *Computer Physics Communications* **182** (2011) 1034 .

[62] T. Cornelissen, M. Elsing, S. Fleischmann, W. Liebig, E. Moyse and A. Salzburger, *Concepts, Design and Implementation of the ATLAS New Tracking (NEWT)*, Tech. Rep. ATL-SOFT-PUB-2007-007. ATL-COM-SOFT-2007-002, CERN, Geneva, Mar, 2007.

[63] A. Rosenfeld and J. L. Pfaltz, *Sequential operations in digital picture processing*, *J. ACM* **13** (1966) 471.

[64] ATLAS Collaboration, *A neural network clustering algorithm for the ATLAS silicon pixel detector*, *JINST* **9** (2014) P09009 [1406.7690].

[65] ATLAS Collaboration, "Measurement of performance of the pixel neural network clustering algorithm of the ATLAS experiment at $\sqrt{s} = 13$ TeV." ATL-PHYS-PUB-2015-044, 2015.

[66] ATLAS Collaboration, "Robustness of the Artificial Neural Network Clustering Algorithm of the ATLAS experiment." ATL-PHYS-PUB-2015-052, 2015.

[67] ATLAS Collaboration, *Performance of the ATLAS track reconstruction algorithms in dense environments in LHC Run 2*, *Eur. Phys. J. C* **77** (2017) 673 [1704.07983].

[68] R. Fruhwirth, *Application of kalman filtering to track and vertex fitting*, *Nuclear Instruments and Methods in Physics Research Section A: Accelerators, Spectrometers, Detectors and Associated Equipment* **262** (1987) 444 .

[69] R. O. Duda and P. E. Hart, *Use of the hough transformation to detect lines and curves in pictures*, *Commun. ACM* **15** (1972) 11.

[70] ATLAS Collaboration, "Performance of primary vertex reconstruction in proton–proton collisions at $\sqrt{s} = 7$ TeV in the ATLAS experiment." ATLAS-CONF-2010-069, 2010.

[71] ATLAS Collaboration, "Performance of the ATLAS Inner Detector Track and Vertex Reconstruction in High Pile-Up LHC Environment." ATLAS-CONF-2012-042, 2012.

[72] ATLAS Collaboration, *Reconstruction of primary vertices at the ATLAS experiment in Run 1 proton–proton collisions at the LHC*, *Eur. Phys. J. C* **77** (2017) 332 [1611.10235].

[73] W. Waltenberger, R. Frühwirth and P. Vanlaer, *Adaptive vertex fitting*, *Journal of Physics G: Nuclear and Particle Physics* **34** (2007) N343.

[74] ATLAS Collaboration, *Topological cell clustering in the ATLAS calorimeters and its performance in LHC Run 1*, *Eur. Phys. J. C* **77** (2017) 490 [1603.02934].

[75] M. Cacciari, G. P. Salam and G. Soyez, *The anti-k_t jet clustering algorithm*, *Journal of High Energy Physics* **2008** (2008) 063.

[76] M. Cacciari, G. P. Salam and G. Soyez, *Fastjet user manual*, *The European Physical Journal C* **72** (2012) 1896.

[77] ATLAS Collaboration, *Jet energy scale measurements and their systematic uncertainties in proton–proton collisions at $\sqrt{s} = 13$ TeV with the ATLAS detector*, *Phys. Rev. D* **96** (2017) 072002 [1703.09665].

[78] ATLAS Collaboration, *Performance of pile-up mitigation techniques for jets in pp collisions at $\sqrt{s} = 8$ TeV using the ATLAS detector*, *Eur. Phys. J. C* **76** (2016) 581 [1510.03823].

[79] ATLAS Collaboration, "Electron efficiency measurements with the ATLAS detector using the 2012 LHC proton–proton collision data." ATLAS-CONF-2014-032, 2014.

[80] ATLAS Collaboration, "Improved electron reconstruction in ATLAS using the Gaussian Sum Filter-based model for bremsstrahlung." ATLAS-CONF-2012-047, 2012.

[81] ATLAS Collaboration, "Electron and photon reconstruction and performance in ATLAS using a dynamical, topological cell clustering-based approach." ATL-PHYS-PUB-2017-022, 2017.

[82] ATLAS Collaboration, *Measurement of the photon identification efficiencies with the ATLAS detector using LHC Run-1 data*, *Eur. Phys. J. C* **76** (2016) 666 [1606.01813].

[83] ATLAS Collaboration, *Measurement of the photon identification efficiencies with the ATLAS detector using LHC Run 2 data collected in 2015 and 2016*, *Submitted to: Eur. Phys. J.* (2018) [1810.05087].

[84] ATLAS Collaboration, *Electron and photon energy calibration with the ATLAS detector using 2015-2016 LHC proton-proton collision data*, *Submitted to: JINST* (2018) [1812.03848].

[85] ATLAS collaboration, M. Aaboud et al., *Electron reconstruction and identification in the ATLAS experiment using the 2015 and 2016 LHC proton-proton collision data at $\sqrt{s}$ = 13 TeV*, *Submitted to: Eur. Phys. J.* (2019) [1902.04655].

[86] ATLAS Collaboration, "Electron efficiency measurements with the ATLAS detector using the 2015 LHC proton–proton collision data." ATLAS-CONF-2016-024, 2016.

[87] ATLAS Collaboration, *Muon reconstruction performance of the ATLAS detector in proton–proton collision data at $\sqrt{s} = 13$ TeV*, *Eur. Phys. J. C* **76** (2016) 292 [1603.05598].

[88] ATLAS Collaboration, *Performance of missing transverse momentum reconstruction with the ATLAS detector using proton–proton collisions at $\sqrt{s} = 13$ TeV*, 1802.08168.

[89] ATLAS Collaboration, "$E_{\mathrm{T}}^{\mathrm{miss}}$ performance in the ATLAS detector using 2015–2016 LHC *pp* collisions." ATLAS-CONF-2018-023, 2018.

[90] ATLAS Collaboration, "Trigger Menu in 2017." ATL-DAQ-PUB-2018-002, 2018.

[91] ATLAS Collaboration, "Non-collision backgrounds as measured by the ATLAS detector during the 2010 proton–proton run." ATLAS-CONF-2011-137, 2011.

[92] ATLAS Collaboration, *Characterisation and mitigation of beam-induced backgrounds observed in the ATLAS detector during the 2011 proton–proton run*, *JINST* **8** (2013) P07004 [1303.0223].

[93] ATLAS Collaboration, "Selection of jets produced in 13 TeV proton–proton collisions with the ATLAS detector." ATLAS-CONF-2015-029, 2015.

[94] ATLAS Collaboration, "2015 start-up trigger menu and initial performance assessment of the ATLAS trigger using Run-2 data." ATL-DAQ-PUB-2016-001, 2016.

[95] ATLAS Collaboration, "Trigger Menu in 2016." ATL-DAQ-PUB-2017-001, 2017.

[96] A. L. Read, *Presentation of search results: The CL(s) technique*, *J. Phys. G* **28** (2002) 2693.

[97] G. Cowan, K. Cranmer, E. Gross and O. Vitells, *Asymptotic formulae for likelihood-based tests of new physics*, *Eur. Phys. J. C* **71** (2011) 1554 [1007.1727].

[98] A. Wald, *Tests of statistical hypotheses concerning several parameters when the number of observations is large*, *Transactions of the American Mathematical Society* **54** (1943) 426.

[99] L. Lönnblad and S. Prestel, *Matching tree-level matrix elements with interleaved showers*, *Journal of High Energy Physics* **2012** (2012) 19.

[100] ALEPH, DELPHI, L3, OPAL Collaboration, "Combined LEP Chargino Results, up to 208 GeV for low DM." LEPSUSYWG/02-04.1 , 2002.

[101] ATLAS Collaboration, *Search for squarks and gluinos in final states with jets and missing transverse momentum using* 36 fb^{-1} *of* $\sqrt{s} = 13$ *TeV pp collision data with the ATLAS detector*, *Phys. Rev. D* **97** (2018) 112001 [1712.02332].

[102] ATLAS Collaboration, *Technical Design Report for the ATLAS Inner Tracker Pixel Detector*, Tech. Rep. CERN-LHCC-2017-021. ATLAS-TDR-030, CERN, Geneva, Sep, 2017.

[103] ATLAS Collaboration, "ATLAS sensitivity to winos and higgsinos with a highly compressed mass spectrum at the HL-LHC." ATL-PHYS-PUB-2018-031, Geneva, Nov, 2018.

[104] ATLAS collaboration, ATLAS Collaboration, "Expected performance of the ATLAS detector at the High-Luminosity LHC." ATL-PHYS-PUB-2019-005, Geneva, Jan, 2019.

[105] ATLAS Collaboration, *Search for long-lived charginos based on a disappearing-track signature in pp collisions at* $\sqrt{s} = 13$ *TeV with the ATLAS detector*, *JHEP* **06** (2018) 022 [1712.02118].

[106] M. Mangano, P. Azzi, M. Benedikt, A. Blondel, D. A. Britzger, A. Dainese et al., *Future Circular Collider*, Tech. Rep. CERN-ACC-2018-0056, CERN, Geneva, Dec, 2018.

[107] M. Saito, R. Sawada, K. Terashi and S. Asai, *Discovery reach for wino and higgsino dark matter with a disappearing track signature at a 100 TeV pp collider*, 1901.02987.

[108] S. Asai, S. Chigusa, T. Kaji, T. Moroi, M. Saito, R. Sawada et al., *Studying gaugino masses in supersymmetric model at future 100 TeV pp collider*, 1901.10389.